UNIVERSIDADE DO VALE DO RIO DOS SINOS
UNIDADE ACADÊMICA DE PESQUISA E PÓS-GRADUAÇÃO
PROGRAMA DE PÓS-GRADUAÇÃO EM ENGENHARIA ELÉTRICA
NÍVEL MESTRADO PROFISSIONAL

SUNKYUNKWAN UNIVERSITY
COLLEGE OF ENGINEERING
ADVANCED MATERIALS SCIENCE AND ENGINEERING DEPARTMENT

Bernardo Bortolotto Ilha

Influence of minor Zn addition on the microstructural stability of Sn-0.7 wt% Cu solder after aging and electromigration

São Leopoldo
2018

Bernardo Bortolotto Ilha

Influence of minor Zn addition on the microstructural stability of Sn-0.7 wt% Cu solder after aging and electromigration

Thesis presented as partial requirement for obtaining the title of Master, by the Program of Graduation in Electrical Engineering of Universidade do Vale do Rio dos Sinos – UNISINOS, and by the College of Engineering on the academic program of Advanced Materials Science and Engineering.

Advisor (Unisinos): Prof. Dr. Eduardo Luis Rhod

Advisor (Sungkyunkwan Univ.): Seung-Boo Jung

Advisor (Sungkyunkwan Univ.): Yongil Kim

São Leopoldo

2018

I27i Ilha, Bernardo Bortolotto.

Influence of minor Zn addition on the microstructural stability of Sn-0.7 wt% Cu solder after aging and electromigration / Bernardo Bortolotto Ilha. – 2018.

98 f. : il. color. ; 30 cm.

Dissertação (mestrado) – Universidade do Vale do Rio dos Sinos, Programa de Pós-Graduação em Engenharia Elétrica, São Leopoldo, 2018.

"Advisor: Prof. Dr. Eduardo Luis Rhod ; Advisor (Sungkyunkwan Univ.): Seung-Boo Jung ; Advisor (Sungkyunkwan Univ.): Yongil Kim."

1. Sn solder. 2. Zn alloying. 3. Isothermal aging. 4. Electromigration. I. Título.

CDU 621.3

Dados Internacionais de Catalogação na Publicação (CIP)
(Bibliotecária: Bruna Sant'Anna – CRB 10/2360)

SUMMARY

LIST OF FIGURES **7**

LIST OF TABLES **13**

ABSTRACT **15**

CHAPTER 1. INTRODUCTION **17**
1.1. Overview **17**
1.2. Objectives **17**

CHAPTER 2. LITERATURE REVIEW **18**
2.1. Electronic Packaging **18**
2.2. Soldering **20**
2.2.1. Pb-free solders 20
2.2.2. Recent issues with Pb-free solders 23
2.3. Pb-free solder alloys **23**
2.3.1. Reactive Wetting 23
2.3.2. Interfacial Intermetallic Compound (IMC) Formation 26
2.3.3. Bulk Microstructure 34
2.3.3.1. Sn-Cu Alloy and Zn addition 34
2.3.3.2. Effect of Zn on the Undercooling 38
2.3.4. Solder strength 42
2.3.5. Electromigration 43
2.3.5.1. Electromigration Kinetics 43
2.3.5.2. Polarity and Reverse Polarity Effects 44
2.3.5.3. Current Crowding 47
2.3.5.4. Anisotropy diffusivity in β-Sn 48
2.3.5.5. Reliability depending on surface finish and Zn content 50

CHAPTER 3. EXPERIMENTAL PROCEDURES **52**
3.1. Solder alloy and test samples **52**
3.2. Aging Experiments **54**
3.3. Electromigration Experiments **55**

CHAPTER 4. EXPERIMENTAL RESULTS AND DISCUSSION **60**
4.1. Microstructure as reflowed **60**
4.1.1. Interfacial IMC 60
4.1.2. Bulk IMC and grain size distribution 65
4.2. Microstructure evolution upon aging **70**
4.2.1. Interfacial IMC 70
4.2.2. Bulk IMC and grain size distribution 74
4.2.3. Shear tests 78
4.3. Electromigration **81**
4.3.1. Resistance change during the tests 81
4.3.2. Characterization of compounds formed after electromigration tests 83
4.3.3. Grain orientation analysis 87

CHAPTER 5. SUMMARY AND CONCLUSIONS **92**
5.1. As reflowed condition **92**
5.2. Aging experiments **92**
5.3. Electromigration experiments **93**

REFERENCES **94**

LIST OF FIGURES

Figure 1: (a) Moore's law for systems' integration; (b) Package evolution trend. [3] 18

Figure 2: SOP concept of system integration of components. [4] 19

Figure 3: Diagram of wetting angle. [6] 24

Figure 4: Axis x is the mass percent content of Zn into Sn-0.7 wt.%Cu solder vs.: (a) Wetting angle & Surface tension; and (b) Cosine of wetting angle & Driving force of first formed IMC. [25] 25

Figure 5: Wetting balance tests of Sn-0.7 wt.%Cu-X wt.%Zn, where X = 0, 0.2, 0.5, 1.0. Atmosphere: (a) in air; (b) in N_2. [25] 25

Figure 6: Wetting angle measurements (a) for various solders without flux in vacuum and (b) for Sn-0.7 wt.%Cu solder using three different commercial fluxes. [17] 26

Figure 7: Micrographs of (a) Eutectic Sn-37 wt.%Pb, (b) Eutectic Sn-3.5 wt.%Ag, (c) Sn-3.8 wt.%Ag-0.7 wt.%Cu, and (d) Sn-0.7 wt.%Cu. [19] 27

Figure 8: (a) Sn-rich corner of Sn-Cu-Zn system (YANG; KAO; 2006) and (b) calculated driving forces for various IMC formation. [24, 25] 28

Figure 9: Formation of interfacial IMC between Cu and: (a) Sn-0.5 wt.%Zn; (b) Sn-0.7 wt.%Zn; and (c) Sn-2.0 wt.%Zn. [26] 28

Figure 10: Formation of interfacial IMC between Ni-P and Sn-3.5 wt.%Ag-0.7 wt.%Cu reflowed at 250 °C for two reaction times: (a) 1s; (b) 1 minute. [50] 28

Figure 11: Intermetallic morphology development of an air cooled sample during aging at 175°C (a) 0 h; (b) 170 h; (c) 500 h; and (d) 1000 h. [28] 30

Figure 12: Total intermetallic thickness as a function of aging time for different aging temperatures: (a) 100°C, (b) 140°C, and (c) 175°C. [28] 30

Figure 13: Schematic diagram of the growth of Cu_3Sn on polycrystalline Cu after (a) reflow and (b) solid state aging. (c) Ratio of Cu_3Sn to total IMC thickness of Sn-0.7 wt.%Cu under aging treatment at 120, 150 and 170 °C. [21, 30] 31

Figure 14: A schematic model of the possible fluxes due to interdiffusion in a Cu/Sn/Cu sample (not to scale). [32] 32

Figure 15: (a) Thickness of each IMC layer as a function of Zn composition in SAC after aging for 1000 h at 150°C on electroplated Cu; and compositional profiles of Sn, Cu and Zn plotted along the distance perpendicular to the IMC interface of (b) Sn-0.7 wt.%Cu-0.4 wt.%Zn and (c) Sn-3.8 wt.%Ag-0.7 wt.%Cu-0.4 wt.%Zn. (d) Thickness of each IMC layer as a function of Zn composition in Sn-0.7 wt.% Cu after aging for 1000 h at 150°C on ENIG UBM. [27, 34] 33

Figure 16: Back-scatted electron images of the interface on Cu that was etched by the solution of NH4OH and H2O2 (3%) in DI water; (a) Sn-3.8Ag-0.7Cu-0.4Zn as-reflowed, (b) Sn-3.8Ag-0.7Cu-0.4Zn aged for 1000 h and (c) Sn-3.8Ag-0.7Cu aged for 1000 h. [27] 34

Figure 17: Cu-Sn binary phase diagram. [54] 35

Figure 18: Longitudinal (top) and transverse (bottom) cross-sections of Bridgman's method samples solidified at 10 μm^{-1}. (a) Primary dendrites followed by a eutectic interface (Sn–0.5 Cu), (b) primary cells followed by a eutectic interface (Sn–0.7 Cu) and (c) random distribution of Cu_6Sn_5 fibres (Sn–0.9 Cu). [55] 35

Figure 19: (a) Projection view of Sn lattice onto the (0 1 0) plane, showing a basic {1 0 1} twin segment and a {1 0 1} cyclic twin nucleus. (b) Perspective view of {1 0 1} cyclic twin nucleus faceted on {1 1 0} planes and rendered as planes. [56] 36

Figure 20: (a) Projection view of Sn lattice onto the (0 1 0) plane, showing a basic {3 0 1} twin segment and a {3 0 1} cyclic twin nucleus. (b) Perspective view of the {3 0 1} cyclic twin nucleus faceted on {1 1 0} and {0 0 1} planes and rendered as planes. [56] 36

Figure 21: Cross polarized image of cross sectioned Sn based solders: in at.% (a) Sn-0.16 Co; (b) 3.0 Ag-0.5 Cu; (c) Sn-0.44 Ag; and (d) inverse pole figure map of sample (c). [60] 37

Figure 22: Vertical section of the Sn-Cu-Zn ternary phase diagram calculated along a constant ratio of 99.3Sn:0.7Cu (in wt.%). [35] 38

Figure 23: Cross-section SEM micrographs after etching of (a) eutectic SnPb, (b) Sn–3.8 wt.%Ag–0.7 wt.%Cu, and (c) Sn–0.7 wt.%Cu. [21] 38

Figure 24: Cross-polarized images of Sn-1.0Ag-Zn solder balls as a function of cooling rate and Zn composition (0 wt.%, 0.2 wt.%, 0.4 wt.%, and 0.6 wt.%). [54] 39

Figure 25: EBSD results of Sn-Ag-Zn/Cu UBM joints; (a) and (b), inverse pole figure maps; (c) and (d), image quality maps; and (e) and (f); inverse pole figures. [54] 40

Figure 26: OM images of the four different solders taken far from the interface: as-reflowed (top row) and aged at 150 °C for 500 h (bottom row). [35] 40

Figure 27: Optical micrographs of Sn1.0Ag0.6Zn solder ball after thermal aging at 200 °C for 8 hrs: (a) cross-polarized micrograph; (b) bright field micrograph. [34] 41

Figure 28: Respectively, EBSD image quality and inverse pole figure map for Sn-0.5 wt.% Cu onto: (a) and (b) electroless Cu UBM, and (c) and (d) ENIG UBM. [63] 42

Figure 29: Isothermal EM stressing of Sn-3.8 wt.%Ag-0.7 wt.%Cu solder at 180 °C. (a) to (h): SEM images of microstructure evolution due to 3.2e+04 A/cm² current density EM stressing. (i): Total thickness [$(\Delta x)^2$] change of IMCs with time at various current densities. [39] 45

Figure 30: Isothermal EM stressing of Sn-9.0 wt.%Zn solder at 150 ±5 °C at current density of 3.87e+04 A/cm². (a) to (d) SEM images of IMCs at the anode (left column) and the cathode (right column) (e) Total thickness [$(\Delta x)^2$] change of IMCs with time. [44] 46

Figure 31: Interface morphology of Sn–1.0 wt.%Ag–0.5 wt.%Cu (a) and (b), and Sn–1.0 wt.%Ag–0.5 wt.%Cu-1.0 wt.%Zn (c) and (d) solder joints both after electromigration for 100 h under current density of 2e+04 A/cm². The anodes are to the left and cathodes to the right. [45] 47

Figure 32: Cross-sectional view showing the current-crowding effect in solder bumps during current stressing. Peak current density occurs at the current entrances of the Al trace into the solder bump. [41] 48

Figure 33: Void propagation in a solder joint assisted by current crowding effect. [46] 48

Figure 34: Panel (a) displays the diffusion pathway (the red balls) for interstitial atom jumping along the c-axis and a-axis. The cyan and green balls represent the two different layers of β–Sn. Panels (b) and (c) shows the diffusion energy curves of Cu and Ag along the c-axis and a-axis, respectively. [47] 49

Figure 35: SEM image of a bi-crystal Sn-Cu solder bump. [36] 50

Figure 36: Plot of resistance change versus EM stress time under 5.2e+03 A/cm² current density for (a) Sn-1.0 wt.%Ag and (b) to (d) Sn-1.0 wt.%Ag-0.6 wt.%Zn. Solder using for anode and cathode, respectively in each case: (a) and (b) bare Cu and Ni UBM; (c) Ni UBM and bare Cu; and (d) Ni UBM at both sides. [36] 51

Figure 37: Effects of the surface finish on the EM reliability at 130 °C and 5.0e+04 A/cm², for the Sn-1.2 wt.%Ag-0.7 wt.%Cu-0.4 wt.%In solder. [48] 51

Figure 38: SEM image and EDS point elemental analysis for solders B (a, d), C (b, e) and D (c, f) reflowed on ENIG substrate. 53

Figure 39: EPMA on flux residue left around solder joint showing backscattered electron image – BEI (a), elemental scan for Zn (b), Cu (c) and Sn (d). Acceleration voltage 15 kV, Beam Size 1 µm, Step 1 x 1 µm. The scale bar on the side of each image represents the element count color label. 53

Figure 40: Process of producing samples for this research (a); example of as printed solder paste on a substrate (b); illustration of ENIG and OSP surface finishes (c). 54

Figure 41: Reflow profile measured by thermocouple sensor. The oven's 4 zones are illustrated superimposed to the curve. Peak temperature was 260 °C, time above melting temperature was around 1 minute. After reflow, samples underwent air-cooling of 1.83 °C/s on average. 54

Figure 42: Illustration of shear test scheme and parameters. Shear speed was 600 µm/s and tool standoff was 10 µm. 55

Figure 43: Illustration of method for measuring the joints' temperature while currents ranging from 100 mA to 3.3 A were applied 56

Figure 44: Results from Joule Heating effect experiments. Currents applied ranging from 100 mA to 3,25 A in ambient temperatures of 25 °C and 125 °C. The sensitivity was calculated as 7.7 °C/A. 56

Figure 45: Results from TCR measurement experiments. Ambient temperature had values ranging from 25 °C to 150 °C and currents applied were 100 mA and 3,25 A. The TCR was calculated as 0.001 $°C^{-1}$. 57

Figure 46: (a) Illustration of experiments set up; (b) example of sample used in the experiments; and (c) illustration of solder joints couple. 58

Figure 47: (a) X-ray image of sample with macrovoid with area of 20.7% of the total joint image area; (b) cross section of solder with macrovoid; and (c) X-ray image of sample with void with area of 7.6% of the total joint image area. 58

Figure 48: Example of sample prepared for EBSD analysis, where a conductive paste was applied on the surroundings of the joints in order to eliminate charge accumulation on the surface of the non-conductive materials (FR-4 substrate and epoxy mount). 59

Figure 49: SEM images and EDS elemental analysis results in spectrum of counts vs. diffraction energy and summary table of elements, respectively, for the solder A (a) and (c), B (b) and (d), C (e) and (f) and D (g) and (h). 61

Figure 50: SEM images for solders A (a) and (b), B (e), D (f) and C (g) and EDS elemental analysis results in spectrum of counts vs. diffraction energy and summary table of elements, for solder A (c) and (d), and C (h). .. 62

Figure 51: Total IMC thickness measurement for solders A, B, C and D with OSP and ENIG surface finishes after reflow of 1 minute above melting temperature. 63

Figure 52: EPMA line scan in the region between the solder bulk and substrate using ENIG surface finish for solders B (a), D (b) and C (c). 64

Figure 53: EPMA line scan in the region between the solder bulk and substrate using OSP surface finish for solders B (a), D (b) and C (c). 65

Figure 54: SEM image of etched cross section of solder D (a) and EDS elemental analysis' spectrum and summary table made on a bulk IMC near the interface. 65

Figure 55: Cross section image obtained by optical microscope with bright field light showing the distribution of the IMCs in solders A (a), B (b), C (c) and D (d), in an as reflowed condition using OSP surface finish. 66

Figure 56: Cross section image obtained by optical microscope with bright field light showing the distribution of the IMCs in solders A (a), B (b), C (c) and D (d), in an as reflowed condition using ENIG surface finish. 67

Figure 57: Cross section image obtained by optical microscope with cross polarized light showing the grain morphology in solders A (a), B (b), C (c) and D (d), in an as reflowed condition using OSP surface finish. 68

Figure 58: Cross section image obtained by optical microscope with cross polarized light showing the grain morphology in solders A (a), B (b), C (c) and D (d), in an as-reflowed condition using ENIG surface finish. 69

Figure 59: Boxplot chart of grains sizes for solders A, B, C and D and OSP and ENIG surface finishes using a logarithmic scale. 69

Figure 60: Bright field image of the interfacial IMCs of samples aged isothermally at 175 °C for 500 h, for solders A (a), B (b), C (c) and D (d) using OSP surface finish. The Cu_6Sn_5 IMC appear as a brighter phase on top of a darker Cu_3Sn IMC. 70

Figure 61: Total IMC thickness versus the square root of the aging time, at 125, 150 and 175 °C, for solders A (a), B (b), C (c) and D (d) using OSP surface finish. 71

Figure 62: Cu3Sn IMC thickness versus the square root of the aging time, at 125, 150 and 175 °C, for solders A (a), B (b), C (c) and D (d) using OSP surface finish. 72

Figure 63: Comparison between each solder's total IMC and Cu3Sn IMC thickness after 500 h of isothermal aging at 125 °C (a), 150 °C (b) and 175 °C (c). 72

Figure 64: Bright field image of the interfacial IMCs of samples aged isothermally at 175 °C for 500 h, for solders A (a), B (b), C (c) and D (d) using ENIG surface finish. The Ni_3Sn_4 and AuSn4 IMCs appear as a brighter phase on top of a darker Cu_3Sn IMC. 72

Figure 65: Total IMC thickness versus the square root of the aging time, at 125, 150 and 175 °C, for solders A (a), B (b), C (c) and D (d) using ENIG surface finish. 73

Figure 66: Comparison between each solder's total IMC thickness after 500 h of isothermal aging at 125, 150 and 175 °C.. 73

Figure 67: Characteristic IMC morphology obtained by optical microscope using bright field light after 200 hours of aging at 3 different temperatures, 125, 150 and 175 °C, for solders A, B, C and D using OSP surface finish. 75

Figure 68: Characteristic IMC morphology obtained by optical microscope using cross polarized light after 200 hours of aging at 3 different temperatures, 125, 150 and 175 °C, for solders A, B, C and D using ENIG surface finish. 75

Figure 69: Boxplot charts of grains sizes for aged solders A, B, C and D and OSP surface finishes for various aging times ranging from 50 to 500 h and test temperatures of 150 °C (a), 125 °C (b) and 175 °C (c)......................... 76

Figure 70: Characteristic IMC morphology obtained by optical microscope using bright field light after 200 hours of aging at 3 different temperatures, 125, 150 and 175 °C, for solders A, B, C and D using ENIG surface finish. 77

Figure 71: Characteristic IMC morphology obtained by optical microscope using cross polarized light after 200 hours of aging at 3 different temperatures, 125, 150 and 175 °C, for solders A, B, C and D using ENIG surface finish. 77

Figure 72: Boxplot charts of grains sizes for aged solders A, B, C and D and ENIG surface finishes for various aging times ranging from 50 to 500 h and test temperatures of 150 °C (a), 125 °C (b) and 175 °C (c)............... 78

Figure 73: Shear force (g) vs aging time (h) for solders A, B, C and D using OSP surface finish and test temperatures of 150 °C (a), 125 °C (b) and 175 °C (c). 79

Figure 74: Shear force (g) vs aging time (h) for solders A, B, C and D using ENIG surface finish and test temperatures of 150 °C (a), 125 °C (b) and 175 °C (c). 80

Figure 75: Shear pattern of solders A and B (Sn-0.7 wt.%Cu and Sn-0.9 wt.%Cu-0.19 wt.%Zn) aged for 500 h for the following test temperature and surface finish for A and B, respectively: 125 °C and ENIG (a) and (b); 175 °C and ENIG (c) and (d); 175 °C and OSP (e) and (f). EDS mapping for solders A and B for the following elements, respectively: Sn (g) and (h); and Cu (i) and (j).. 81

Figure 76: Resistance change (*R/R0*) versus time during electromigration tests for three different samples using solder A and OSP surface finish.. 82

Figure 77: Solder joint exhibiting a propagate pancake-type void after current stress during an electromigration test. The sample used solder A and OSP surface finished... 82

Figure 78: SEM image of solder joint couples stressed for 200 h in the electromigration tests. Both couples used OSP surface finish. It was used solder B for fabrication of the couple on the images (a) and (b), and the solder alloy C for the couple on the images (c) and (d). 83

Figure 79: SEM image of solder joints stressed for 200 h in the electromigration tests. Both joints used ENIG surface finish. It was used solder A for fabrication of the joint on the image (a), and solder C for the joint on the images (b). The white dashed line indicates the location where EPMA line scan took place. 84

Figure 80: EDS analysis of different IMC compounds formed during 200 h of electromigration tests. Both joints used OSP surface finish. The joint (a) was fabricated with solder B and the spectrum of each point analyzed is shown on Figures (c) and (e). The joint (b) was fabricated with solder C and the spectrum of each point analyzed is shown on Figures (d) and (f)... 85

Figure 81: EDS analysis of different IMC compounds formed during 200 h of electromigration tests. Both joints used ENIG surface finish. The joint (a) was fabricated with solder A and the spectrum of each point analyzed is shown on Figures (c) and (e). The joint (b) was fabricated with solder C and the spectrum of each point analyzed is shown on Figures (d) and (f)... 86

Figure 82: Line EPMA scan over an IMC formed at the cathode of a test sample that underwent 200 h of current stress. The joint was fabricated with solder C and ENIG surface finish. 87

Figure 83: Illustration of a sample with a single grain with its orthogonal c-axis oriented parallel to TD and the result in terms of the inverse pole figure map. 88

Figure 84: Bright field image (a), cross polarized light image (b) and inverse pole figure map (c) of cross section of joint fabricated using solder A and OSP surface finish that underwent 50 h of electromigration stress........... 88

Figure 85: SEM image (a), cross polarized light image (b) and inverse pole figure map (c) of cross section of joint fabricated using solder A and OSP surface finish that underwent 200 h of electromigration stress. 89

Figure 86: Bright field images (a) and (b), cross polarized light images (c) and (d), inverse pole figure maps (e) and (f) and zoomed in bright field image (g) and (h) of cross sections of joints fabricated using, respectively, solder A and solder C, and OSP surface finish that underwent, respectively, 50 and 100 h of electromigration stress... 90

Figure 87: Cross section of samples that underwent 50 h of electromigration stress and were fabricated using ENIG surface finish. The solder alloys used were A, B, C and D, and bright field OM images are, respectively, (a), (b), (g) and (h); cross polarized OM images are, respectively, (c), (d), (i) and (j), and the inverse pole figure maps are, respectively, (e), (f), (k) and (l). 91

LIST OF TABLES

Table 1: Pb-free solder criteria and desired attributes. [8] 21

Table 2: Major solder alloys melting temperature and relative price compared to SnPb solder. [9] 22

Table 3: Major solder alloy systems remarks regarding replecement of SnPb solder. [8] 22

Table 4: Pb-free solders required mechanical properties. [8] 23

Table 5: ICP-OES analyses of solders A (Sn-Cu), and B, C and D (Sn-Cu-Zn). 52

ABSTRACT

Influence of minor Zn addition on the microstructural stability of Sn-0.7 wt.% Cu solder after aging and electromigration

The aging and electromigration (EM) effects were evaluated when up to 0.19 wt.% Zn was added to Sn-0.7 wt.% Cu solder. Currently, the Sn-0.7 wt.% Cu solder is being widely used in the electronic industries due to its advantages of low cost and high temperature applications. However, its usage is also limited by detrimental properties – for instance, when compared to SAC305, Sn-0.7 wt.% Cu solder has lower electromigration life time, shear strength and drop reliability. Minor Zn alloying to Pb-free solders reportedly enhances some of their properties, e.g.: stabilization of bulk microstructures by decreasing undercooling; formation of a thin interfacial diffusion barrier and, thereby, suppressing Cu_3Sn and Cu_6Sn_5 interfacial IMC growth rate and retarding under bump metallurgy (UBM) diffusion through the solder; and also, compensation for Sn self-diffusion due to reverse polarity effect.

In this research, the aging and EM effects are assessed when 0.09, 0.16 and 0.19 wt.% Zn were added to Sn-0.7 wt.% Cu solder. The samples underwent up to 500 h of isothermal aging at temperatures of 125, 150 and 175 °C, and EM samples underwent up to 200 h of stressing at a constant temperature of 150 °C and current of 3.25 A. Solder balls were fabricated on a BGA structure for the aging tests, and for the EM tests, a pair of solders was assembled in a daisy-chain structure with organic solderability preservative (OSP) and electroless nickel immersion gold (ENIG) surface finishes. The microstructural evolution and compositional distribution analyses were carried out using optical microscope with brightfield and cross polarized light, scanning electron microscope (SEM), energy dispersive spectrometer (EDS), electron probe micro analyzer (EPMA), and electron backscattered diffraction (EBSD).

The addition of Zn suppresses the formation of Cu_3Sn IMC and the total interfacial IMC thickness upon aging, and the samples with ENIG had smaller IMC thickness than OSP surface finish. In addition, the grains' microstructure becomes less interlaced and more stable, indicating lower undercooling. The electromigration effects on the microstructure is mainly governed by the relative orientation between the c-axis of Sn grains and the direction of current flow. When parallel, allows cathode UBM and alloying elements diffusion through the solder and formation of IMC, and, when transverse, inhibits this diffusion leading to failure by void formation at the anode UBM/solder interface due to depletion of the UBM and slow Sn self-diffusion.

Key words: Sn solder, Zn alloying, isothermal aging, electromigration.

CHAPTER 1. INTRODUCTION

1.1. Overview

Semiconductor devices are essential in modern lives. According to the World Semiconductor Trade Statistics WSTS [1], the total market value of integrated circuit, sensors and optoelectronics devices reached 339 billion dollars in 2016. It Is expected to have a growth of 11% in 2017, reaching 337.8 billion dollars in 2017, and grow to 387.2 by 2019. New usage or perspectives for devices such as mobile cellphones, PC, automobile, Internet of Things, medical devices, and, also, competitiveness arisen from tight market, increasing raw materials and subcontract price, new applications, create the need for innovation and science development in terms of either cheaper, more adequate or reliable materials and processes.

Since international efforts to ban high containing Pb solders took place with Waste Electrical and Electronic Equipment (WEEE) and Restriction of Certain Hazardous Substance (RoHS) directives, much research has been developed to understand the mechanisms of formation and failure of Pb-free solders and improve its mechanical and electrical properties, as well as reduce cost. Among the Pb-free solder options studied and available today in the market are Sn-Ag-Cu (SAC), Sn-Cu, Sn-Bi and Sn-Zn solder systems, and additional alloying elements are also studied.

Sn-Ag-Cu (SAC) solders are regarded as the most promising solder and holds the biggest market share between all Pb-free solders, however it has a high cost. Sn-Cu solders were at almost half the price of a SAC solder by 2007 [9] and its reliability is adequate for certain applications that do not demand high mechanical strength, creep resistance or stability during high current application. Many researchers have studied ways to increase Sn-Cu solder overall reliability through micro alloying. One of the most promising elements for micro alloying the Sn-Cu solder is Zn, which is claimed to stabilize bulk microstructures by decreasing β-Sn undercooling [13, 54], forming of a thin interfacial diffusion barrier and thereby, suppressing interfacial IMC growth rate and retarding under bump metallurgy (UBM) Cu diffusion through the solder upon aging [27] and current application [34], and also, compensating for Sn self-diffusion due to reverse polarity effect [39, 44]. Additionally, to the characteristics of alloying, the solder joint's reliability is highly affected by the Sn grain orientation, the surface finish used and also joint geometry [40, 44, 47].

As a common trend in electronics, the components get smaller and smaller over the years, in order to improve speed, decrease size of devices and reduce energy consumption. The solder joints may reach today a size as little as 1 µm. However, the joints become a source of concern regarding its mechanical reliability, due to a smaller cross section area, thus smaller shear strength and toughness, and also stability under high electrical current density, since the current density is inversely proportional to the cross-sectional area of the solders.

1.2. Objectives

- General: Evaluate the thermal aging and electromigration effects on the Sn-Y wt.% Cu, where Y = 0.5 and 0.7, and minor Zn additions of 0.09, 0.16 and 0.19 wt.%.
- Specific:

  a. Evaluate the thermal aging influence on microstructure and mechanical strength;

  b. Assess the electromigration effects associated with Zn;

  c. Observe the influence of two different surface finishes: OSP and ENIG.

CHAPTER 2. LITERATURE REVIEW

2.1. Electronic Packaging

The electronic packaging is a technology indispensable for the use of modern electronic devices, as it provides four essential functions:

- Interconnection for electrical signals between components;
- Distribution of electrical energy that powers the devices;
- Protection of circuits against mechanical shock and environment hazards, such as moisture, dust particles, electro-static discharge (ESD), etc.;
- Dissipation of heat generated by the circuit.

Packages are usually classified into 4 levels of interconnections, which are cited next followed by an example: zero level – transistor integration circuitry inside a silicon chip; 1st level – printed circuit board (PCB) substrate mounted and molded integrated circuit (IC) chip; 2nd level – PCB assembled passive and active components, such as onto a memory card; and 3rd level – motherboard assembly [2].

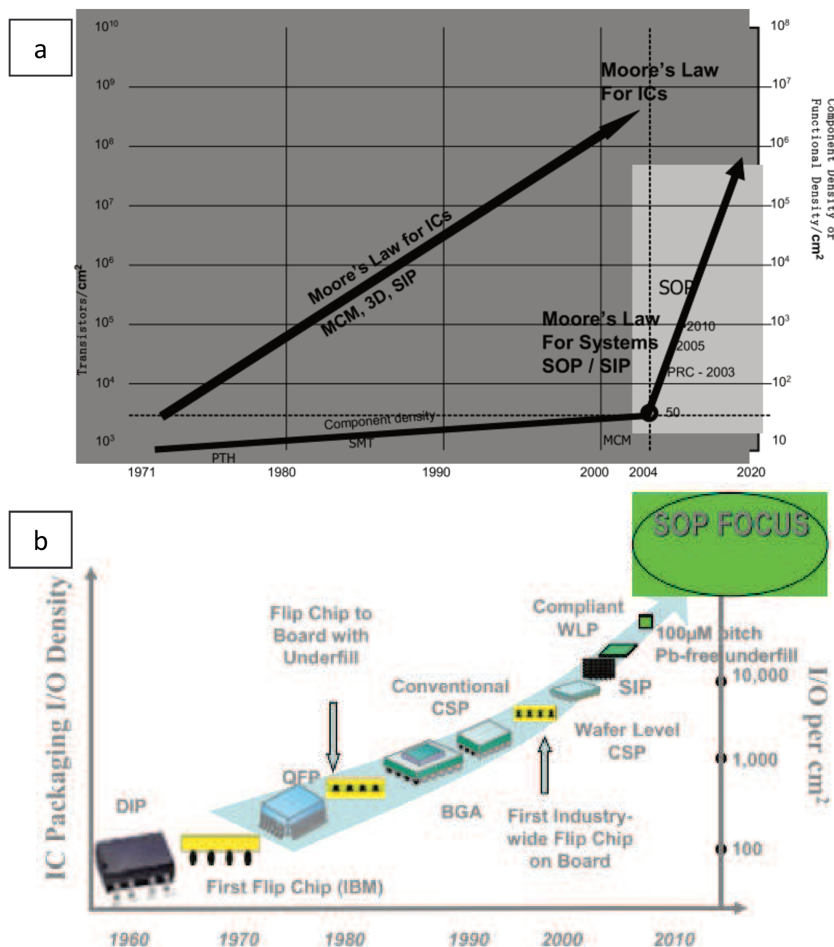

Figure 1: (a) Moore's law for systems' integration; (b) Package evolution trend. [3]

Moore’s law, around the 1970’s, predicted basically that the number of transistors in a dense IC would double approximately every two years and is still followed by the industry. It has being achieved by scaling down the minimum dimension of a transistor, reaching 14 nm technology node on 2014 using finFET technology. Scaling down transistors means that packages should adapt, also scaling down and increasing the number of I/O - note in Figure 1 (a) that Moore’s law for IC and systems’ integration are proportional; also, components count per cm² reaches 10^3 in 2010 and is expected to reach 1 million components/cm² by 2020. The drive of IC I/O increase and down scaling resulted in the development of packaging technologies such as DIP – dual in-line package, QFP – quad flat package, BGA – ball grid array, SOP – system on package, as seen in Figure 1 (b) [3]. Other factors such as the device size reduction, reduction of resistance-capacitance (RC) effect on the circuitry, special applications, etc., had also contributed to development of new technologies and package performance.

In Figure 2, we can see that the reality of packaging is chaging towards close integration of systems, where on the same packages, many relatively small devices are assembled, passives are eliminated and are embbeded into SIP – system in packages, together with different functional devices. Micro-electromechanical systems (MEMS) sensors can be placed beside wire bonded or flip chip devices, using solders that can reach 1 µm size. The use of wire bonding will still be seen, due to its lower cost, however vias and flip chip and through via technologies are likely to take over the market since they offer shorter circuitry and demand smaller area [4].

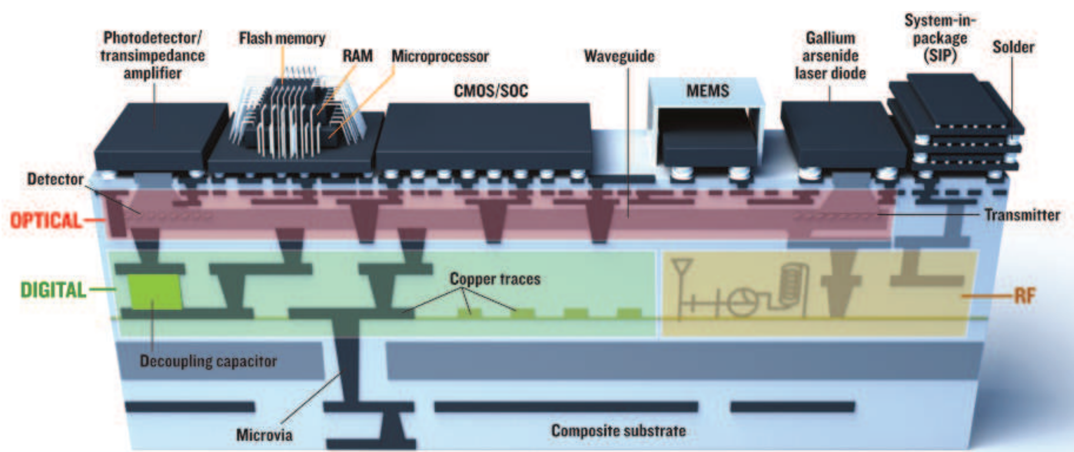

Figure 2: SOP concept of system integration of components. [4]

According to a reading of iNEMI Technology Roadmap of 2015 the next challenges for packaging technology development include the topics mentioned below [5].

- MEMS standardization of reliability test methods and standards for critical applications such as implantable medical devices;
- Reliability simulations of material characterization, interfacial delamination and chip-package interaction, process modeling, moisture modeling and solder joint reliability modeling;
- New capability to close the gap between chip and substrate interconnect density;
- 3D package stacking development with emphasis on assembly, testing, cooling and reliability;

- Low-temperature assembly of soldering and strategic opportunities for room temperature processing;
- Low-cost, high-density, high-performance PCB substrate technology of rigid & flex;
- Next generation of solder materials to replace the high-cost and high-temperature silver containing alloys and also non-silver bearing alloys for medical applications;
- New interconnect technologies deploying nanomaterials to support decreased pitch and increased interconnect frequencies;
- High-end processors require more I/O data than electronics support, making optical technology attractive, using optical interposers.

2.2. Soldering

Soldering is a well-known metallurgical joining method that uses a filler metal, the solder, with a melting point below 425 °C. In the immense electronic materials world, soldering plays a crucial role in the assembly and interconnection of the silicon die (or chip). As a joining material, solder provides electrical, thermal and mechanical continuity in electronics assemblies. The performance and quality of the solder are crucial to the integrity of a solder joint, which in turn is vital to the overall functioning of the assembly. Solders are used in different levels of the electronic assembly sequence. As a die bonding material, the solder provides the electrical and mechanical connection between the silicon die and the bonding pad. It also serves as a path for dissipation of the heat generated by the semiconductor. Bonding of the die to a substrate and its encapsulation is referred to as Level 1 packaging. While the predominant method of providing electrical connection to the silicon chip is through wire bonding, the use of solder bumps on the surface of the Si die, instead of wire bonding, gained acceptance recently, due to the higher number of input/output terminals that can be attached to a given area. The flip chip configuration, which is currently used in most of the components like the ones on the scheme of Figure 2, is such an approach. The Si die is turned `upside down', hence flip chip, and mounted on an appropriate substrate. The next level of assembly and interconnect, referred to frequently as Level 2 packaging, is where the component (encapsulated silicon die) is mounted on a PCB. Solder is the primary means of interconnect in Level 2 packaging [6].

2.2.1. Pb-free solders

Eutectic Sn-Pb solders have been used the most notably to attach discrete components to PCBs. However, due to an increased awareness of the potential health hazards associated with the toxicity of lead (Pb) in humans, which can lead to disorders of the nervous and reproductive systems, and also affect neurological and physical development, actions have been taken to eliminates or reduce the use of Pb in a variety of products. Among these are solders used for plumbing, and additives in paint and gasoline since the late 1970s. There has been a growing worldwide movement to eliminate the use of lead in products due mainly to health-related concerns. This is now mandated through European Union (EU) legislation banning the use of lead in electronics products with some exemptions since July of 2006. Environmental issues,

particularly lead elimination, had not received much attention in the electronics industry until the late 1990s when the initial Waste from Electrical and Electronic Equipment (WEEE) Directive was drafted by the EU. It became clear that responsible environmental practices can have a positive impact on business. Failure to embrace prescribed environmental practices would result in a degraded competitive posture and erosion in market share [7]

Besides health and legislation concerns, "green marketing" and mechanical properties enhancement need were important drivers for the ascension of Pb-free solders. Japanese electronics manufacturers took the lead as green solder manufacturers in the early stages and attribute much of their success to the green advertising. As for the mechanical properties improvements, the tight pitches of devices and smaller solder joints for finer-line circuitry demand high mechanical properties, and many lead-free candidate solders exhibit better strength and fatigue life properties than Pb-Sn solders [8]

In order to replace SnPb solder system with a Pb-free solder, a set of criteria was defined to guide the choice for a suitable replacement. It makes clear that some elements should not be the appropriate substitute for Pb regarding large-scale usage, e.g., In for its limited abundance or even Au and Ag due to its high price. The requirements are listed on Table 1. On Table 2, it can be seen that the final price of each solder system is much closer than the individual element price, due to alloying quantity differences between solders, however, solder systems such as SnAgCu are still expensive, costing almost 3 times higher than SnPb [9]. SnZn, followed by Sn-Cu are the cheapest options, however they present problems mainly with oxidization and wetting, respectively, as seen on Table 3, which may halt their market share ascension. Another relevant issue is the requirement for mechanical strength of new solders, as listed on Table 4 [8]. Currently, huge efforts are being made to develop harsh environment resistant semiconductor devices, e.g., SiC JFET for automobile engine compartment, which, when put in an environmental chamber can raise temperature near the solder to around 175°C – it means that solders used on this device should possess high creep resistance and thermal fatigue resistance [10].

Table 1: Pb-free solder criteria and desired attributes. [8]

- Not toxic
- Available in sufficient quantities to meet current and future requirements
- Exhibit sufficient electrical and thermal conductivity
- Possess adequate mechanical properties: strength, toughness, fatigue and creep resistance
- Compatible with typical terminal metallizations (e.g., Cu, Ni, Ag, Au, Sn, etc.)
- Affordable (i.e., economically viable)
- Have acceptable melt and process temperatures
- Not too different from eutectic Sn-Pb
- Avoid deleterious temperature effects on cards, boards, and components
- Low dressing characteristics

Table 2: Major solder alloys melting temperature and relative price compared to SnPb solder. [9]

Solder	Liquidus [ºC]	Price [vs. SnPb]
SnAgCu	~217	2,76
Sn-Cu	~227	1,47
SnAgBi	~211	2,50
SnZn	~199	1,36
SnAg	~221	2,63

Table 3: Major solder alloy systems remarks regarding replecement of SnPb solder. [8]

Alloy system	Remarks
Binary	
Sn-Ag	Fairly high melt temperature (221ºC) Alternative for wave soldering, but cost an issue Some reliability concerns related to Ag3Sn platelet growth
Su-Cu	Fairly high melt temperature (227ºC) Wave solder candidate Only moderate wetting, but sufficient for most applications
Sn-Bi	Not applicable as a general assembly solder due to cost, low melt temperature (138ºC), and availability Good for low-temperature end of a solder hierarchy
Sn-Zn	Cheap Lower melt temperature than most Pb-free solders Zn is highly active , presents potential corrosion and process concerns
Ternary	
Sn-Ag-Cu	Leading candidate system for reflow soldering Lower melt point than Sn-Ag, Sn-Cu binary alloys Adequate wetting, mechanical properties Much reduced Cu scavenger characteristics compared to Sn-Ag
Sn-Ag-Bi	Even lower melt temperature than Su-Ag-Cu Best fatigue characteristics among most popular Pb-free alloys Poses some reliability and end-of-life reclamation concerns
Others additions	
Ag,Al,Bi,Ga,In,Cu	Reduce melting temperature of Sn-based solders, and some enhance mechanical properties
Ni,Sb	Do not reduce the melt temperatureof Sn-based solders, but added to enhance properties

Table 4: Pb-free solders required mechanical properties. [8]

Properties	Remarks
Shear strength	Solder joints typically experience shear loading -Often due to coefficient of thermal expansion (CTE) mismatches
Fatigue resistance	Increased number of consumer electronics products -Particularly communication, handheld devices -Experiences many on/off cycles
Elevated temperature compatibility	Increased applications involving harsh conditions (e.g., vehicle engine compartment) -Needs improved creep resistance and microstructural stability

2.2.2. Recent issues with Pb-free solders

Recently, studies investigate about addition of other elements into these base alloy systems in minor quantities – up to 1% usually. For instance, additions of rare elements (RE) metal and additions of Pd, Cr and Ca into the Sn-0.7 wt.%Cu solder system had similar results – increase on ultimate tensile strength (UTS), creep fatigue and strength and similar melting point, decreased grain size and lowered maximum elongation [11, 12]. Also, mechanical property issues are being addressed [13], as it was reported that the excessive undercooling of Sn-Ag-Cu solder system, which leads to the growth of Ag3Sn intermetallic compound (IMC) blades, is reduced by addition of 4th alloy element – mainly Zn; Zn or Ge, between other elements. These elements can be also added to reduce Cu_3Sn IMC, which grows in the interface between solder and the interconnection material (often Cu) and creates Kirkendall voiding when it is transformed to Cu_6Sn_5 IMC and expands [13, 14]; furthermore, IMC growth control in general is a concern currently, since it can hold the lowest ductility and become a fracture site, especially after aging [13]; another concern is the downsizing of pad opening size, which reduce cross-sectional area of solders, therefore, increasing current density in the solder. Solder's bulk and interfacial microstructure stability must be developed in order to withstand electromigration effects [15].

2.3. Pb-free solder alloys

In this section, aspects of the metallurgy of Pb-free solders are discussed, focusing in the Sn-Cu solder system and further addition of Zn, which is the object of study.

2.3.1. Reactive Wetting

To form a proper metallurgical bond between two metals, wetting must take place. The ability of the molten solder to spread during the soldering process is of prime importance for the formation of a proper metallic bond. Wetting is measured by the contact angle that is formed at the juncture of a solid and a liquid in a particular environment, as shown in Figure 3.

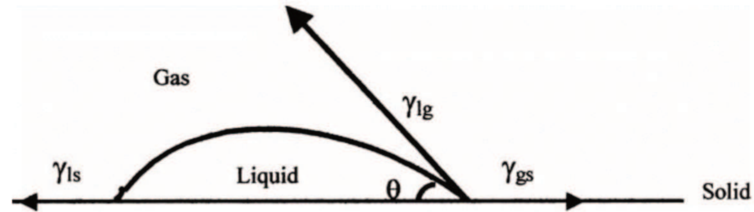

Figure 3: Diagram of wetting angle. [6]

In general, if the wetting or contact angle lies between 0 and 90° the system is said to wet, and if the angle is between 90 and 180°, the system is considered to be non-wetting. The contact angle (θ) is determined from the balance of surface tensions at the juncture, according to the Young-Dupree equation:

$$\gamma_{gs} = \gamma_{ls} + \gamma_{gl} \cos \theta \quad (1)$$

where γ_{gs} is the surface tension of the solid in the particular environment, γ_{ls} is the interfacial energy (surface tension) between the solid and the liquid, and γ_{gl} is the surface tension of the liquid in the same environment. The surface tension of a liquid is a thermodynamic quantity and is defined as the amount of work needed to isothermally enlarge the liquid surface area. The dissolution of the substrate in the molten solder, the oxidation of the flux, the soldering environment, etc., affect the surface tension of solder. The most fundamental characterization of wetting is given by considering the thermodynamics of the wetting forces. In term of free energy, good wetting will occur if there is a net lowering of the total free energy, i.e., the surface energy of the solder is lowered by it forming an interface that is at a lower surface interfacial energy [6].

Other studies indicate that wetting is also affected by the IMC formation driving force [20, 25]. A study on the wetting behavior of Sn-0.7 wt.%Cu-X wt.%Zn (where X was 0, 0.2, 0.5 and 1.0) on Cu substrate was reported. With a wetting balance test, the maximum wetting force was measured, and the contact angle was calculated. Also, the surface tension for each condition was computationally calculated and plotted. The surface tension is ascending with the Zn addition into the system, while the contact angle starts (X = 0 wt.%) at 43°, and has a maximum at 0.5, reaching 53°, and going back to 50° at X = 1.0 wt.%. In Figure 4 (a) it becomes clear that the surface tension has limited influence in the wetting angle. One hypothesis, in the same work, is that the driving force of the first formed IMC in the interface of molten solder and substrate is the major factor of wetting angle. The driving force was calculated and the values for the driving force of IMC formation were plotted for each X composition and the trend of the curve could be compared to the contact angle curve - Figure 4 (b). The driving force curve shows a similar trend with the inverse of the contact angle – there is a minimum value for the driving force at X = 0.5. Therefore, it is believed that the higher the driving force for the formation of the first IMC, the better the wettability [25].

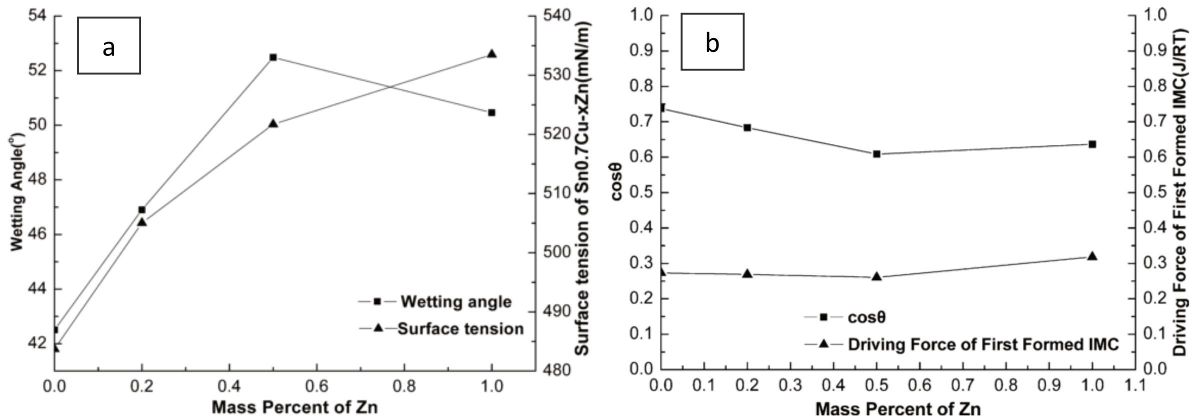

Figure 4: Axis x is the mass percent content of Zn into Sn-0.7 wt.%Cu solder vs.: (a) Wetting angle & Surface tension; and (b) Cosine of wetting angle & Driving force of first formed IMC. [25]

Other factors can affect the wettability as well, for example, roughness of substrate, heterogeneity of the surface, flux type, temperature, trace elements and atmosphere [26]. Wetting balance tests for Sn-0.7 wt.%Cu-X wt.%Zn in air and N_2 atmospheres (on [25]) show that the addition of Zn hindered the wetting force, especially in air atmosphere. This behavior may be attributed to the oxidation of Zn particles in the bulk solder, which would increase the interfacial tension of the solder. In Figure 5 below, it is possible to see that when zinc is added, the maximum wetting force raises.

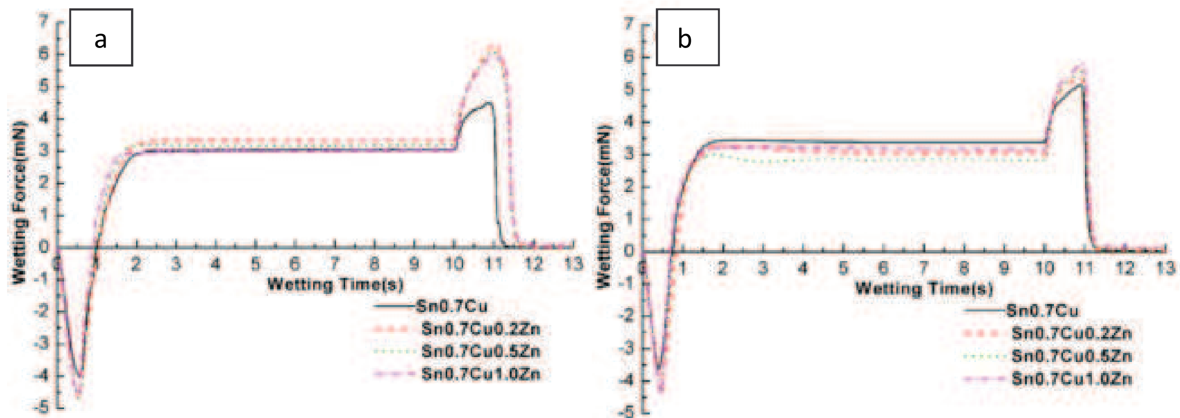

Figure 5: Wetting balance tests of Sn-0.7 wt.%Cu-X wt.%Zn, where X = 0, 0.2, 0.5, 1.0. Atmosphere: (a) in air; (b) in N_2. [25]

The wetting angles for SnPb solder system are considerably lower than Pb-free. For instance, in the work of [17] the wetting angle was measured without flux in vacuum for SnPb and other 4 Pb-free solder systems containing elements such as Ag, Cu and Bi. While the wetting angle of Sn-37 wt.%Pb solder was 13°, for Sn-0.7 wt.%Cu it was 36° (Figure 6 (a)). This work shown as well that the usage of mildly activated rosin (RMA) flux can decrease wetting angle to 20°, under the same temperature as without flux condition (Figure 6 (b)).

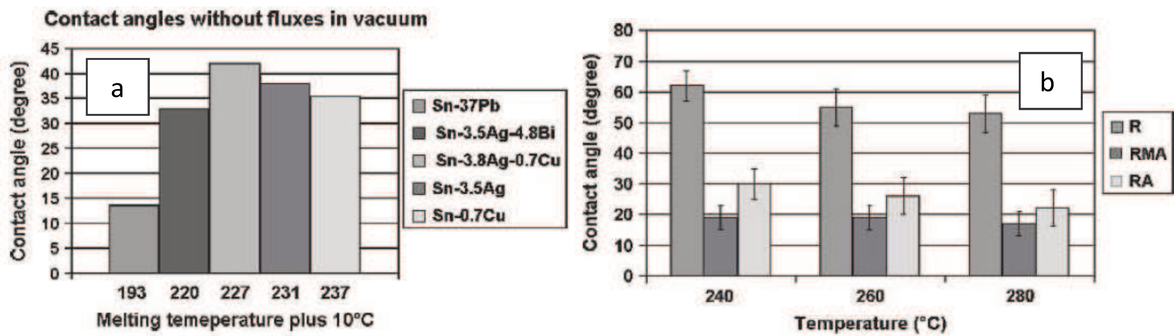

Figure 6: Wetting angle measurements (a) for various solders without flux in vacuum and (b) for Sn-0.7 wt.%Cu solder using three different commercial fluxes. [17]

2.3.2. Interfacial Intermetallic Compound (IMC) Formation

At the interface of the molten solder and the interconnect substrate, the nucleation of the IMC takes place during reflow and it is necessary for good wetting. The thickness of the IMC, however, should not be excessive, since it is a more brittle material than the solder and substrate, which means it may become a site for crack initiation and propagation [18]. The chemical composition of the intermetallic present at the interface of the solder and interconnect is similar between most solders containing Sn, and it will vary depending on amount of alloy elements added and substrate composition.

Using Cu as substrate with a Sn based solder will lead to the formation of Cu_6Sn_5 IMC, with scalloped shape. A study has characterized lead-free and lead-bearing solders after 2 reflows. The reflows took place at 260 °C for lead-free solders and 220 °C for lead-bearing, both with 1 minute above melting temperature. The substrate was a Cu UBM and no-clean flux was used. Micrographs of 4 solders are shown in Figure 7: (a) Eutectic Sn-37 wt.%Pb, (b) Eutectic Sn-3.5 wt.%Ag, (c) Sn-3.8 wt.%Ag-0.7 wt.%Cu, and (d) Sn-0.7 wt.%Cu. It can be noted in this figure that the composition was practically only Cu_6Sn_5 and it had a scalloped shape. Some Cu_3Sn also developed due to the long time exposed to high temperatures, but it is too thin to be observed in these micrographs. The SnPb solder developed a thinner IMC, and it is thought to be due to its Sn lower activity or due to lower Cu dissolution rate on SnPb solder when compared to Pb-free solder systems [19 - 21].

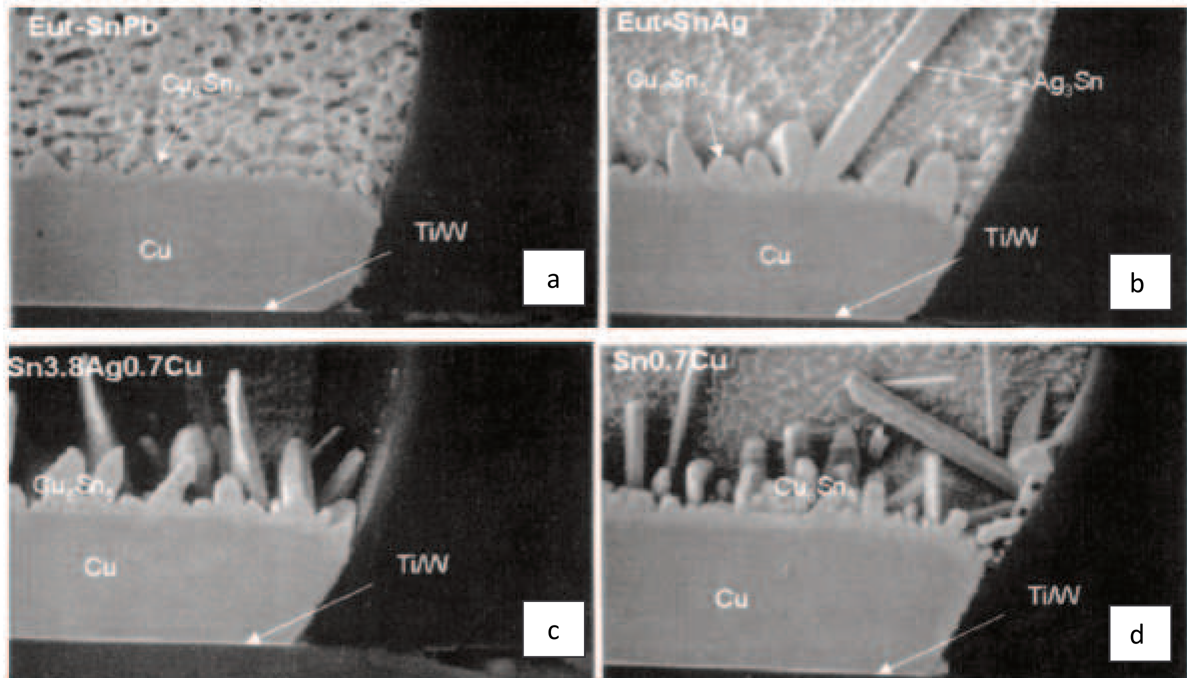

Figure 7: Micrographs of (a) Eutectic Sn-37 wt.%Pb, (b) Eutectic Sn-3.5 wt.%Ag, (c) Sn-3.8 wt.%Ag-0.7 wt.%Cu, and (d) Sn-0.7 wt.%Cu. [19]

A research from Suwoo (1992) about Sn-37 wt.%Pb solder shows that since Pb is almost immiscible with Cu, when a molten solder gets in contact with a Cu substrate, the Cu dissolves into the Sn matrix, and reaches the saturation at around 1.5 wt.%, for 250°C, and the IMC Cu_6Sn_5, also known as η, nucleates at the substrate interface and grows towards the liquid in a hexagonal structure [22].

Chou and Chen have determined experimentally the Sn-Cu-Zn ternary diagram [23], and Yang and Kao have redrawn the Sn rich corner (Figure 8 (a)) [24]. According to these data, the saturation of Cu happens around 1.5 wt.%, and the addition of around 0.5 wt.% Zn has the effect of forming CuZn intermetallic. Wang has used the CALPHAD method to calculate thermodynamically the first IMC formed between Cu and a Sn-0.7 wt.%Cu-X wt.%Zn, where X assumed values from 0.2 to 1.0 wt.%. The driving force for various compounds that were likely to be formed was calculated and the plot can be seen in Figure 8 (b) [25]. These results differ with the data present in the ternary phase diagram in the content of Zn needed to form a CuZn compound, which is around 0.88 wt.%. In Figure 9, the interfacial IMC of a Zn bearing Sn produced on a Cu substrate by 2 minutes reflow can be compared: the solder with 0.5 wt.% Zn formed a thin Cu_6Sn_5 IMC; 0.7 wt.% Zn addition led to CuZn formation, and it was showed in the respective study that it is the first IMC to form and after the Zn go depleted at the interface spalling frequently happens, then, Cu_6Sn_5 is formed underneath; a 2 wt.% addition showed a more stable CuZn IMC [24]. Note that CuZn is represented also as Cu_5Zn_8 in Figure 9. Actually, CuZn is a variation of Cu_5Zn_8, and can be represented as β'-CuZn or γ-CuZn [23, 25]. Kotadia [26] reported that for 1.5 wt.%Zn addition to Sn-0.7 wt.%Cu still spalling may happen, and addition that the of 0.5 wt.%Zn had similar results to Yang and Kao [24].

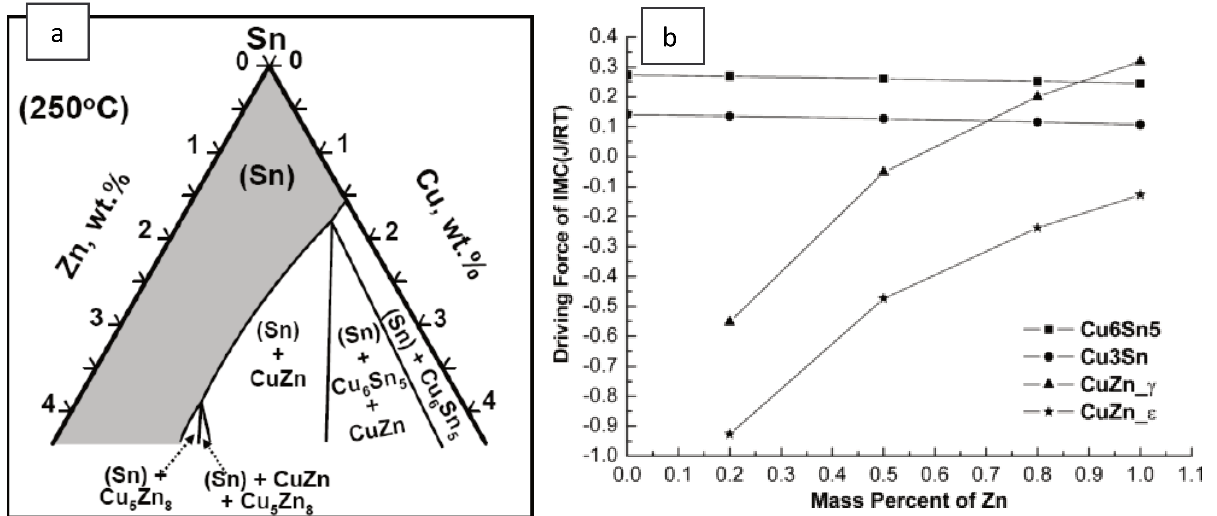

Figure 8: (a) Sn-rich corner of Sn-Cu-Zn system (YANG; KAO; 2006) and (b) calculated driving forces for various IMC formation. [24, 25]

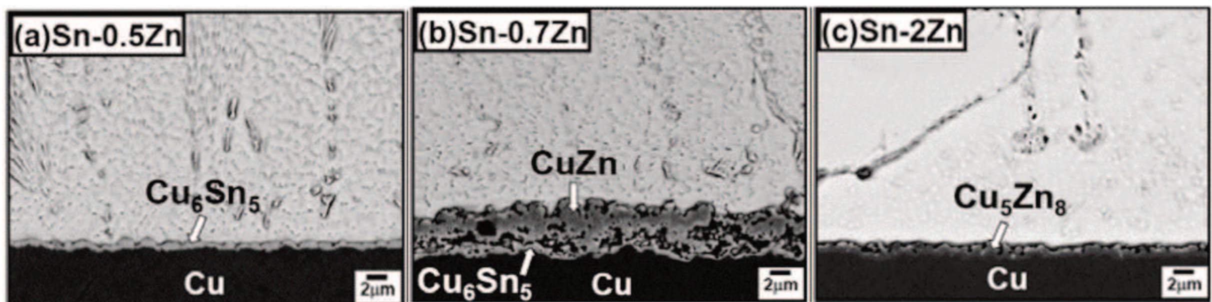

Figure 9: Formation of interfacial IMC between Cu and: (a) Sn-0.5 wt.%Zn; (b) Sn-0.7 wt.%Zn; and (c) Sn-2.0 wt.%Zn. [26]

Other surface finishes have been used successfully in the electronics industry for many years now, such as electroless nickel/immersion gold (Ni-P), which was developed as an alternative to hot air leveled Sn-Pb (HAL). It has been reported that using under bump metallurgy (UBM) leads to formation of Ni_3Sn_4 right at the interface often alongside Cu_6Sn_5 and $(Au,Ni)Sn_4$ [19, 49 - 51]. Figure 10 shows the afore mentioned interfacial structures.

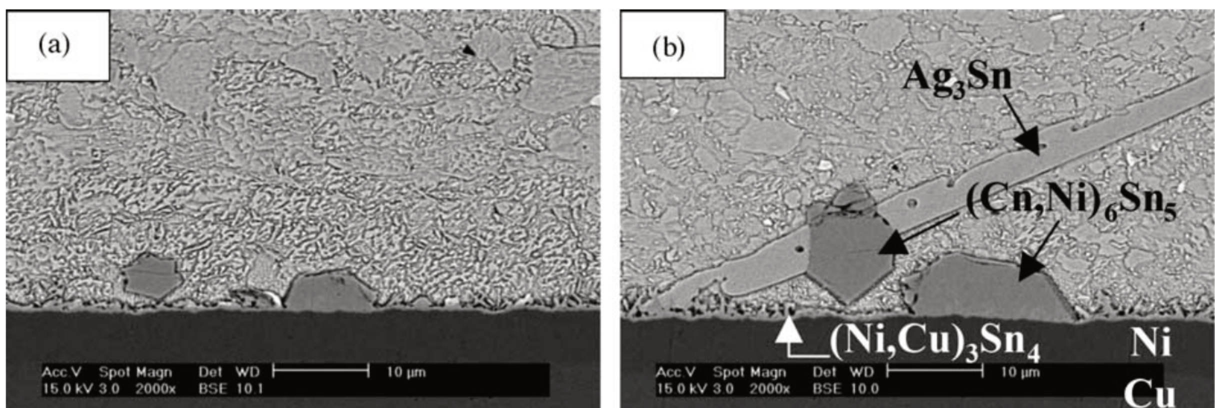

Figure 10: Formation of interfacial IMC between Ni-P and Sn-3.5 wt.%Ag-0.7 wt.%Cu reflowed at 250 °C for two reaction times: (a) 1s; (b) 1 minute. [50]

The evolution of IMC on Pb-free solders under aging has been widely reported by several authors. Besides the concerns over excessive overall growth of the brittle compound at the interface of the solder joint, upon aging the Cu_3Sn compound, also known as ε phase, is formed between the Cu_6Sn_5 and the substrate – where Sn is not abundant –, which, according to Cho [27], is related to appearance of interfacial micro-voids, or Kirkendall Voids, which may cause serious reliability concerns under impact loading conditions. Besides, the void layer can reduce the joint strength of Pb-free solder joints.

Deng drew relevant conclusions about IMC aging on an experiment with a Sn-3.5 wt.%Ag solder on Cu substrate and aging at various temperatures. The solders were formed with 3 different cooling rates after reflow: furnace cooling, air cooling and water quenching. The furnace cooling allows the formation of a thicker initial IMC, due to its prolonged exposure to high temperature. It also forms a more scalloped shape in the IMC, due to the fewer nucleation sites – and consequently larger IMC grains. The samples showed a mixed type of diffusion mechanism, between bulk and grain-boundary diffusion, and it is now clear what was the dominant diffusion mechanism [28]. In Figure 10, micrographs from a Sn-0.7 wt.%Cu solder aged up to 1000 h at 175°C can be seen.

As for the growth rate, two distinct linear regimes were found. At an initial stage, a mainly bulk diffusion is believed to lead the growth of the solder, since it has a more scalloped shape, and thus, a higher surface area for diffusion. This trend was very evident in the furnace-cooled samples, which had a more scalloped IMC morphology. With an increase in time, planarization of the layer took place, resulting in a decrease in the growth rate. These trends are evident in the curves from Figure 12, where the first regime takes place before 50 h for all samples [28].

The initial thickness and morphology had little effect on the Cu_3Sn IMC growth kinetics. This is because the ε phase formed and grew at the η phase/Cu interface during the aging process, primarily at the expense of the η phase, because of the interface reaction between the Cu and the η phase. The morphology of the ε phase was relatively planar and grain-boundary diffusion was the dominant mechanism for growth, while in the η phase, bulk diffusion was more predominant [28].

It should be noted that the intermetallic-layer growth and coarsening of Ag_3Sn particles in the matrix took place concomitantly. The intermetallic layer did not react with Ag_3Sn and engulfed the particles during growth, as shown in Figure 11 (b) and (d) [28]. Thus, although Ag_3Sn may be regarded as an obstacle to Sn diffusion, it can be incorporated into intermetallic layers easily and has little effect on the intermetallic growth kinetics. In this sense, the growth behavior of the SAC solder in this study can be regarded as analogous to other high-Sn solder systems, such as Sn-0.7 wt.%Cu [21, 28].

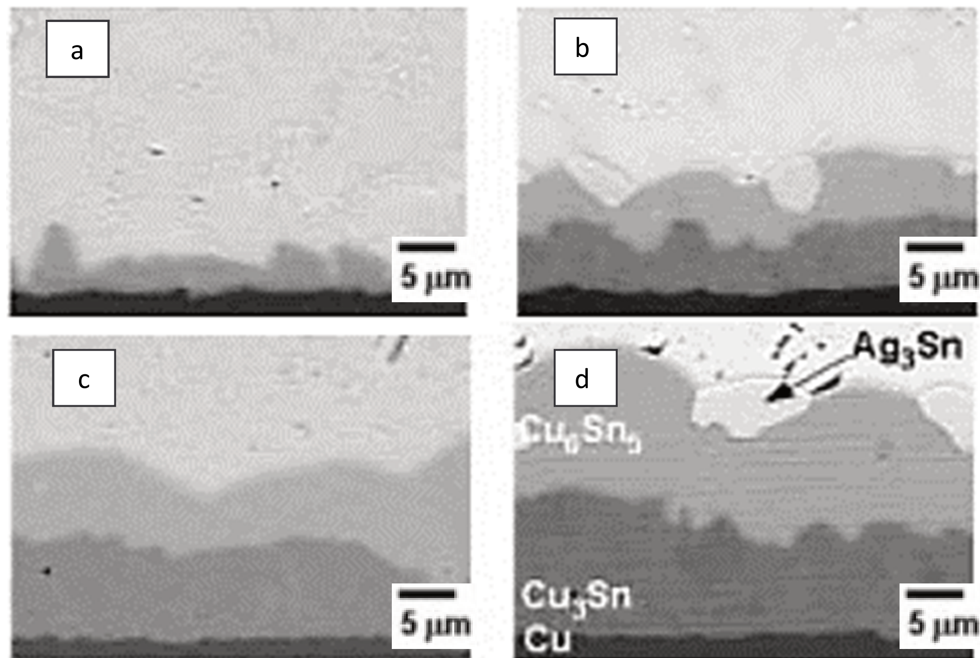

Figure 11: Intermetallic morphology development of an air cooled sample during aging at 175°C (a) 0 h; (b) 170 h; (c) 500 h; and (d) 1000 h. [28]

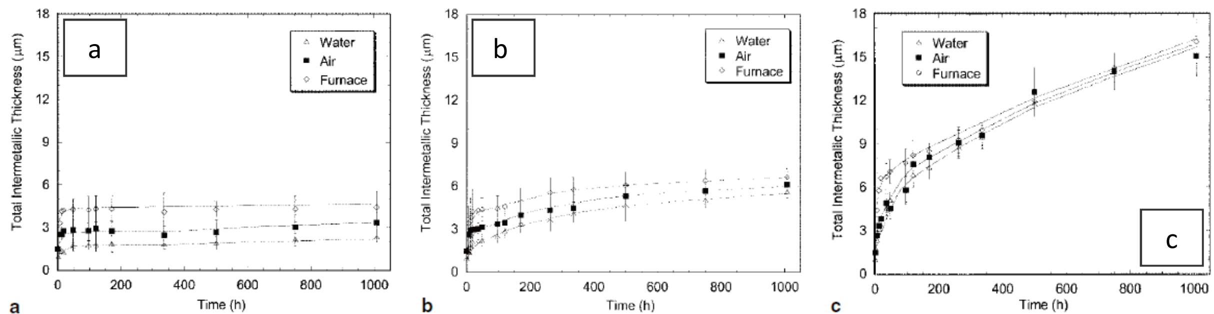

Figure 12: Total intermetallic thickness as a function of aging time for different aging temperatures: (a) 100°C, (b) 140°C, and (c) 175°C. [28]

The formation of Cu_3Sn is closely associated with Cu_6Sn_5. After Cu_6Sn_5 precipitation, a planar Cu_3Sn layer with a thickness more than 250 nm was observed after reflowing pure Sn on a Cu substrate for 4 min at 245 °C. The Cu_3Sn thickness suggested the formation of Cu_3Sn was initiated at the earlier stage of the liquid/substrate reaction. A transmission electronic microscope (TEM) study showed that Cu_3Sn formed after 4–5 s of reflow of eutectic SnBi solder at 170 °C. This means that Cu_3Sn and Cu_6Sn_5 can be formed after a very short reflow at the interface between most Sn-based Pb-free solder alloys and Cu [29].

A scheme of newly formed Cu_3Sn and aged solder interface are depicted on Figure 13 (a) and (b), respectively. On polycrystalline Cu there are many nucleation sites, such as grain boundaries and surface defects. The Cu_3Sn phase can nucleate easily at these defects. Moreover, because of the different growth rates on different crystallographic planes, the growth of Cu_3Sn grains would be highly inhomogeneous between Cu grains of different orientations [30]. It has been reported that the planar morphology of the ε phase is consequence of the high number of grains and random distribution [31].

No matter what morphology the prior Cu_6Sn_5 has, growth of Cu_3Sn is always controlled by grain boundary diffusion. Different to the observation during the liquid state reaction, during

the solid-state reaction, the thickness of Cu_3Sn grows quickly to be comparable to that of Cu_6Sn_5, at the expense of Cu_6Sn_5, as seen on Figure 13 (c). This is because Cu_3Sn is possible to form in two ways: through the reaction of $3Cu + Sn = Cu_3Sn$ at the interface between Cu and Cu_3Sn, and through the reaction of $9Cu + Cu_6Sn_5 = 5Cu_3Sn$ at the interface between Cu_6Sn_5 and Cu_3Sn. At the interface between Cu and Cu_3Sn, the release of Cu atoms from Cu unit lattices is difficult at low homogenous temperature of Cu and the fast grain boundary diffusion of Sn through the Cu_3Sn layer promotes the reaction of $3Cu + Sn = Cu_3Sn$. Note that the molar volume of the newly formed Cu_3Sn is 5 times higher than the previously Cu_6Sn_5, which may contribute to its significant thickness. Moreover, at an aging temperature typically close to 150 °C, the decomposition of Cu_6Sn_5 at the interface between Cu_6Sn_5 and Cu_3Sn can be readily activated [29].

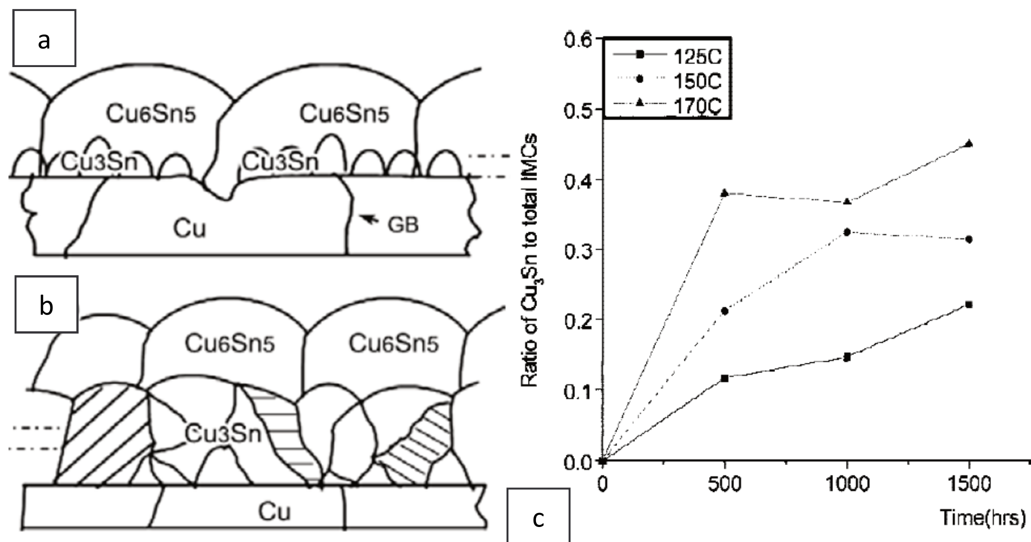

Figure 13: Schematic diagram of the growth of Cu_3Sn on polycrystalline Cu after (a) reflow and (b) solid state aging. (c) Ratio of Cu_3Sn to total IMC thickness of Sn-0.7 wt.%Cu under aging treatment at 120, 150 and 170 °C. [21, 30]

The competitive growth of Cu_6Sn_5 and Cu_3Sn is both diffusion and reaction controlled and multiple parameters such as reaction temperature, reaction time and the surface of the substrate must be considered, which can be discussed using the schematic diagram of the possible inter-diffusion fluxes in a Cu/Sn/Cu sample in Figure 14 [32]. Firstly after a short time of liquid state reaction, Cu_6Sn_5 forms in a scallop shape with nano-scale channels in between and the Cu_3Sn forms in a planar morphology with closer grain boundaries than that in the Cu_6Sn_5 layer. These channels are occupied by the Cu flux from the Cu substrate to Cu_6Sn_5 layer. As a result, it is difficult for Sn to pass through these channels and hence, Sn needs to diffuse through the IMCs to react with Cu at the substrate side [29].

During the liquid reaction, the higher driving force for formation results in the Cu_6Sn_5 precipitating preferentially. While Sn remains, the growth of Cu_3Sn is slow and the Cu_3Sn thickness does not increase clearly during the reaction time from 30 to 60 min. After the liquid state reaction, Cu_6Sn_5 and Cu_3Sn keep growing during the solid state reaction. At temperature around 200 °C the volume diffusion of Sn should be dominant. Currently, to the best of our knowledge, there is no indisputable conclusion on the diffusion between Cu and Sn reaction couples [29].

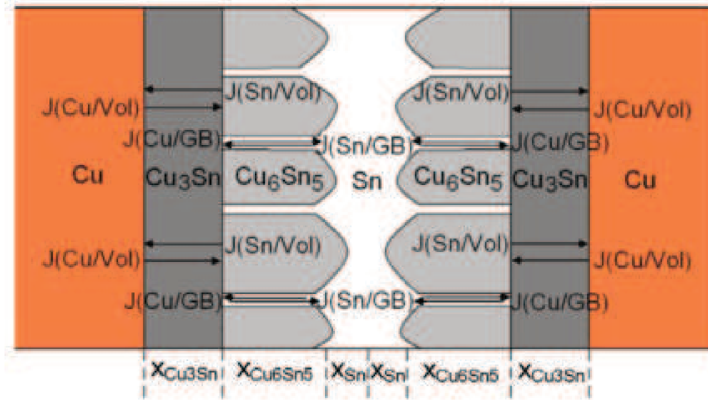

Figure 14: A schematic model of the possible fluxes due to interdiffusion in a Cu/Sn/Cu sample (not to scale). [32]

Many efforts by research groups have been made to find alternatives that mitigate the growth and, hence, the detrimental effects of the Cu_3Sn IMC. Cho has investigated the micro-alloying of Zn into Sn-0.7 wt.%Cu and Sn-3.8 wt.%Ag-0.7 wt.%Cu solders. He found that additions of 0.7 wt.% Zn effectively suppressed the formation of Cu_3Sn [27]. On Figure 15 (a) the results for the SAC-XZn are presented, where X = {0.0, 0.1, 0.4, 0.7}. The mechanism of suppression is still under debate and other researches attempted to find a conclusion to this matter. Figure 15 (d) has the results of total IMC thickness measurement on Sn-0.7 wt.% Cu solder with minor additions of Zn on an electroless nickel immersion gold (ENIG) surface finish, which shows similar trends of Cu UBM, but much smaller values [34].

One of the possible explanations are present in this research by Cho [27], in which he claims that upon reflow, due to the high reactivity of Zn with noble elements, such as Cu, Zn is accumulated at the very interface of the solder and the substrate (Cu in this case), and it reacts with the Cu from the substrate to form a solid solution of Cu-XZn, where X may assume values from 0 to ~35 wt.% (its maximum solubility on Cu at 150 °C). If this is the case, the formation of Cu_3Sn would rely on the Cu from this solid solution following the equation Cu_6Sn_5 + 9Cu (FCC,Cu-XZn) = $5Cu_3Sn$. Since it could drastically decrease the activity of Cu, he calculated with the CALPHAD method, using a thermodynamics computational software, the driving force for Cu_3Sn formation under this new condition. He found that the driving force would decrease up to 20% when Zn accounted for 30 wt.% of the solid solution. It could be enough to suppress the nucleation of Cu_3Sn.

An electron microprobe analysis (EPMA) profile scan was performed at the interface of Cu substrate and Sn-0.7 wt.%Cu and Sn-3.8 wt.%Ag-0.7 wt.%Cu solders, as seen on Figure 15 (b) and (c), respectively, and a consistent amount of Zn was found accumulated there. Cu_3Sn was also found, however it is a very thin layer and its growth might be suppressed due to the Zn accumulation layer. Also, to further investigate the presence of such Cu-Zn solid solution, a solution of NH_4OH and H_2O_2 (3%) in de-ionized (DI) water was applied, which is a known etchant to Cu-Zn solid solutions, and it does not etch Cu-Sn IMCs or Cu. The sample containing 0.4 wt.% Zn showed some etched spots, which match the location of the Zn accumulation layer, and the samples that did not contain Zn addition were not etched by this solution (Figure 16) [27].

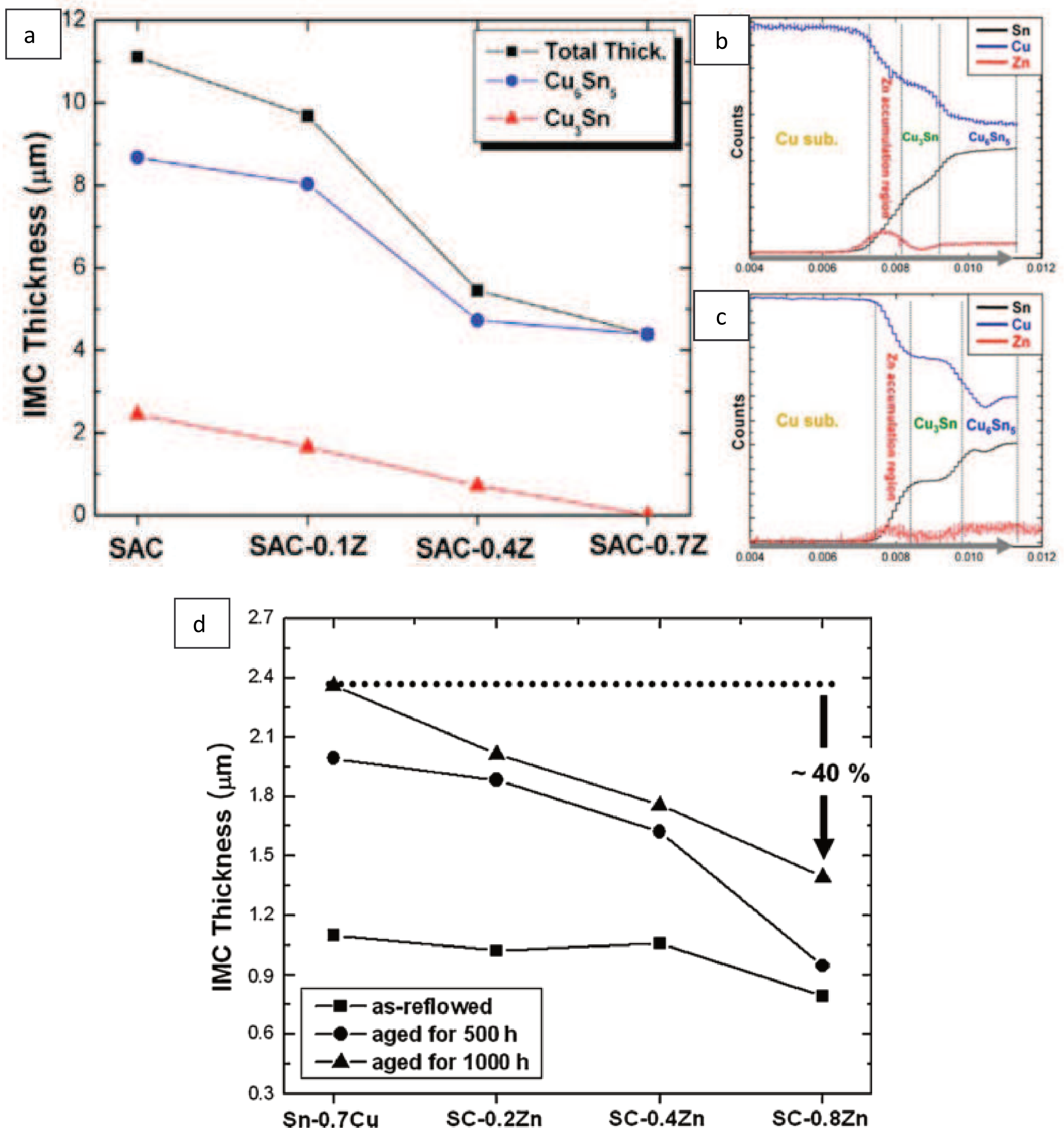

Figure 15: (a) Thickness of each IMC layer as a function of Zn composition in SAC after aging for 1000 h at 150°C on electroplated Cu; and compositional profiles of Sn, Cu and Zn plotted along the distance perpendicular to the IMC interface of (b) Sn-0.7 wt.%Cu-0.4 wt.%Zn and (c) Sn-3.8 wt.%Ag-0.7 wt.%Cu-0.4 wt.%Zn. (d) Thickness of each IMC layer as a function of Zn composition in Sn-0.7 wt.% Cu after aging for 1000 h at 150°C on ENIG UBM. [27, 34]

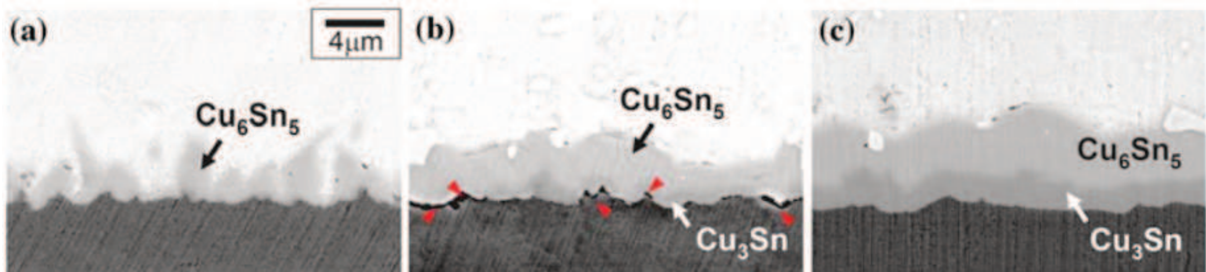

Figure 16: Back-scatted electron images of the interface on Cu that was etched by the solution of NH4OH and H2O2 (3%) in DI water; (a) Sn-3.8Ag-0.7Cu-0.4Zn as-reflowed, (b) Sn-3.8Ag-0.7Cu-0.4Zn aged for 1000 h and (c) Sn-3.8Ag-0.7Cu aged for 1000 h. [27]

2.3.3. Bulk Microstructure

2.3.3.1. Sn-Cu Alloy and Zn addition

The Sn-Cu binary phase diagram has been extensively studied, from which it is possible to make predictions for the microstructure, such as phases compositions and volumes. Recently, an updated Sn-Cu phase diagram was proposed (Figure 17) [54]. The Sn-rich side of the diagram shows that there is an eutectic point at 98.7 atom.% Sn, or 99.1 wt.% Sn, and 227 °C. From 227 to 186 °C, Sn and Cu_6Sn_5 (η) are stable, and below 186 °C, Sn and Cu_6Sn_5 (η'), which means η will form just after reflow, and transformation to η' will happen with aging.

Ventura et. al researched about the solidification behavior of near eutectic Sn-Cu alloys. The eutectic composition of 0.9 wt.% Cu showed a dotted-like dispersed IMC, which grew from fine Cu_6Sn_5 fibers. Lower amount of Cu allows β-Sn to grow as cells and further reduction, as dendrites, and the IMC accumulates on the edges of the dendrites (Figure 18) [55].

Typically, Sn based PB-Free solder balls and interconnects after reflow present considerably either large twin grains, partially interlaced or interlaced grains structure [56 - 60]. Lehman proposed a model for twining nucleus that grow on {101} and {301} plane directions on Sn's BCT lattice, as presented in Figure 19 and 20, and which leads to beach-ball-like or interlaced morphology, respectively. Both structures will present only 3 crystal directions. Such twins are not seen in pure Sn ingots, so it is suggested that β-Sn clings around an impurity and grows epitaxially on the faces of twin nucleus. In Figure 21 some examples of twinned grains are shown, where 21 (a) is fully {101} twin, 21 (b) is partially interlaced, and 21 (c) is fully interlaced. Figure 21 (d) shows electron back-scattered diffraction (EBSD) inverse pole figure (IPF) map from same sample of 21. (c) where there are mainly 3 crystal orientations [56].

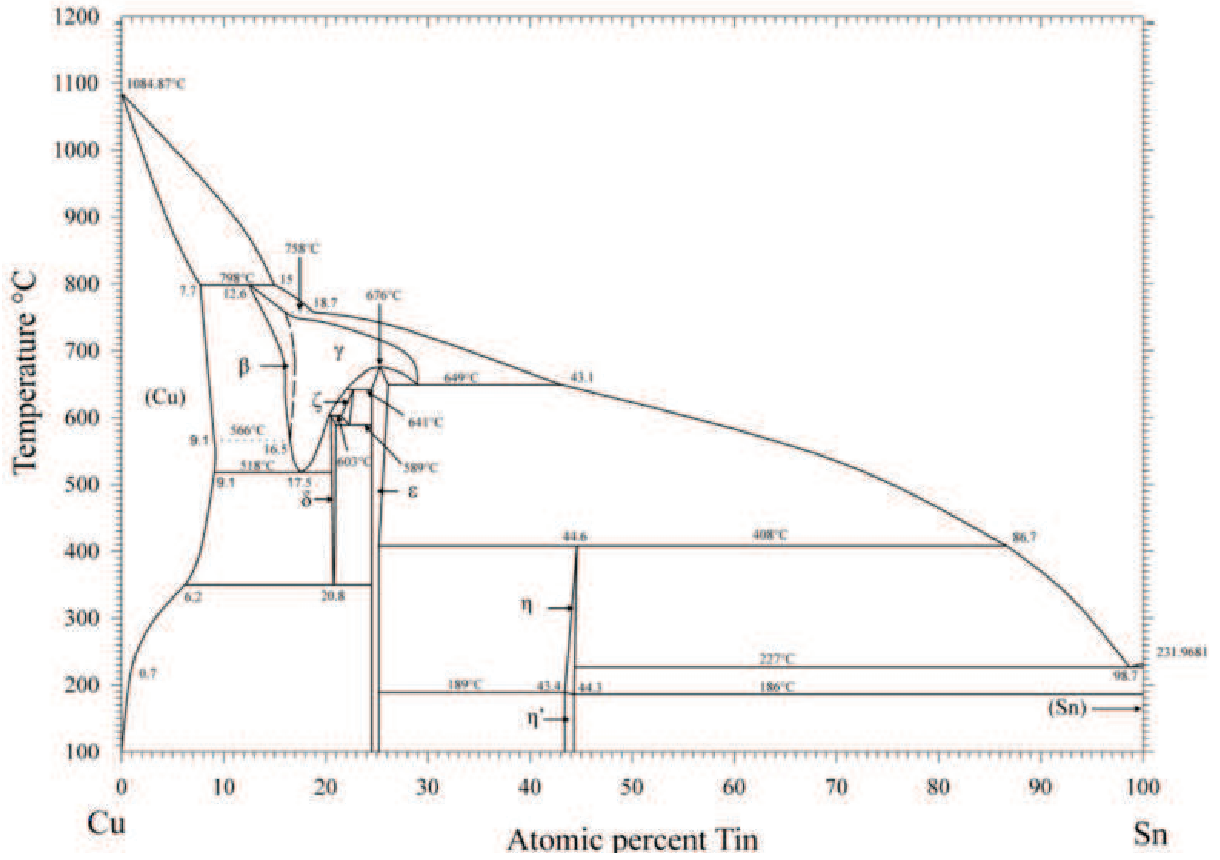

Figure 17: Cu-Sn binary phase diagram. [54]

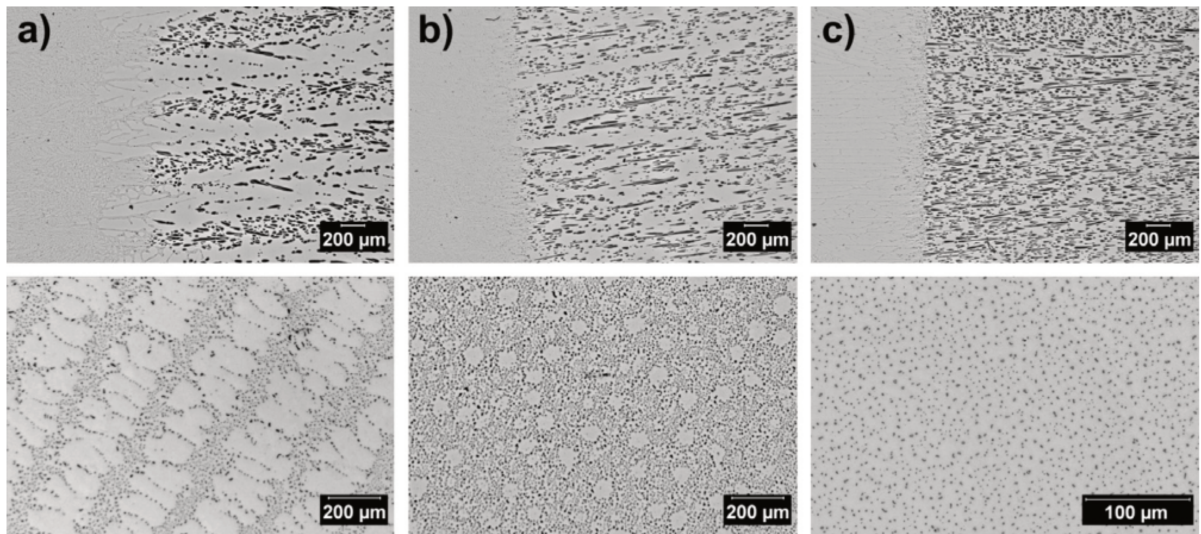

Figure 18: Longitudinal (top) and transverse (bottom) cross-sections of Bridgman's method samples solidified at 10 μm^{-1}. (a) Primary dendrites followed by a eutectic interface (Sn–0.5 Cu), (b) primary cells followed by a eutectic interface (Sn–0.7 Cu) and (c) random distribution of Cu_6Sn_5 fibres (Sn–0.9 Cu). [55]

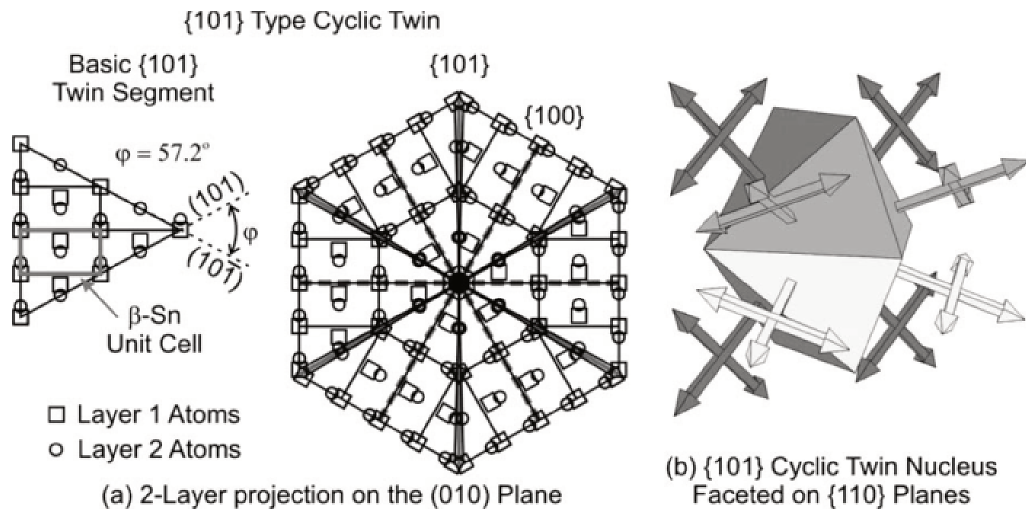

Figure 19: (a) Projection view of Sn lattice onto the (0 1 0) plane, showing a basic {1 0 1} twin segment and a {1 0 1} cyclic twin nucleus. (b) Perspective view of {1 0 1} cyclic twin nucleus faceted on {1 1 0} planes and rendered as planes. [56]

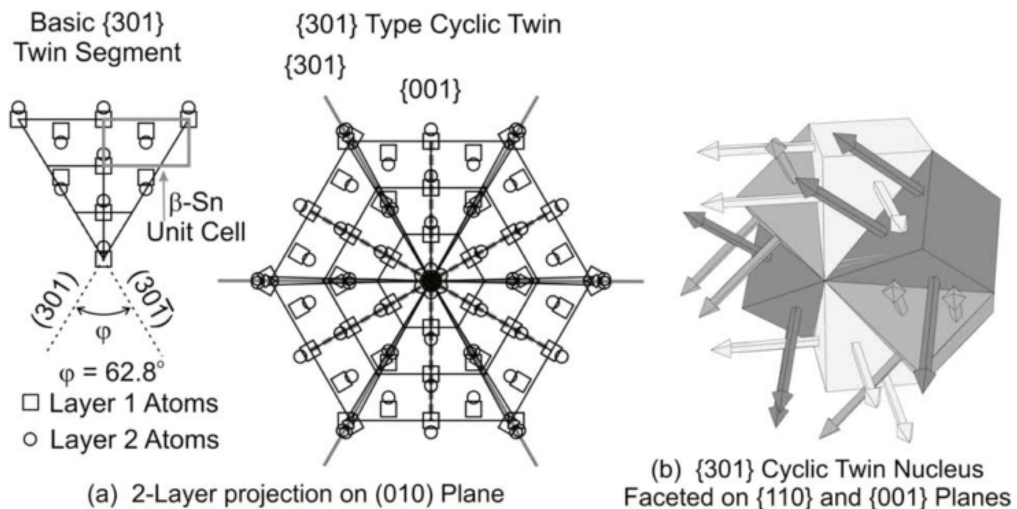

Figure 20: (a) Projection view of Sn lattice onto the (0 1 0) plane, showing a basic {3 0 1} twin segment and a {3 0 1} cyclic twin nucleus. (b) Perspective view of the {3 0 1} cyclic twin nucleus faceted on {1 1 0} and {0 0 1} planes and rendered as planes. [56]

Arfaei investigated the morphology dependence on the solidification temperature of Sn based solders and shows a clear correlation, where the lower the solidification temperature (and thus, higher undercooling degree), the more interlaced, or interpenetrated, the dendrites become. It was suggested that when there is a high undercooling degree, the higher the temperature gradient between the growing dendrite and molten Sn, which can lead to change in the direction of growth [60]. For instance, the samples shown in Figure 21 a, b and c had undercooling of, respectively, 2 K, 45 K and 34 K.

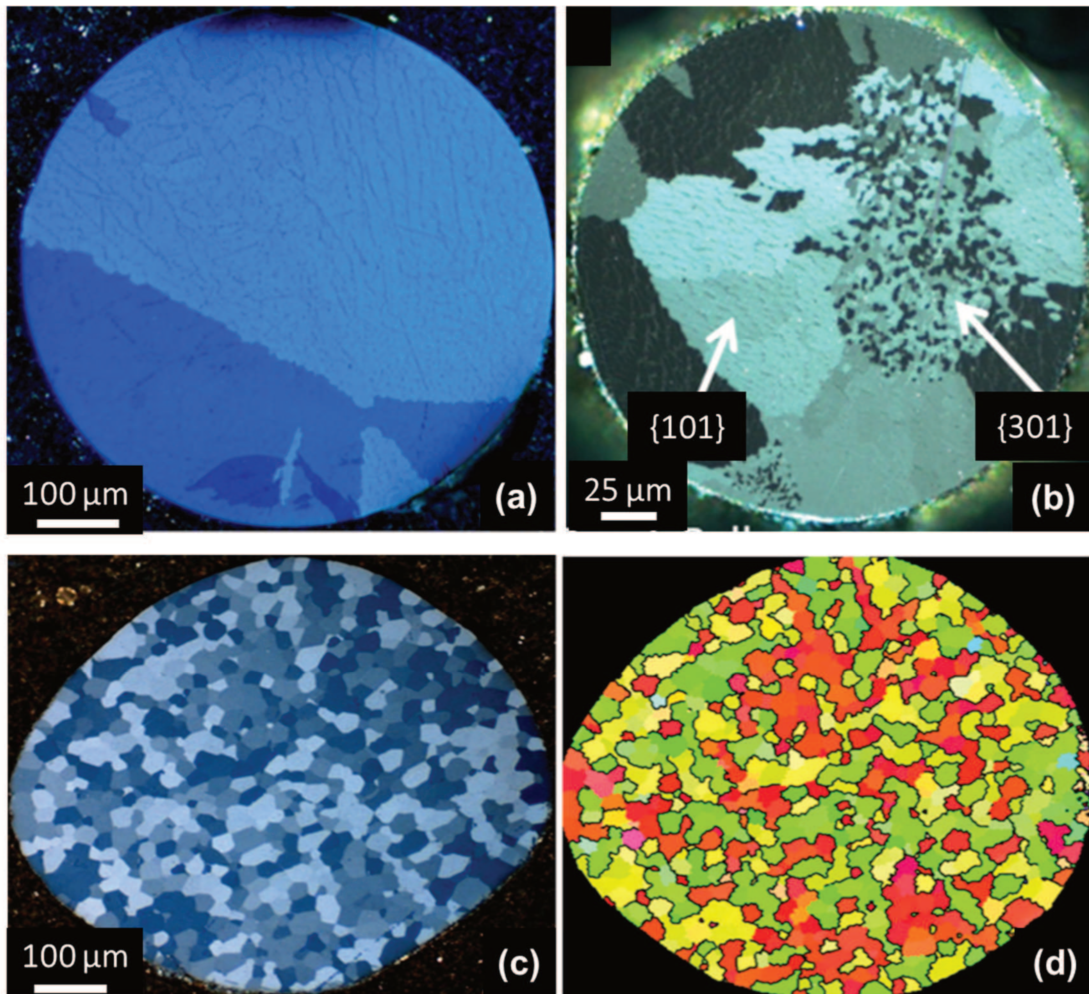

Figure 21: Cross polarized image of cross sectioned Sn based solders: in at.% (a) Sn-0.16 Co; (b) 3.0 Ag-0.5 Cu; (c) Sn-0.44 Ag; and (d) inverse pole figure map of sample (c). [60]

Figure 22 presents a ternary phase diagram of Sn-Cu-Zn system calculated using a constant 99.3 wt.% Sn-0.7 wt.% Cu ration via thermodynamics simulation software using CALPHAD method, and shows that the eutectic happens at around Sn-0.7 wt.% Cu- 0.5 Zn, and the stable phases below melting point are β-Sn, Cu_6Sn_5 and Cu_5Zn_8 [35].

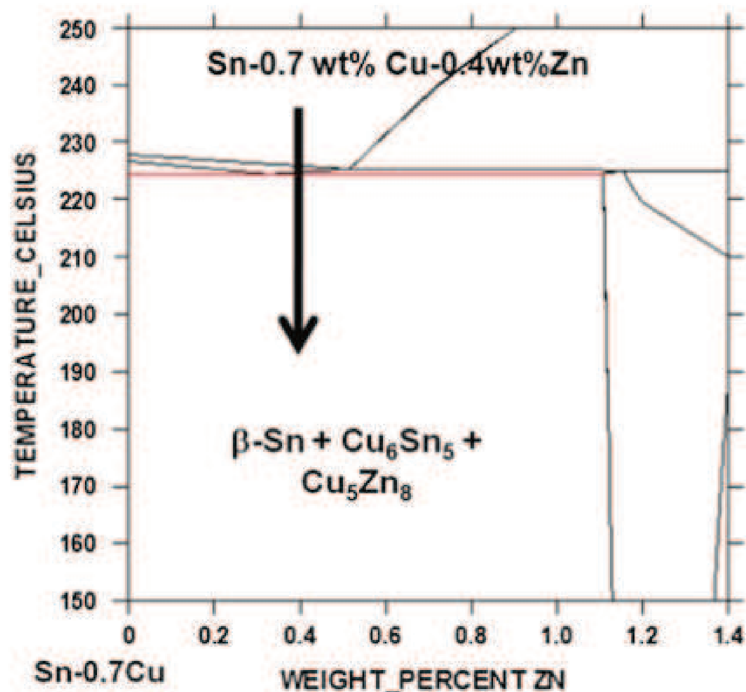

Figure 22: Vertical section of the Sn-Cu-Zn ternary phase diagram calculated along a constant ratio of 99.3Sn:0.7Cu (in wt.%). [35]

2.3.3.2. Effect of Zn on the Undercooling

One of the main characteristics that distinguishes Pb-free form Pb-bearing solders are the IMC structures distributed along the bulk solder: while Pb-bearing solders do not form IMC in the bulk, Pb-free form various IMC depending on the alloying characteristics. An example is shown in the scanning electron microscope (SEM) acquired images on Figure 23, where the eutectic SnPb system can be seen with its grains of Pb and Sn, and no IMC in the bulk (a), the SAC system has the tendency to form Ag3Sn plates, which nucleate from the interfacial Cu_6Sn_5 IMC and grow across the solder – which is a major concern for its mechanical reliability -, and some Cu_6Sn_5 distributed along the bulk (b), and the Sn-Cu system on (c) which presents Cu_6Sn_5 distributed along the bulk, which can sometimes have a needle-like shape [21].

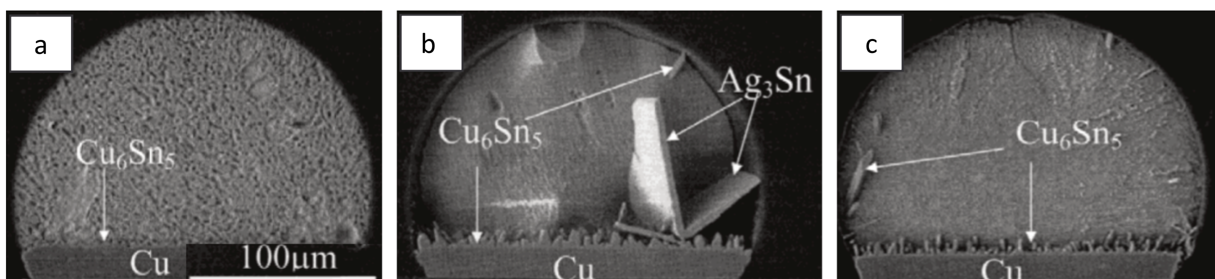

Figure 23: Cross-section SEM micrographs after etching of (a) eutectic SnPb, (b) Sn–3.8 wt.%Ag–0.7 wt.%Cu, and (c) Sn–0.7 wt.%Cu. [21]

Pb-free solders tend to present a large undercooling [13]. Undercooling implies that solidification does not occur even though the liquid phase passes its equilibrium phase-transformation temperature. In other words, the solidification does not occur at the equilibrium

melting point but at a relatively lower temperature. Cho extensively researched the undercooling behavior of electronic solders, and reported the amount of undercooling for several solder systems, such as Sn-0.7 wt.%Cu, Sn-3.5 wt.%Ag and Sn-3.8 wt.%Ag-0.7 wt.%Cu. The value of undercooling for these solders, when soldered on Cu substrate are, respectively: 21.2, 16.1 and 20.7 K. In this case, the phase which is affected by the undercooling effect is β-Sn, while pro-eutectic IMC can freely grow in the molten solder [13]. It was also reported that alloying extra elements to Sn solder with hexagonal close packed (HCP) lattice and a jagged crystal face provide clusters for heterogeneous nucleation due to the low energy between β-Sn and the alloys crystal's jagged faces, which reduces the surface energy between β-Sn solid and liquid, and promotes growth of a β-Sn nuclei, which means that the undercooling is reduced. For instance, the undercooling of pure Sn was measured to be 31.2 K, and the addition of 0.2 wt.% Zn reduces de undercooling to 1.4 K [34]. The undercooling of Sn-0.7 wt.%Cu was measured 36.5 K, and the addition of 0.4 wt.%Zn presented an undercooling of 4.1K [28].

The amount of undercooling also affects the shape and size of β-Sn grains, as well as the distribution of the eutectic phase and intermetallic compounds. In terms of dendritic growth, high undercooling alloys tend to have smaller dendrites due to many intermetallic compounds already nucleated in the liquid, while low undercooling allows the dendrites to grow bigger and the intermetallic compounds will form at the edges of the dendrites. Figure 24 shows the relationship of Zn addition to Sn-1.0 wt.%Ag solder (SA), from 0.2 to 0.6 wt.%Zn, for different cooling rates. It can be seen that SA solder presents many fine twins, while when Zn is added mainly large tiwns appear, for all cooling conditions. The undercooling for SA and additions of 0.2, 0.4 and 0.6 wt.%Zn was, respectively, 32.8, 3.5, 2.0 and 2.1 K. Figure 25 also shows EBSD image of two samples of SA with 0.2 and 0.6 wt.%Zn addition each, and large twins can be seen, as well as a more eutectic structure through the image quality maps, where IMCs appear as a darker shade due to its low difractability [54].

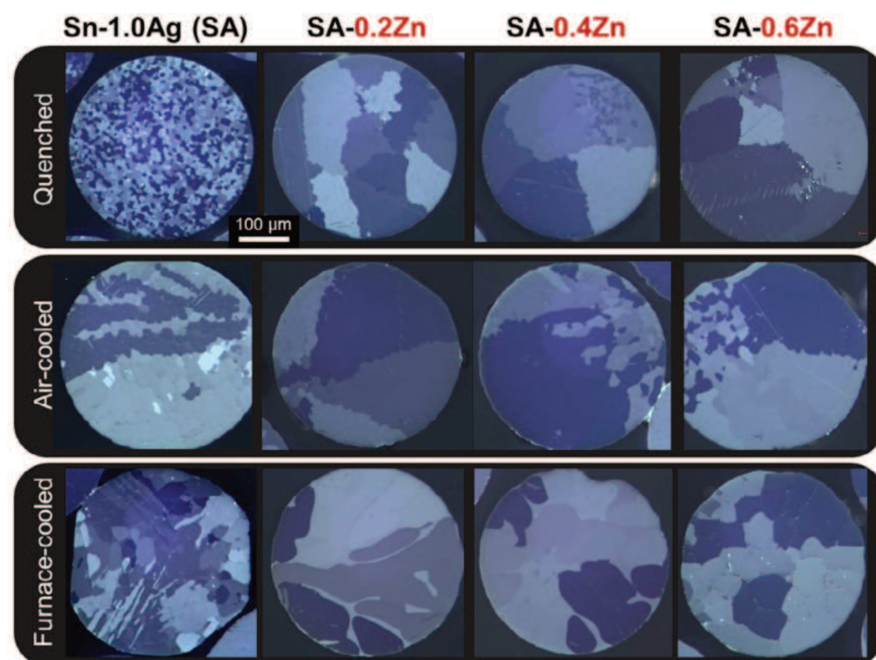

Figure 24: Cross-polarized images of Sn-1.0Ag-Zn solder balls as a function of cooling rate and Zn composition (0 wt.%, 0.2 wt.%, 0.4 wt.%, and 0.6 wt.%). [54]

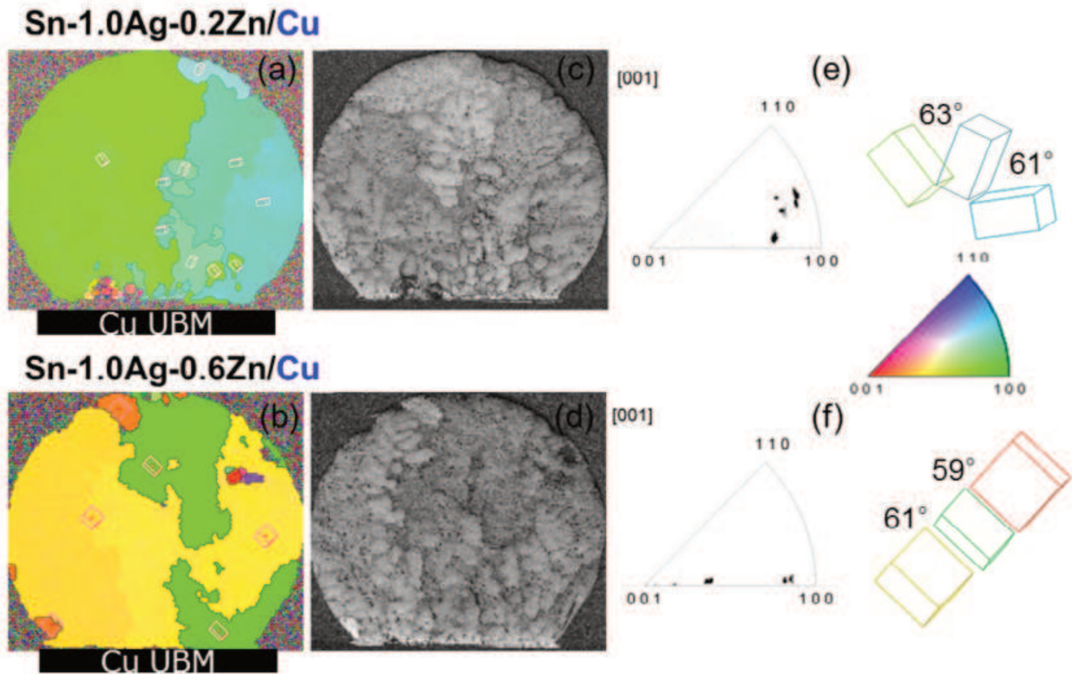

Figure 25: EBSD results of Sn-Ag-Zn/Cu UBM joints; (a) and (b), inverse pole figure maps; (c) and (d), image quality maps; and (e) and (f); inverse pole figures. [54]

For aged samples, as seen in Figure 26, Sn-0.7 wt.%Cu as reflowed has a fine structure of β-Sn and eutectic phases. When Zn is added – from 0.2 to 0.8 wt.% –, a more equiaxied β-Sn and a finer dispersed IMC in the eutectic phase. These solders underwent isothermal aging at 150 °C for 500 h, and are shown in the second row of micrographs on Figure 26. Both β-Sn and eutectic IMC structures had coalesced and formed much bigger structures in comparison with non-aged samples. When Zn was added, the microstructure gets more stable [35]. The main reasons for the microstructure stabilization are: that the IMC, which was previously Cu_6Sn_5, now contains Zn ($(Cu,Zn)_6Sn_5$, where Zn accounts for around 7.7 at% of the total amount of the IMC), and this IMC is somehow more stable than no Zn-containing solder; and also that the IMC gets finely dispersed in the grains and dendrite edges, and this pose as an physical barrier to the coalescence of grains, as can be seen in the Figure 27 (b) below [34]

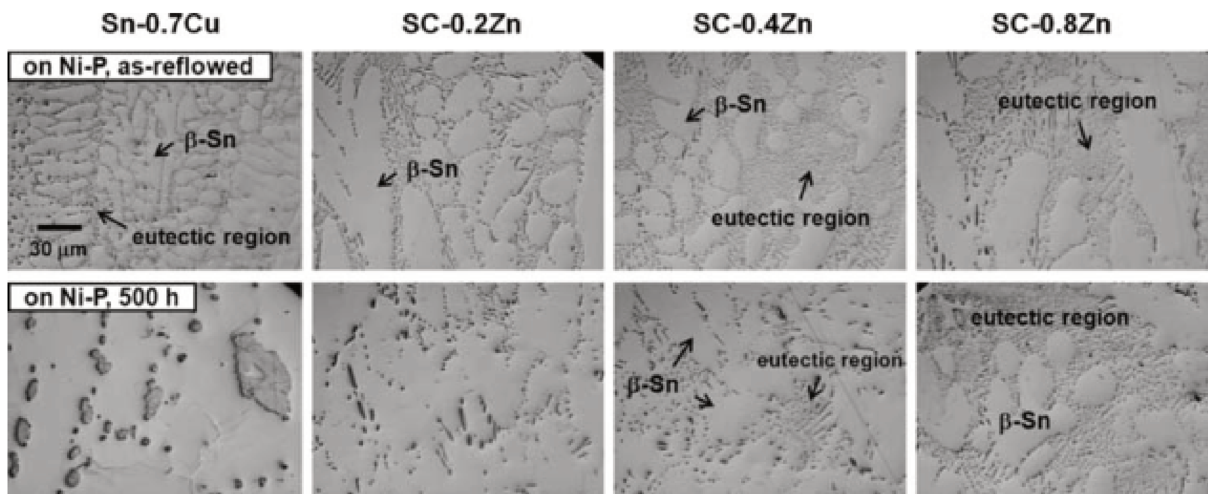

Figure 26: OM images of the four different solders taken far from the interface: as-reflowed (top row) and aged at 150 °C for 500 h (bottom row). [35]

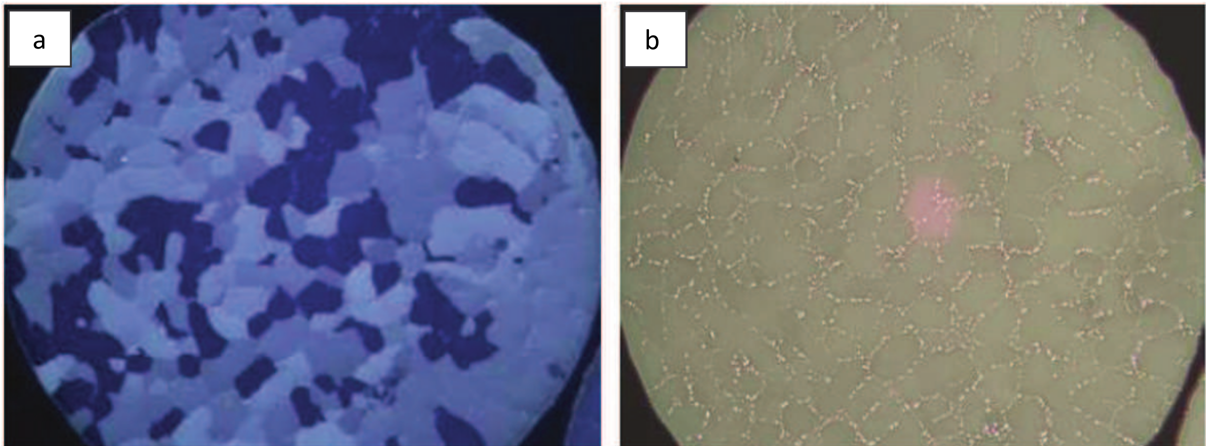

Figure 27: Optical micrographs of Sn1.0Ag0.6Zn solder ball after thermal aging at 200 °C for 8 hrs: (a) cross-polarized micrograph; (b) bright field micrograph. [34]

Seo (2009) also researched about the grain orientation formed in Sn-0.5 wt.%Cu solder using electroless Cu and ENIG surface finishes. He found that usually the grains had a radial orientation, from the UBM towards the surface. And often the solders with Cu UBM had more grains than the ones with Ni(P) UBM. He suggests that this must be due the different amount of impurities in the solder during reflow, coming from the dissolution of the UBM into the solder, which serve as nucleation sites – the solubility of Cu and Ni into a Sn-rich Sn-Cu alloy at 250 °C are, respectively, 1.3 and 0.06 wt.%. Figure 28 shows two solders using Cu and Ni(P) UBM each. The shape of the grains is narrow near the interface and larger near the outer surface, and this may indicate that the nucleation point was near the interface, according to Lehman's (2010) proposal – Sn dendrites grow fast and release latent heat of fusion, which heats up the melt and suppresses the growth of clusters away from initial nucleation sites [63].

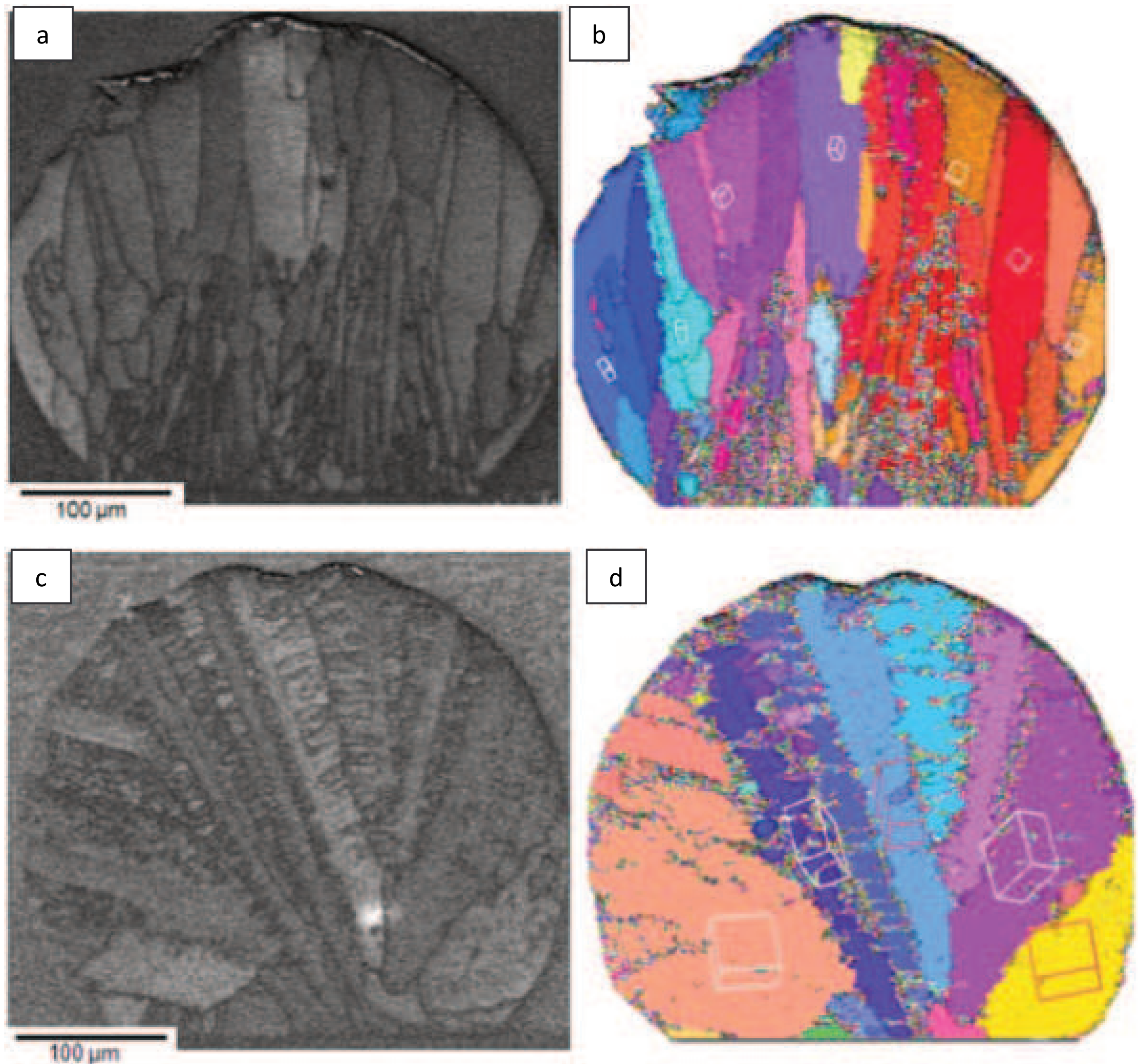

Figure 28: Respectively, EBSD image quality and inverse pole figure map for Sn-0.5 wt.% Cu onto: (a) and (b) electroless Cu UBM, and (c) and (d) ENIG UBM. [63]

2.3.4. Solder strength

The solder microstrucure strongly affects the mechanical reliability of the joint. For example, if IMCs' shapes and sizes in the bulk are plate-shaped, or considerably large, they are in general potential path for cracks [65]; large grains will increase the joint tenacity, however, if the grain is oriented parallel to the substrate, shear forces can easily propagate cracks, due to the tetragonal lattice of β-grains which cause anisotropy [58], and are prone to ductile creep failure; large IMC or microvoiding can propagate cracks due to its brittle nature [39, 64].

To assess the mechanical reliability of solders is crucial for the development of new solders. For instance, the shear strength is an important feature, due to the fact that the joint must withstand high shear stress originated from the coefficient thermal expansion (CTE) mismatch of the components in electronic applications [62].

Another way to assess the solder strenght is through its microhardness, and it has been reported that it is closely related to the microstructure of the solder matrix. Seo has measured the microhardness of aged samples at various temperatures and aging times and Sn-based Pb-free solders. Finely dispersed IMC along the bulk and smaller grains solder present a higher hardness. Short-time aging experiments showed a decrease in grain size, and longer aging imes promote growth of grains and bulk IMCs [71]. The decrease in grain size may be due to dynamic precipitation of IMCs along β-Sn dendrites' grain-boundaries or subgrain-boundaries, which promotes recrystallization of grains [71, 72].

2.3.5. Electromigration

2.3.5.1. Electromigration Kinetics

The term electromigration refers to mass motion under the influence of high current density. The transport of mass in metals is governed mainly by the momentum exchange between the charge carriers moving under the applied field and the thermally activated ions of the metal. The electrostatic force generally plays a relatively minor role [37]. The mass flow is also influenced by chemical, thermal and mechanical forces within the solder [38].

Several studies have addressed the kinetics and mechanisms of mass flow and microstructure evolution of solders under EM influence, but there is no undisputable explanation for this complicated phenomena. Nevertheless, the total mass flux (J_{total}) during the application of high current into a solder is usually represented by the equation below, which is the sum of the components affected by the following driving forces: difference of the chemical potential (J_{chem}); electromigration forces (J_{EM}); and back stress (J_{σ}) [39]:

$$J_{total} = J_{chem} + J_{EM} + J_{\sigma} \tag{2}$$

The mass flux can be explained following the definition that the mass flux is given by the product

$$J_i = C_i v_i \tag{3}$$

where the subscript i is the diffusing specimen, C is the concentration and v is the drift velocity. According to the Nernst-Einstein relation, the drift velocity is related to its driving force through:

$$v_i = \frac{DF}{kT} \tag{4}$$

where F is the driving force, k is the Boltzmann's constant, T is the absolute temperature and D is the diffusion coefficient, which is a function of the temperature and is given by $D = D_0 e^{-Q/kT}$, where D_0 is the maximum diffusion coefficient and Q is the activation energy.

The J_{chem} is basically described by Fick's law of diffusion. In diffusion-controlled phase transformations in alloys there usually exists a composition gradient, which gives a chemical potential gradient μ_i, or:

$$F_{chem} = kT\left(\frac{\partial \ln Ci}{\partial x}\right) \tag{5}$$

where x is displacement into the material.

Huntington and Grone (1961) proposed that the force caused by electromigration can be described by:

$$F_{EM} = eEZ^* = eE(Z_{el} + Z_{wd}) \quad (6)$$

where e is the charge of an electron, E is the electric field and Z^* is the effective charge number of electromigration. It can be divided in two parts: Z_{el} is the ion's nominal valence. It varies from zero up to the full valence of the atom, depending on how much screening effect is assumed; Z_{wd} is the effective charge number due to the "wind force", arising because of the momentum exchange between the moving charge carriers and the thermally activated ions. Z_{wd} is regarded as much larger than Z_{el} [70].

As put by Conrad, the drift of atoms generally occurs from cathode to anode, leaving behind an excess concentration of vacancies in the vicinity of the cathode and an accumulation of atoms at the anode. This results in an opposing chemical potential gradient $\partial(\mu_a - \mu_v)/\partial x$ which gives a back force:

$$F_\sigma = -\Omega\frac{\partial\sigma}{\partial x} \quad (7)$$

where μ_a is the chemical potential of the atoms, μ_v that of the vacancies, Ω the atomic volume and σ is the hydrostatic stress in the metal [40].

The steady-state flux is then given by combining equations (3) through (7), J_{total} can be written as below.

$$J_{total} = \frac{CD}{kT}\left(kT\left(\frac{\partial \ln C}{\partial x}\right) + eEZ* - \Omega\frac{\partial\sigma}{\partial x}\right) \quad (8)$$

Some authors include in this formula other driving forces for mass flux during high current density application, such as thermomigration, which is the flow of material caused by temperature gradient [41], or dissolution of interfacial IMC into the bulk [42], however these phenomena apparently contribute little to the microstructure evolution.

2.3.5.2. Polarity and Reverse Polarity Effects

Both noble and near-noble metals react with Sn to form IMCs at room temperature due to fast interstitial diffusion. Since the IMCs formed at the solder joint interfaces are an integral part of the joint, they must be considered together with the solder bump in electromigration. Because of fast diffusion and rapid reaction, the chemical and electrical forces interact at these interfaces. However, the interactions at the cathode and the anode are different due to the polarity effect. At the cathode, the electrons flow from the IMC to solder, but at the anode the flow direction is reversed. While electromigration enhances IMC formation at the anode, it enhances IMC dissolution at the cathode [43].

To investigate the polarity effect, Gan and Tu have designed experiments with Sn-3.8 wt.%Ag-0.7 wt.%Cu solder in "V-groove" samples, which means it was a V-like cavity into Si wafer, with width and length of 100 μm and 200 μm respectively, filled with SAC solder and connected to Cu lines in each edge. Temperatures from 120 to 180 °C and current density in the order of 10^4 A/cm² [39].

Figure 19 demonstrates the thickness change of IMCs at the anode and cathode, after current stressing for 0, 10, 21, and 87 h, with a current density of 3.2e+04 A/cm² at 180 °C. The pictures

in the left column are for the anode side and those in the right column are for the cathode. The direction of electron flow is indicated by the vertical arrows with symbol e– in Figure 29. Although the growth rate of IMCs is much different between the anode and the cathode due to the polarity of electric current, the same type of IMCs of Cu_6Sn_5 and Cu_3Sn formed at both interfaces, independent of the direction of electric current. As shown in Figures 29 (a) and (b), the scallop-type Cu_6Sn_5 compounds formed at the solder/Cu interfaces in the initial stage, that is after reflow, and transformed into layer-type after current stressing for 10 h, as shown in Figures 29 (c) and (d). There is always a very thin layer of Cu_3Sn compound formed between Cu_6Sn_5 and Cu, although it is difficult to tell from the SEM images at the initial stage. At the anode, as shown in the left column in Figure 29, both Cu_6Sn_5 and Cu_3Sn layers grew with current stressing time. The total thickness approached 10 µm after 87 h, which is comparable with that of thermal annealing for 200 h at the same temperature. The IMC layer at the anode side was always much thicker than that at the cathode side after same current stressing time, as indicated by the side arrows. In comparison with the case of thermal annealing without current, there were fewer Kirkendall voids formed at the anode side, along the Cu_3Sn/Cu interface, although the IMCs were much thicker. Under the current effect, the vacancy flux moved away from the anode, became supersaturated, and then condensed to form voids at the cathode side, as shown in Figure 29 (h).

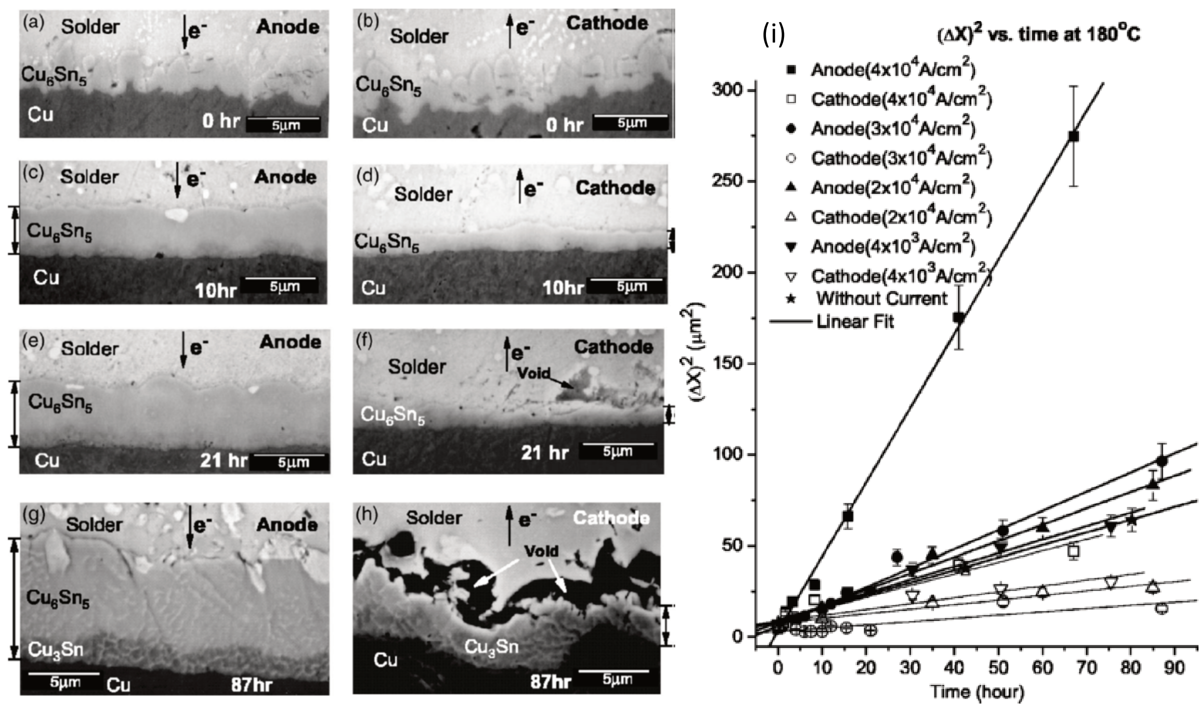

Figure 29: Isothermal EM stressing of Sn-3.8 wt.%Ag-0.7 wt.%Cu solder at 180 °C. (a) to (h): SEM images of microstructure evolution due to 3.2e+04 A/cm² current density EM stressing. (i): Total thickness [$(\Delta x)^2$] change of IMCs with time at various current densities. [39]

As shown in Fig 29 (i), several phenomena are taking place for IMC growth. First, the growth of IMC at the anode has a parabolic dependence on time since the square of thickness $(\Delta x)^2$ increases linearly with time. Second, electric current enhances the growth of IMC at the anode and retards it at the cathode due to the polarity of the current. Third, IMC grows more quickly with higher current density at the anode. After the same stressing time, the sample with the largest current density 4e+04 A/cm² has the thickest IMC, and the one with the lowest current density 4e+03 A/cm² has the thinnest IMC, slightly thicker than that in the no-current

case. Finally, the thickness of the IMC at the cathode is close to the initial thickness (around 2.5 µm) or below, not changing as much as that at the anode. Reportedly, the reduction of the IMC thickness is due to dissolution of IMC into the bulk assisted by the EM driving force and high temperature [42].

As seen in Eq. (8), the EM influence depends on intrinsic properties of the diffusing species, hence, each solder system will have different characteristics upon EM stressing. Recently researchers have studied the characteristics of Sn-based solders containing Zn, and its response to EM stress is in reverse of response by alloying elements such as Cu, Ag or Ni.

Zhang and Guo evaluated the EM characteristics of Sn-9.0 wt.%Zn under current density of 3.87 A/cm², and they found that although the IMC type is the same as formed after reflow and during aging, unlike in a solder such as SAC, the accumulation of IMC after EM stress was higher in the cathode than in the anode, as it can be seen in Figure 30. They found, however, that Sn still accumulated at the anode, as expected, but Zn migrated towards the cathode and formed a Cu-Zn based IMC [44].

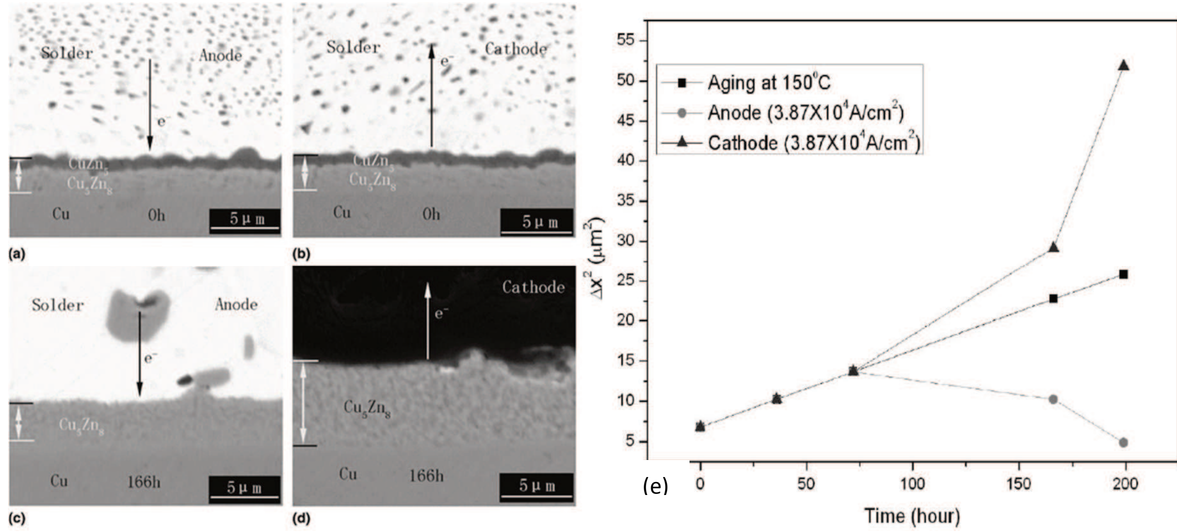

Figure 30: Isothermal EM stressing of Sn-9.0 wt.%Zn solder at 150 ±5 °C at current density of 3.87e+04 A/cm². (a) to (d) SEM images of IMCs at the anode (left column) and the cathode (right column) (e) Total thickness [(Δx)²] change of IMCs with time. [44]

Since the main difference between cathode and anode was the direction of the electron flow. If only the electrowind force is considered, these results are unexpected, since zinc's Z^* is negative, as is for Sn, so that a normal polarity effect was expected. Zhang and Guo explained this effect by comparing the backstress force, which is caused by vacancies accumulation at the cathode and are the same for all diffusing species, and the EM force acting on Sn and Zn, which have different value due to a different Z^*. They found that since Zn possess a much lower Z^* than Sn, -2 and -18 respectively, the EM force acting upon Zn could not overcome the backstress force, which push atoms towards the cathode, whereas in the Sn case the EM force was enough to push it towards the cathode [44]. This difference can be represented by the following inequality:

$$\frac{Z_{Zn}^* \, eE_{Zn}}{\Omega_{zn}} < \frac{\partial \sigma}{\partial x} < \frac{Z_{Sn}^* \, eE_{Sn}}{\Omega_{Sn}} \tag{9}$$

Liu et al studied the influence of EM on a SAC solder and further addition of Zn. Figure 31 shows the results of 100 hours of EM stressing at current density of 2e+04 A/cm² and 150 °C for Sn–1.0 wt.%Ag–0.5 wt.%Cu and Sn–1.0 wt.%Ag–0.5 wt.%Cu-1.0 wt.%Zn solders. The solder without Zn showed a normal polarity effect, with IMC formation near the anode and complete depletion of IMC at the cathode, whereas the one containing Zn showed a both sides with virtually the same thickness, which is claimed to be due the reverse polarity of Zn [45].

It is worthy to mention that the SAC solder with Zn showed a much higher microstructure stability, which may be a good result in terms of improving the joint reliability though addition of 1 wt.% Zn.

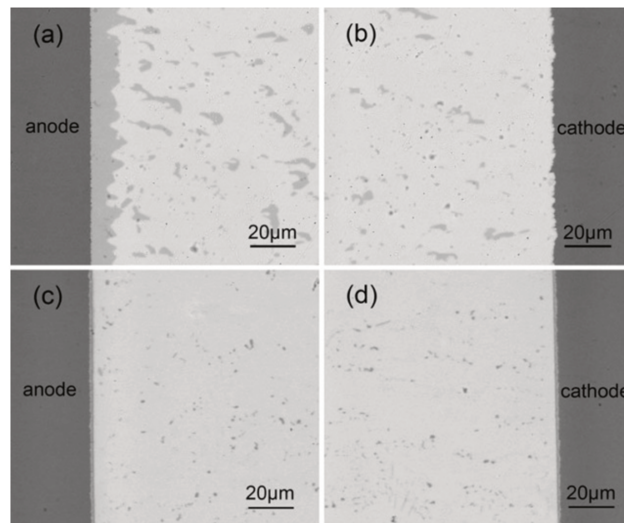

Figure 31: Interface morphology of Sn–1.0 wt.%Ag–0.5 wt.%Cu (a) and (b), and Sn–1.0 wt.%Ag–0.5 wt.%Cu-1.0 wt.%Zn (c) and (d) solder joints both after electromigration for 100 h under current density of 2e+04 A/cm². The anodes are to the left and cathodes to the right. [45]

2.3.5.3. Current Crowding

The current crowding is an important effect for electrical circuits and joints. The electron flow is not uniform through the cross sectional area of a conductor, especially if there are changes in the geometry.

For solder joints, the nominal current density i is calculated through $i = I / A$, where I is the current (A) and A is the area of the pad opening (cm²). However, due to abrupt changes in cross section area from the solder to the conductor lines inside the substrate or component, the current accumulates near the joints. Figure 32 below shows through a simulation that the accumulation of electron flow inside a solder joint may reach up to a current density of 10^5 A/cm² [41]

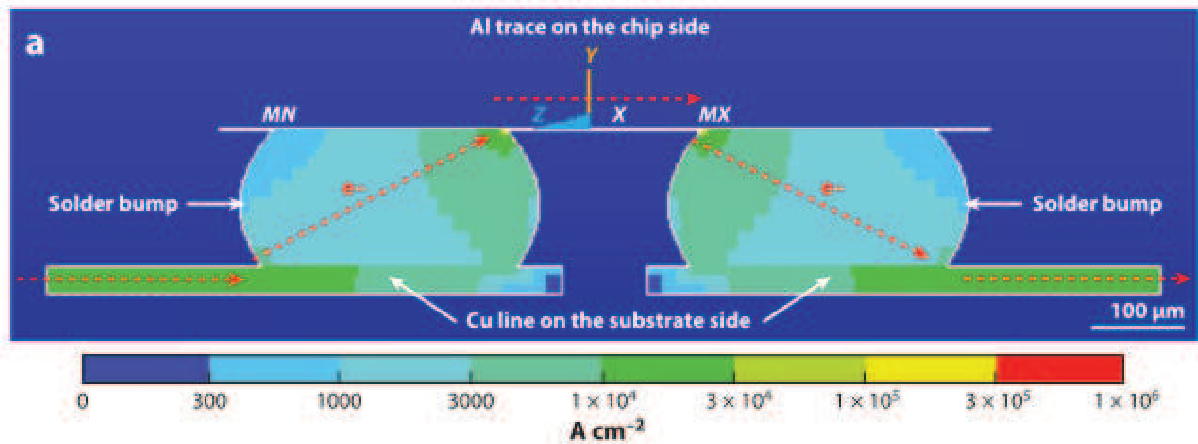

Figure 32: Cross-sectional view showing the current-crowding effect in solder bumps during current stressing. Peak current density occurs at the current entrances of the Al trace into the solder bump. [41]

The accumulation of current near the solder joints causes uneven joule heating and also enhanced dissolution and drift of atoms due to electromigration. Many authors, including Yeh et al, propose that the mass depletion due to EM near the solder joints associated with current crowding reduce significantly the lifetime of a solder under high current stress by nucleating and propagating voids at the interface. A scheme of such mechanism is depicted below on Figure 33 [46].

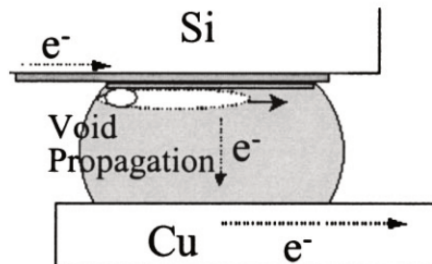

Figure 33: Void propagation in a solder joint assisted by current crowding effect. [46]

2.3.5.4. Anisotropy diffusivity in β-Sn

A notable characteristic of noble elements, such as Cu, Ag and Zn, which diffuse interstitially in a β-Sn matrix solder – the main microstructure present in Sn-based solders –, is that their diffusivity varies inside β-Sn. This is due to the crystallography of β-Sn, which is monoclinic, and have an easier pathway for diffusion along its *c* axis. P. Liu et al used simulation to calculate the activation energy of diffusion in different axis for various elements and found a similar trend with experimental results from literature. Figure 34 shows on (a) a scheme of the diffusion pathway (red dotted line) in a monoclinic crystal lattice, on a vertical *c* axis and horizontal *a* axis, and on (b) and (c) the calculated activation energy to move into this pathway for Ag and Cu. For Cu, the activation energy reached 0.40 eV in the *c* axis and 0.69 eV in the *a* axis. Ag had a similar trend. The author also found that Cu is the fastest diffusion element on β-Sn among noble elements, and that Cu may slow down the substitutional diffusion of Sn, regarded as Sn self-diffusion, by moving from interstitial to vacancies created by a Sn diffusion species, which means that it occupies and blocks the diffusion pathway of Sn [47].

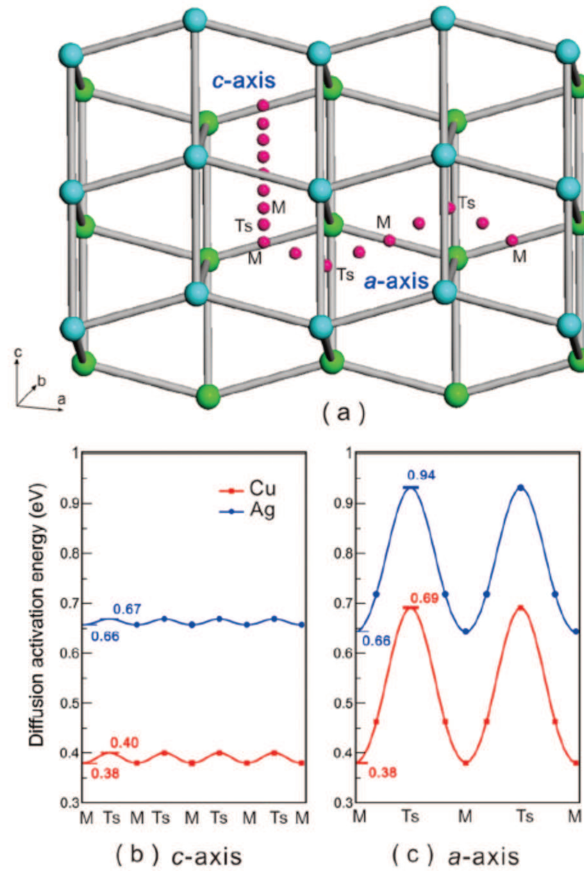

Figure 34: Panel (a) displays the diffusion pathway (the red balls) for interstitial atom jumping along the c-axis and a-axis. The cyan and green balls represent the two different layers of β–Sn. Panels (b) and (c) shows the diffusion energy curves of Cu and Ag along the c-axis and a-axis, respectively. [47]

Reportedly, when a high current density is applied to a solder joint the atoms' drift is much more severe if the bulk lattice has its *c* axis oriented parallel to the direction of the electron flow. In Figure 35 a Sn-0.7 wt.%Cu solder joint presents two grains on each side of the solder, and a EBSD analysis show that the grain in the left has its *c* axis oriented parallel to the direction of the electron flow, whereas the grain in the right has its *c* axis perpendicular to the electron flow. A much larger IMC accumulation near the anode is present in the left side, which means that Cu migrated from the cathode UBM towards the anode. This could lead to weakening of the joint and void formation at the cathode due to Cu depletion. At the right side, less IMC is found near the anode, however a severe depletion is found at the cathode. This is claimed to be due to the Sn self-diffusion, pushed by EM force, and since the Cu had a difficult diffusion pathway it was not able to slow down Sn diffusion, or annihilate the voids. They reported that failure due to depletion of Cu is faster than when Sn is depleted [36].

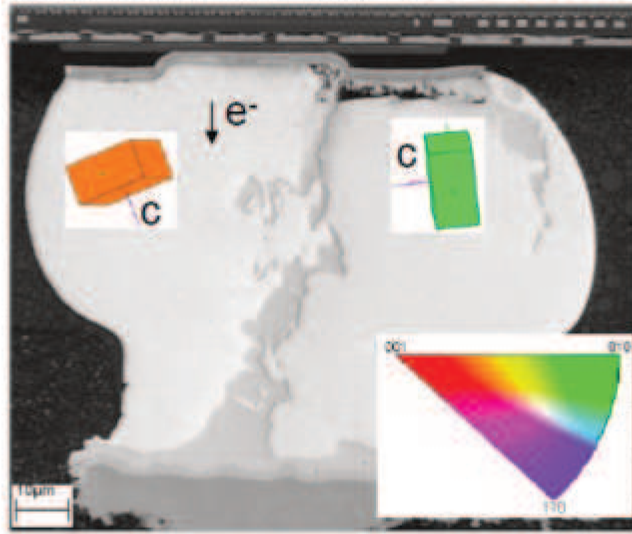

Figure 35: SEM image of a bi-crystal Sn-Cu solder bump. [36]

2.3.5.5. Reliability depending on surface finish and Zn content

Lu et al evaluated the solder reliability through measurement of resistance during EM stress for Sn-1.0 wt.%Ag-x wt.%Zn, where x = 0.2, 0.4 and 0.6. A current density of 5.2e+03 A/cm² was used and the temperature was 150 °C. He found that the addition of Zn at 0.6 wt.% eliminated "early failures" that happened in the solder without Zn at around 500h, and all joints failed after 1000h of EM stressing when the solder joint was mounted on a bare Cu anode and Ni UBM cathode (Figure 36 (a) and (b)). They found that the Zn addition could stabilize significantly the solder microstructure, and form a accumulation layer at the cathode interface which would slow down the dissolution of Cu at the anode, enhancing the life-time [36].

They also inverted the polarity of the electron flow for the Sn-1.0 wt.%Ag-0.6 wt.%Zn solder joint, so that the bare Cu was the cathode. As seen on Figure 36 (c) the average life-time of the solder decreased because the Cu was free to dissolve into the bulk, and when the Ni UBM is present it acts as a physical barrier, since Ni doesn't diffuse as fast as Cu into Sn and other types of IMC are formed at the cathode containing Ni, so that dissolution mechanism differs from when the bare Cu is used as anode.

Also, using Ni UBM on both sides decreased the life time of the solders, in comparison to those using bare Cu as anode. The reason may be due to the backflow of Cu atoms from the anode, due to a backstress and a more easy dissolution of Cu from the bare Cu anode. However it showed somewhat better results than when bare Cu was used as cathode (Figure 36 (d)).

Similar mechanisms were found by Kim et al which evaluated the reliability of Sn-1.2 wt.%Ag-0.7 wt.%Cu-0.4 wt.%In solder using organic solderability preservative (OSP) or ENIG as surface finishes. Using ENIG, there is Ni accumulation near the interface, which acts as barrier to Cu diffusion and improves the life-time of the solder. Figure 37 shows the reliability results plotting the cumulative probability distribution (CDF %) versus the time to failure. The mean time to failure of joint using ENIG was 293.5 hours, and using OSP was 60.7 hours [48].

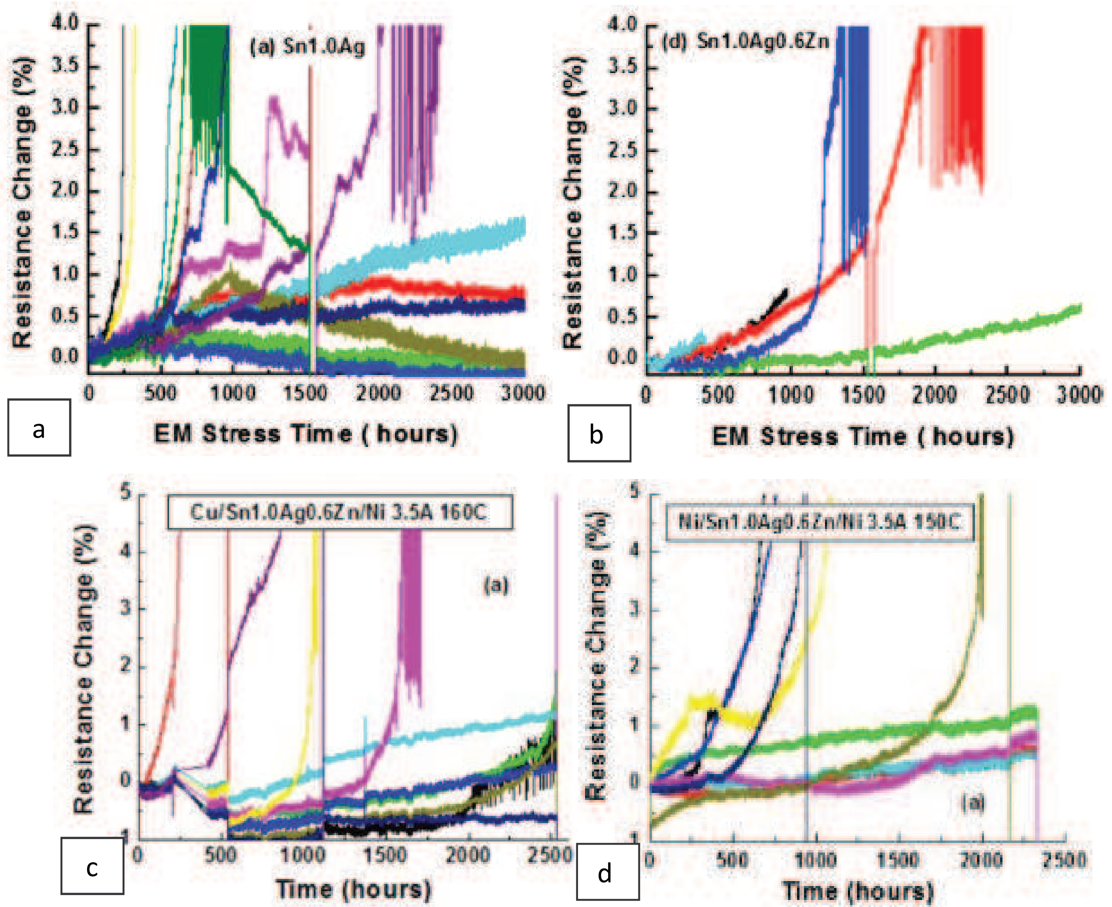

Figure 36: Plot of resistance change versus EM stress time under 5.2e+03 A/cm² current density for (a) Sn-1.0 wt.%Ag and (b) to (d) Sn-1.0 wt.%Ag-0.6 wt.%Zn. Solder using for anode and cathode, respectively in each case: (a) and (b) bare Cu and Ni UBM; (c) Ni UBM and bare Cu; and (d) Ni UBM at both sides. [36]

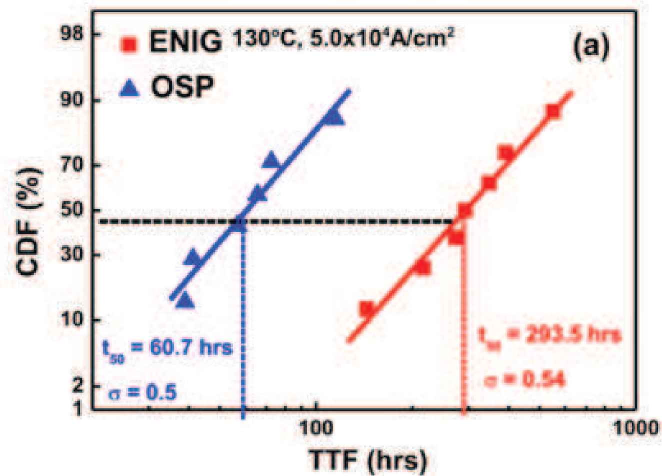

Figure 37: Effects of the surface finish on the EM reliability at 130 °C and 5.0e+04 A/cm², for the Sn-1.2 wt.%Ag-0.7 wt.%Cu-0.4 wt.%In solder. [48]

CHAPTER 3. EXPERIMENTAL PROCEDURES

3.1. Solder alloy and test samples

For this research, 4 solder powders with different Sn, Cu and Zn contents (A, B, C and D) were used to produce solder balls and interconnects. The powders contained type 3 sized metal microspheres – 80% of diameter between 45 and 25 µm, maximum of 10% below 20 µm and no particle above 50 µm. They were mixed with a commercial no-clean flux at a weight ratio of powder to flux of 7.3:1, type RMA (high Mildly Rosin Activated) in a centrifuge with rotation speed and revolution speed both of 300 rpm, which provides uniform mixture and avoids air entrapment.

In order to verify the chemical composition of the alloys, inductively coupled plasma optical emission spectrometry (ICP-OES) was performed with each solder powder and with post-reflow solder balls – the paste was printed onto an inert polyimide tape substrate and reflowed with the same profile used in Figure 42 – 1,4 °C/s ramp up, 260 °C peak temperature, 1 minute above melting temperature and air cooled. The preparation for the ICP-OES test included digesting 2 g of each powder / solder balls with acqua regia solution – HNO_3 + HCl at a ratio of 1:3 – at a temperature of 80 °C. The average composition obtained from 3 tests are shown in the Table 5. Considering the post reflow elemental results, hereinafter the solder alloys containing 0, 0.09, 0.19 and 0.16 Zn will be mentioned as solders A, B, C and D, respectively.

Table 5: ICP-OES analyses of solders A (Sn-Cu), and B, C and D (Sn-Cu-Zn).

ICP OES - Sn-Y wt%Cu-X wt%Zn		Metal Powder				Solder Ball - Post Reflow			
		A	B	C	D	A	B	C	D
Cu (Y)	Average	0,74	0,79	0,78	0,49	0,75	0,90	0,89	0,51
	Std. Dev.	0,03	0,08	0,06	0,03	0,03	0,04	0,02	0,01
Zn (X)	Average	-	0,48	0,86	0,94	-	0,09	0,19	0,16
	Std. Dev.	-	0,02	0,06	0,04	-	0,01	0,01	0,00

It was seen that much of the Zn for all solders was lost. However, Sn was also removed along with the flux during reflow. Although a no-clean flux was used, when Zn was added, some flux residue was left stuck to the solidified metal and surrounding areas on the PCB – this flux could be removed mechanically, which was done for ICP-OES analyses. Energy dispersive X-ray spectrometry (EDS) and EPMA were used to identify which elements were present in the flux and it was observed that it contained Zn and Sn – see Figures 38 and 39. Zn added solders (B, C and D) lost around 83 wt.% of its Zn content, Solder A lost 2 wt.% of Sn, B and C solders lost 12 wt.% of Sn and D lost 3 wt.% of its Sn. EDS was performed on several flux residues left on solders after reflow and EPMA analysis was made on a sample of solder D which was used for an electromigration test for 200h. However, the flux residue remained intact after this test and cross section. It can be seen from Figure 39 that the count for Zn is proportional to the ICP results for solders B, C and D – these images are from solders reflowed on ENIG substrate. Figure 39 shows that flux residue for solder D contains Zn and Sn, and no Cu – this joint was reflowed using OSP substrate.

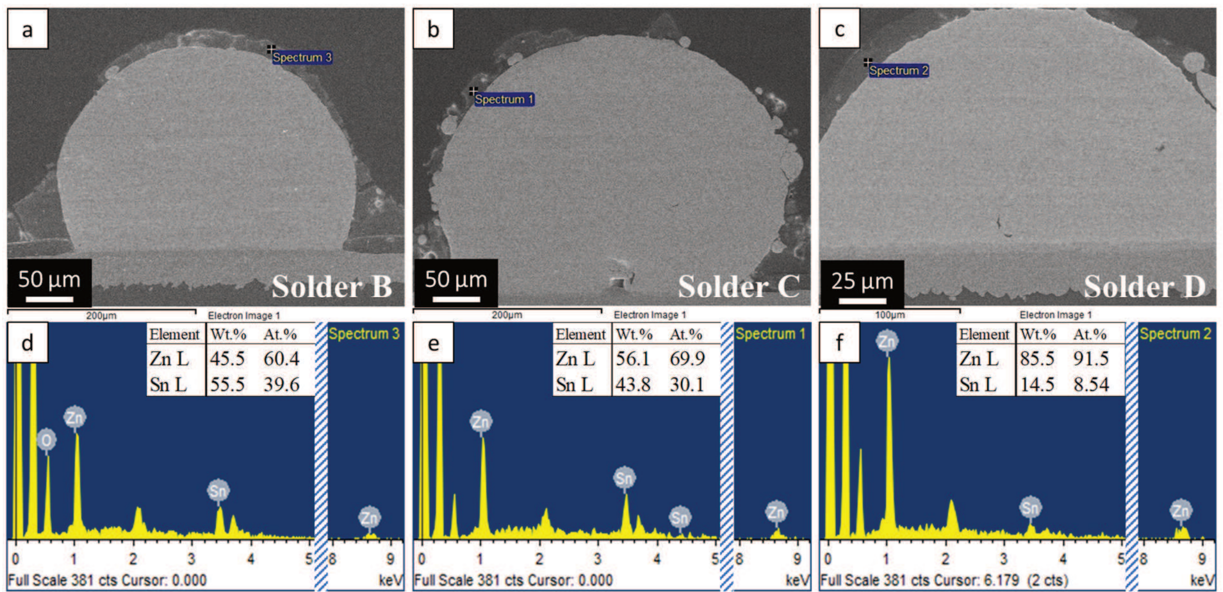

Figure 38: SEM image and EDS point elemental analysis for solders B (a, d), C (b, e) and D (c, f) reflowed on ENIG substrate.

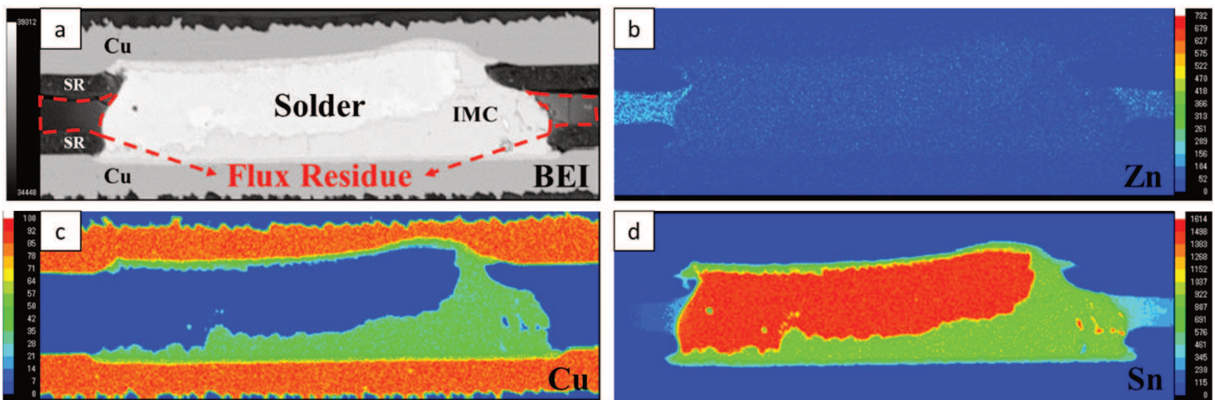

Figure 39: EPMA on flux residue left around solder joint showing backscattered electron image – BEI (a), elemental scan for Zn (b), Cu (c) and Sn (d). Acceleration voltage 15 kV, Beam Size 1 µm, Step 1 x 1 µm. The scale bar on the side of each image represents the element count color label.

Figures 40 (a) illustrates the process for making samples for the aging and electromigration experiments. The solder pastes were mask-printed on 320 µm Cu pads built on a FR-4/solder resist substrate, containing 64 pads. Two types of surface finishes were used – OSP and ENIG. For this research, the ENIG surface finishes had a measured ~ 10 µm Ni-P layer topped by a ~ 3 µm Au layer, and the OSP protective layer thickness could not be determined (scheme on Figure 40 (c)). For electromigration, after the first printing/reflow step, flux was applied to another substrate containing 350 µm Cu pads and the solder ball containing substrate was placed on top it, and this couple was reflowed using the same reflow profile of Figure 41 – this reflow profile was set according to the recommendations of use from the flux manufacturer. The reflow machine used in this research was 1 meter long and the tray speed was 0.3 cm/s. It possesses four zones where a different temperature can be set for each, and heat is spread out by fans at each zone. The curve in Figure 41 is the actual measurement obtained by a thermocouple sensor attached to a substrate during the process of reflow. Before most of reflows, the curve was assessed in order to guarantee that all samples had similar reflowing conditions. It is also illustrated (blue filled rectangle) in Figure 41 the flux activation temperature range, as informed by the flux manufacturer.

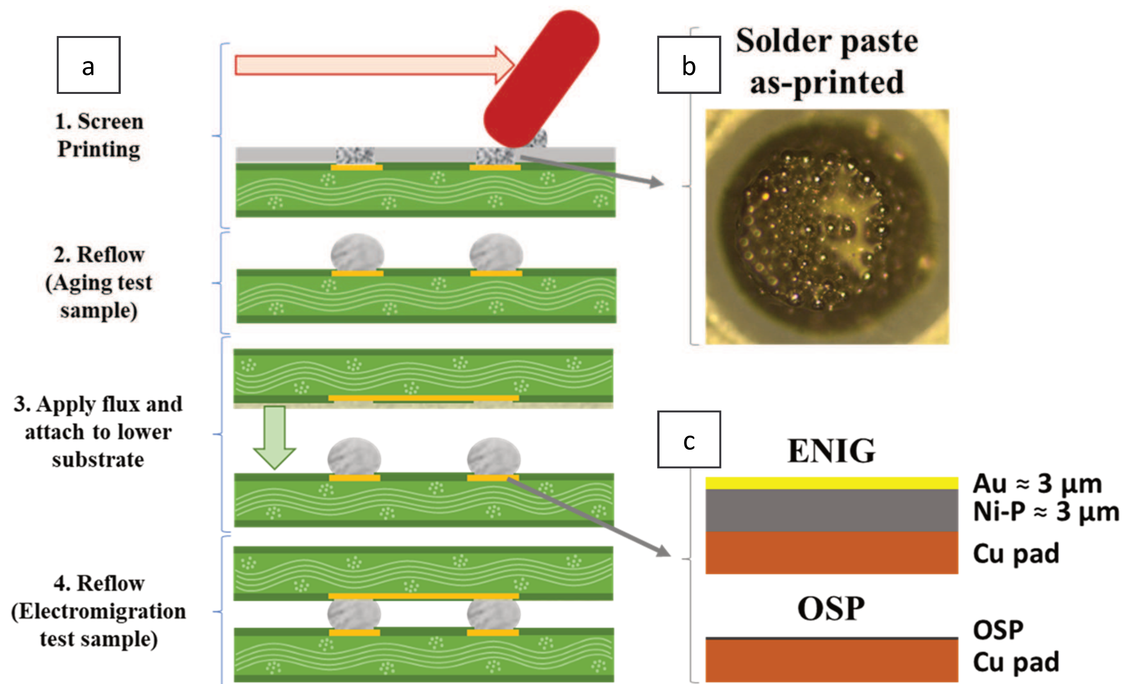

Figure 40: Process of producing samples for this research (a); example of as printed solder paste on a substrate (b); illustration of ENIG and OSP surface finishes (c).

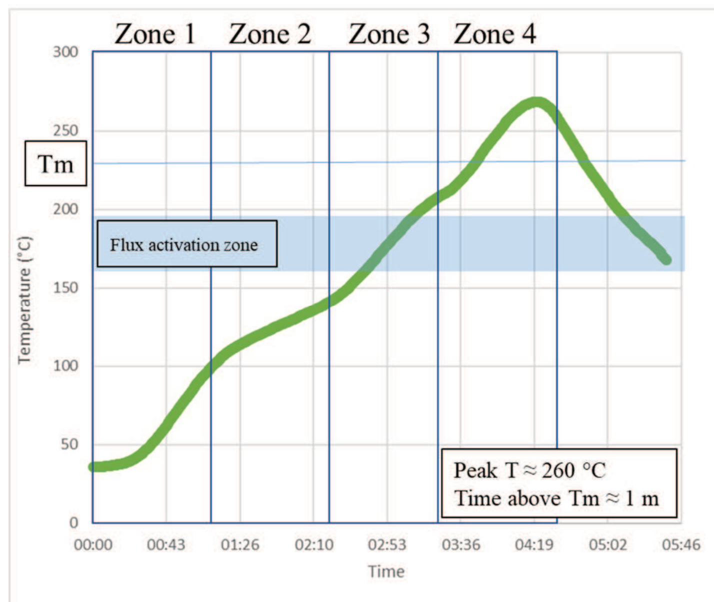

Figure 41: Reflow profile measured by thermocouple sensor. The oven's 4 zones are illustrated superimposed to the curve. Peak temperature was 260 °C, time above melting temperature was around 1 minute. After reflow, samples underwent air-cooling of 1.83 °C/s on average.

3.2. Aging Experiments

For the aging experiments, each solder alloy (A, B, C and D) was printed on substrates, as shown in the previous section, and stored in an oven at constant and high temperatures - 125, 150 or 175 °C – for up to 500 hours, sampling also at 50, 100 and 200 h. OSP and ENIG were used as surface finishes.

After aging, the microstructures of aged and as-reflowed samples were compared. Sample preparation included mounting each sample in an epoxy resin and grinding and polishing down to a 0.05 µm diameter sized SiO_2 polishing colloidal suspension solution. The microstructure was captured with a digital camera coupled to an optical microscope utilizing bright field and cross polarized light illumination. Thus, the intermetallic compounds and grains sizes and distribution could be analyzed. An elemental analysis with SEM/EDS was carried out to confirm some of the phases' chemical compositions.

The aging effects were also evaluated through shear test of same aged samples for each solder alloy. The aging tests were performed according to JEDEC BGA Ball Shear Standard JESD22-B117A. Shear speed used was 600 µm/s and shear height, or tool standoff was 10 µm. Other characteristics are shown in Figure 42 below. The maximum shear force in grams for at least 8 tests was computed and averaged for each sampling condition (solder alloy, aging temperature and time and surface finish). However, whenever a relatively big void affected the results, dropping the shear force, the measurement was excluded, and another solder ball was sheared. Some samples had the fracture surface analyzed by SEM imaging and EDS elemental mapping.

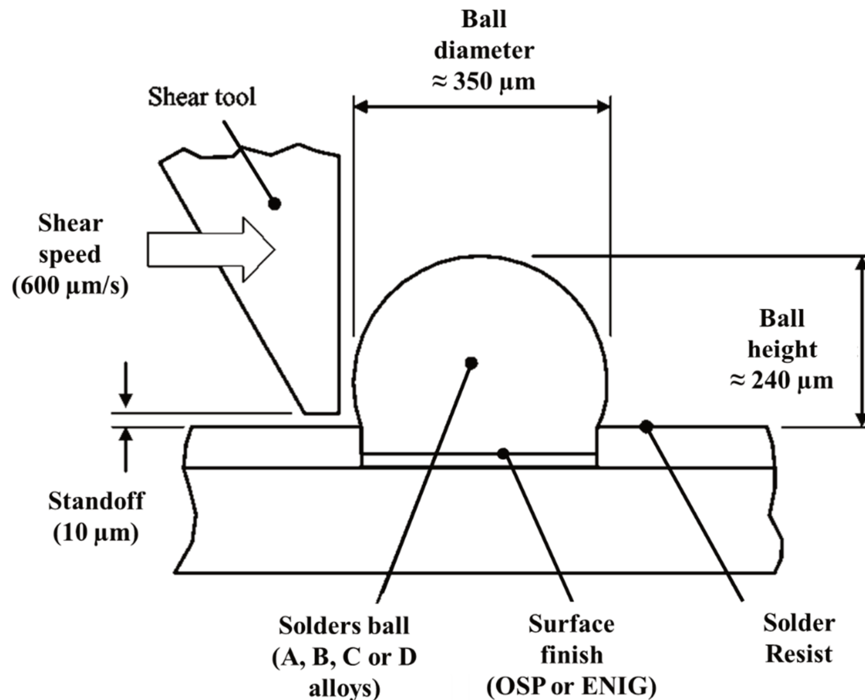

Figure 42: Illustration of shear test scheme and parameters. Shear speed was 600 µm/s and tool standoff was 10 µm.

3.3. Electromigration Experiments

The electromigration experiments followed the JEDEC standard JESD61A.01. It provides a range for each parameter of an electromigration test at solid state. In order to choose adequate parameters for the tests the Joule Heating effect and the thermal coefficient of resistance (TCR) were assessed.

First, the temperature was correlated to the current increase due to the Joule Heating effect – the researches from both Alam (2006) and Lu (2012) include the measurement of the increase in temperature due to increase in the applied current placing sensors on the backside of the

current stressed samples, however they differ in the proportion of increase in temperature – Alam (2006) found that the temperature increase was proportional to the increase in applied current, while Lu (2012) found that the temperature proportion to the square of the current. Several samples were prepared utilizing the same arrangement of the electromigration test samples, however the top substrate, which connects the two solder joints was thinned down to less than 100 µm, and a thermocouple sensor was placed on top of the Cu trail, as illustrated on Figure 43. The samples were then placed inside an oven for maintaining isothermal condition at two different temperatures – room temperature ≈ 25 °C and 125 °C – and current was applied with values ranging from 0.1 A to 3,25 A. The results of temperature variation with current increase were consistent for both oven set temperatures – the slope for both, or sensitivity, had a value of 7.7 °C/A, and it had a linear correlation, as shown in Figure 44. Based on these results, the current and ambient temperature for electromigration tests in this research were chosen to be, respectively, 3.25 A and 125 °C, in order to have a temperature of 150 °C in the solder joints during the experiments – the dashed lines in Figure 44 indicate that 3,25 A generate 25 °C due to Joule Heating –, which is suitable for accelerated electromigration experiments.

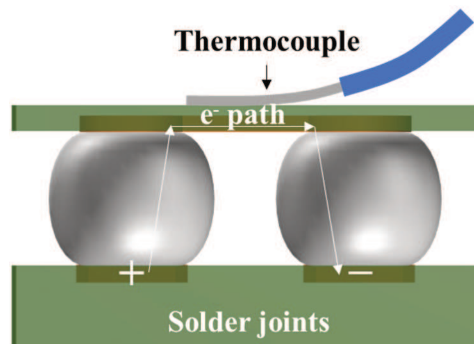

Figure 43: Illustration of method for measuring the joints' temperature while currents ranging from 100 mA to 3.3 A were applied.

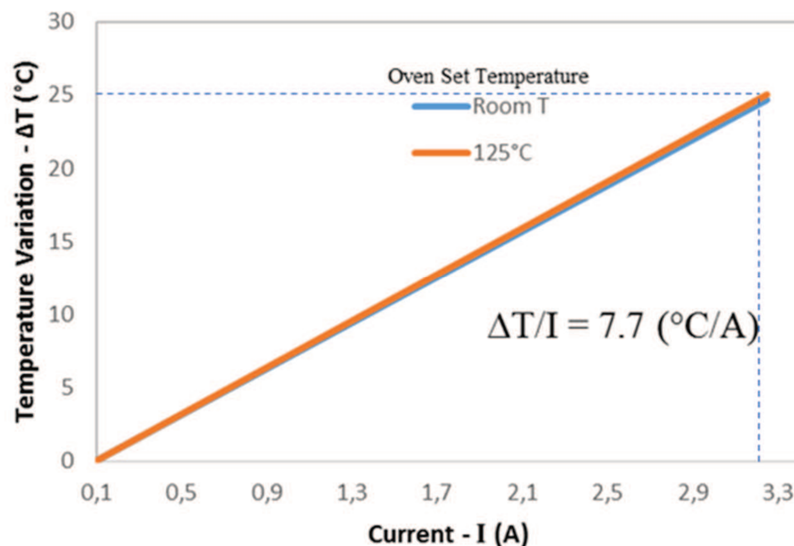

Figure 44: Results from Joule Heating effect experiments. Currents applied ranging from 100 mA to 3,25 A in ambient temperatures of 25 °C and 125 °C. The sensitivity was calculated as 7.7 °C/A.

Afterwards, a TCR assessment was performed, measuring the relation between resistance change and temperature change, according to JEDEC standard JESD33B. Same arrangement from the electromigration test samples was used again, and samples were placed inside an oven

to control the ambient temperature. Two values for current were applied to the joints, 0.1 A and 3.25 A, and the resistance was measured for several oven temperatures: 25, 50, 75, 100, 115, 130, 140 and 150 °C. The results for resistance change with temperature was consistent for both applied currents and the TCR was calculated as 0.00094 $°C^{-1}$, according to the equation (10). Figure 45 shows plot the change variation (%) vs. the oven temperature for these tests. Based on these results, the maximum resistance change before a joint was considered as failed was defined as 8%, considering that this much resistance change leads to an increase of around 75 °C in the solder joints – as indicated by the dashed lines in Figure 45 –, which would lead to partial or full melting of the solder joints, since the temperature in the joints during the electromigration tests was set as 150 °C.

$$TCR(T_0) = \frac{\frac{R(T)}{R(T_0)} - 1}{T - T_0} \tag{10}$$

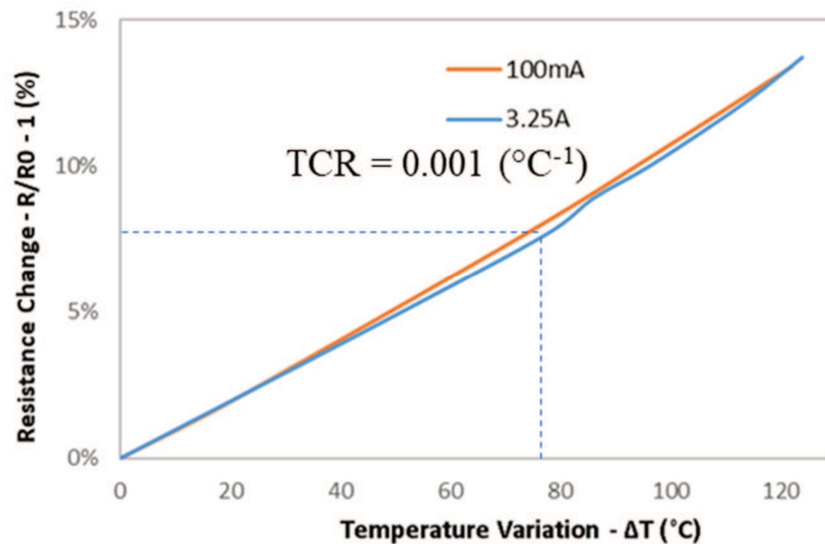

Figure 45: Results from TCR measurement experiments. Ambient temperature had values ranging from 25 °C to 150 °C and currents applied were 100 mA and 3,25 A. The TCR was calculated as 0.001 $°C^{-1}$.

The samples for electromigration were connected with oxygen free Cu wires to a DC current supply, and placed inside an oven, as illustrated in Figure 46 (a). Figure 46 (b) displays and example of a sample used in our experiments and (c) provides an illustration of the solder joints couple. In order to evaluate the microstructure evolution, the length of the experiments was 50, 100 and 200 hours. At least 3 samples using each solder alloy (A, B, C and D) and each surface finish (ENIG and OSP) were tested.

It was identified that after reflow, many solder joints possessed large macrovoids. These macrovoids, if present in an electromigration sample, would reduce the area for current flow, probably increasing current crowding, and would affect the microstructure of the solder, causing a distortion in the experiment results. Therefore, the samples were X-rayed and solders with macrovoids larger than 10% of the total 2D projected solder image area would not be selected for these experiments. Figure 47 shows an example of (a) an X-rayed image of a solder having a macrovoid with area of 20.7% of the total solder area, (b) a cross section of this joint, and (c) a couple in which one joint has a void with area of 7.5% and the other is absent of voids.

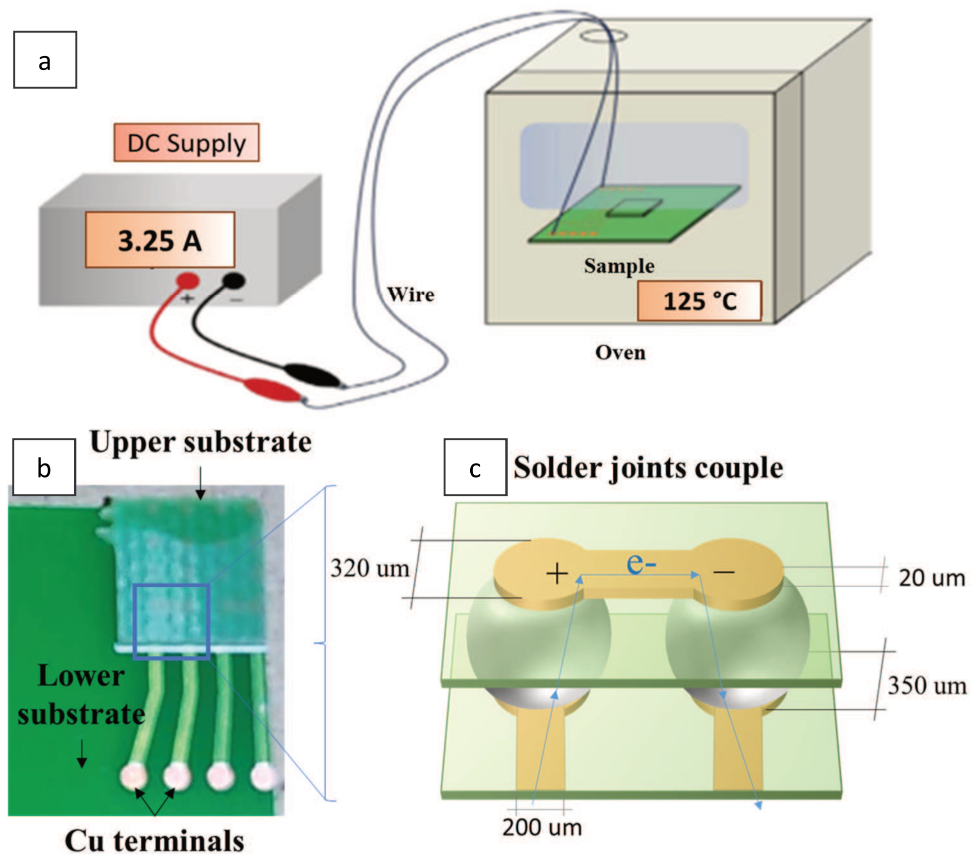

Figure 46: (a) Illustration of experiments set up; (b) example of sample used in the experiments; and (c) illustration of solder joints couple.

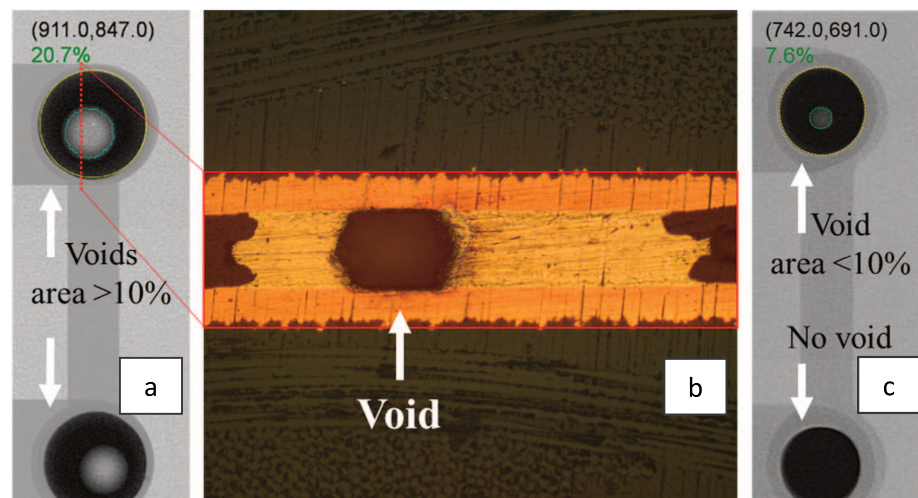

Figure 47: (a) X-ray image of sample with macrovoid with area of 20.7% of the total joint image area; (b) cross section of solder with macrovoid; and (c) X-ray image of sample with void with area of 7.6% of the total joint image area.

After the electromigration experiments, the microstructures of stressed and as-reflowed samples were compared. Sample preparation included mounting each sample in an epoxy resin and grinding and polishing down to a 0.05 μm diameter sized SiO_2 polishing colloidal suspension solution. The microstructure was captured with a digital camera coupled to an optical microscope utilizing bright field and cross polarized light illumination. Thus, the intermetallic compounds and grains sizes and distribution could be analyzed. Imaging and

elemental analysis with SEM/EDS with was carried out to confirm some of the microstructures and phases' chemical compositions. The preparation for SEM/EDS analyses included applying a Pt sputtered coating, and some samples were etched to better reveal the microstructure with a solution of 92 vol.% CH_3OH, 5 vol.% HNO_3 and 3% HCl. Also, EPMA was performed in some of the interfaces in order to identify the elemental distribution at the interfaces. The β-Sn grain orientations were identified using EBSD method for the majority of samples, since it affects greatly the diffusion of alloying elements through its crystal lattice during electromigration tests. The EBSD analyses might be affected if a sputtered coating is applied (as usual when using SEM) –, however the epoxy mount and PCB cause interference to the electron beams, since they are insulant materials and accumulate charges on their surfaces. Therefore, a conductive carbon-based paste was applied to the surroundings of the joints in order to eliminate accumulation of charges in the surface of the sample and improve the accuracy of the electron beams. Figure 48 has an example of a sample prepared for EBSD analysis.

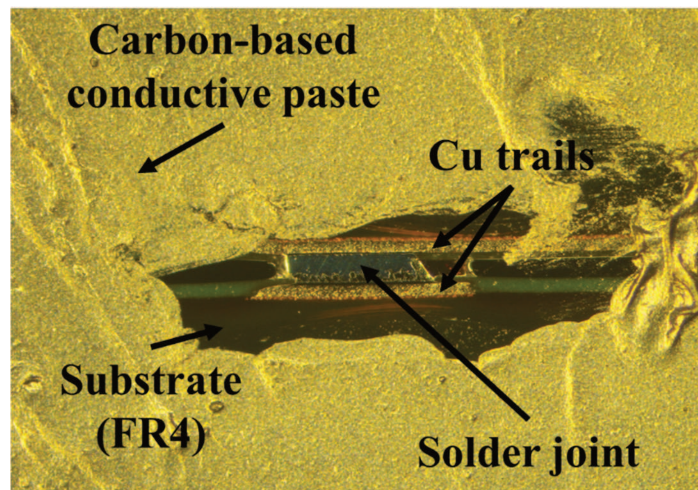

Figure 48: Example of sample prepared for EBSD analysis, where a conductive paste was applied on the surroundings of the joints in order to eliminate charge accumulation on the surface of the non-conductive materials (FR-4 substrate and epoxy mount).

CHAPTER 4. EXPERIMENTAL RESULTS AND DISCUSSION

4.1. Microstructure as reflowed

4.1.1. Interfacial IMC

The compounds formed were analyzed in the SEM by EDS. The samples were reflowed and cross sectioned, and the etching solution mentioned previously was applied to reveal the microstructures. Figures 49 and 50 show the analysis at the interface between solder and Cu pad, including SEM image, identification of the phases and localized EDS elemental analysis showing the obtained spectrum of counts vs. diffraction energy in keV. Figure 51 shows the average size for the interfacial IMC total thickness at the as reflowed condition for each solder and both surface finishes.

All samples with OSP surface finish formed Cu_6Sn_5 IMC, considering the atomic ratio obtained in the EDS analyses, which varied for Cu from 56 to 68 at.%, and Sn as the composition remaining. For the Sn-Cu solder (solder A), the IMC had a planar shape and measured around 3 µm. The addition of Zn turned the interfacial IMC's shape into a more scalloped morphology, and the thickness decreased to, in average, 1,3 µm in average with the addition of 0,19 Zn (solder C). The samples with ENIG surface finish formed two types of IMC at the interface. For the Sn-Cu solder (A), on top of the Ni-P layer, an IMC which is believed to be a modification of the Ni_3Sn_4 IMC - $(Ni,Cu,Au)_3Sn_4$ - was formed, containing on average approximately 30 at.% Ni, 15 at.% Cu, 0,6 at.% Cu and 54,4 at.% Sn, and above it, a needle-shaped quaternary IMC compound formed, containing approximately 73.3 at.% Sn, 12 at.% Au, 9 at.% Ni and 6 at.% Cu. This IMC compound ratio does not match any of the Ni-Sn alloy system IMCs, but matches that of the $AuSn_3$ IMC, so, it was identified here as $(Au,Ni,Cu)Sn_3$. The addition of 0.09 and 0.16 wt.% Zn (solders B and D) reduced significantly the total IMC thickness and the growth of $(Au,Ni,Cu)Sn_3$ crystals, and with the addition of 0.19 wt.% Zn these crystals were analyzed by EDS but no Au was identified in it (see Figure 50 (e), (f) and (g)). The presence of Au into the modified Ni_3Sn_4 was practically eliminated when 0.16 wt.% Zn was added (solder D), and was not detected in the solder C (0.19 wt.% Zn) by EDS.

Figure 51 shows the measurements for the total thickness of the interfacial IMC. Overall, the solders with OSP had a larger IMC thickness, and the more Zn added to the alloys the smaller the IMC.

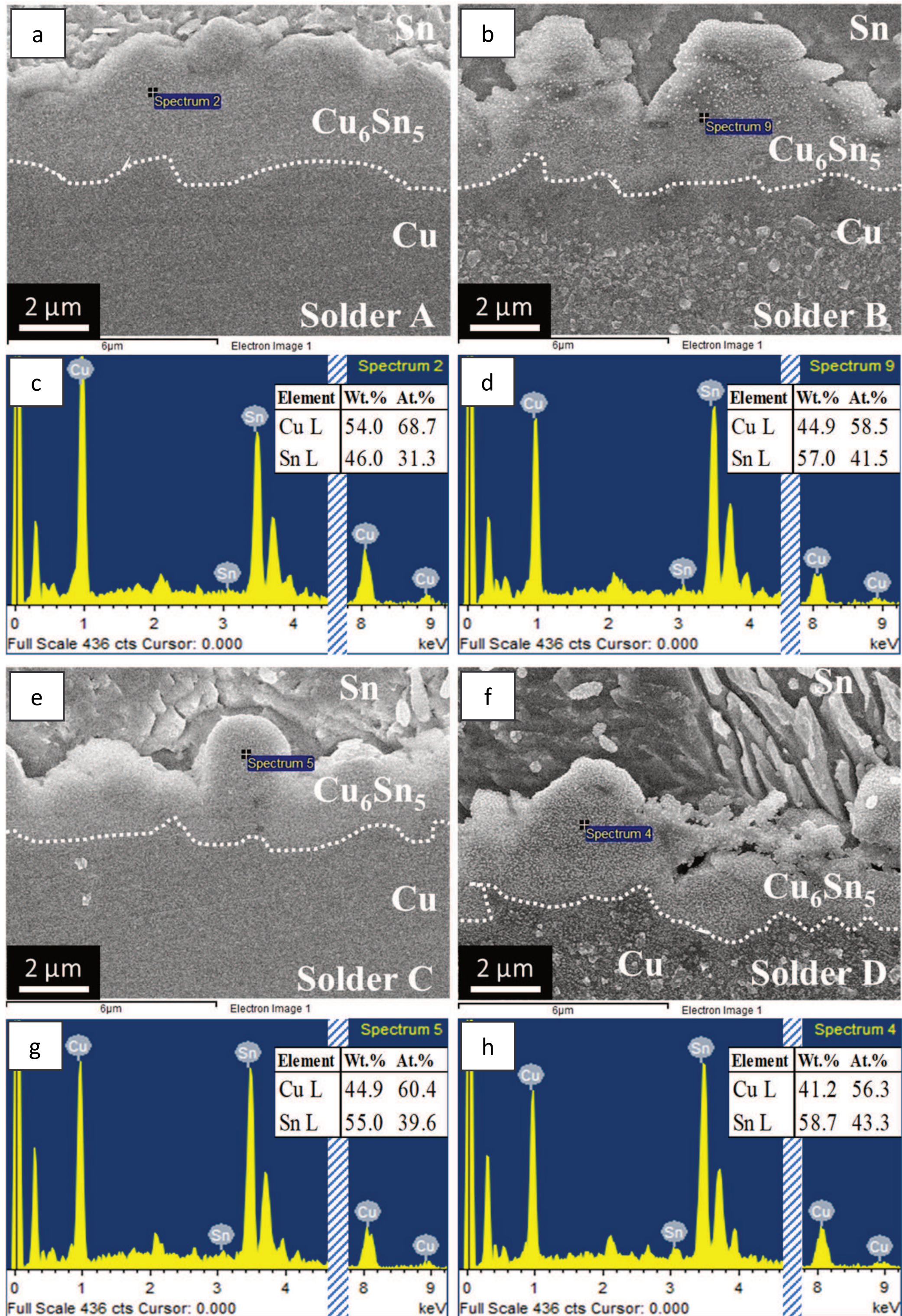

Figure 49: SEM images and EDS elemental analysis results in spectrum of counts vs. diffraction energy and summary table of elements, respectively, for the solder A (a) and (c), B (b) and (d), C (e) and (f) and D (g) and (h).

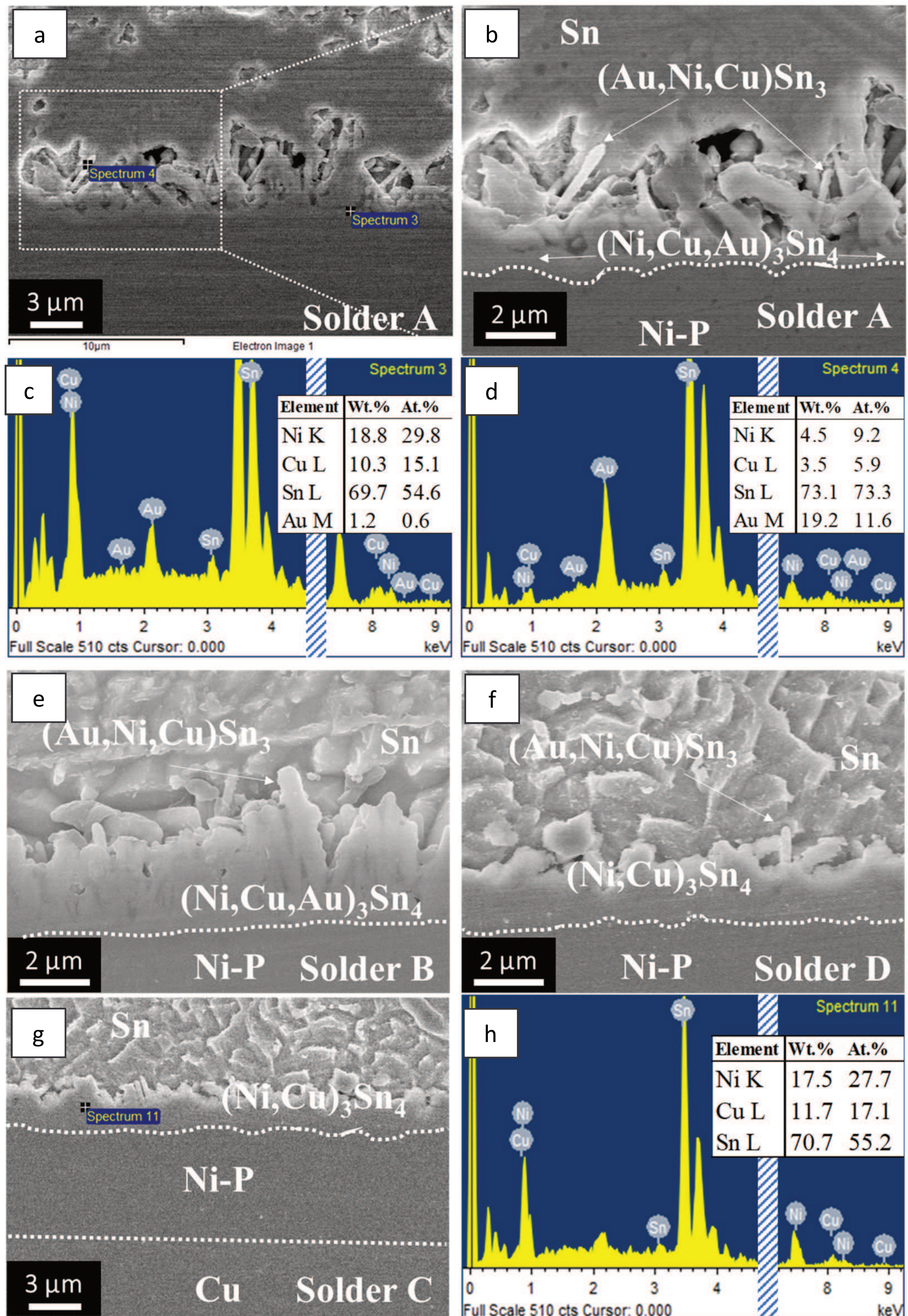

Figure 50: SEM images for solders A (a) and (b), B (e), D (f) and C (g) and EDS elemental analysis results in spectrum of counts vs. diffraction energy and summary table of elements, for solder A (c) and (d), and C (h).

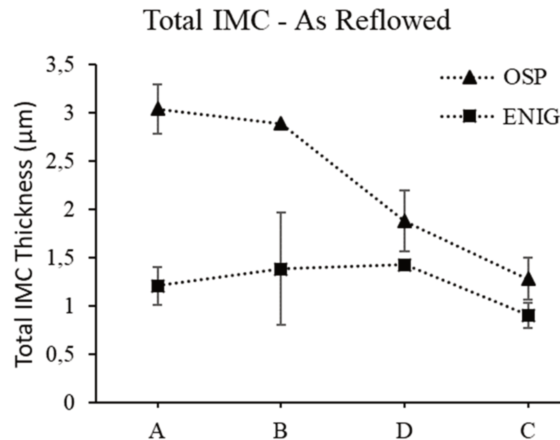

Figure 51: Total IMC thickness measurement for solders A, B, C and D with OSP and ENIG surface finishes after reflow of 1 minute above melting temperature.

An EPMA line scan analysis was conducted to identify the elemental distribution along the interfaces between the bulk solder and Cu pad regions of the Zn containing solders. Figure 52 and 53 shows the results for solder B, solder D and solder C using ENIG surface finish in Figures 52 (a), (b) and (c), respectively, and using OSP surface finish in Figures 53 (a), (b) and (c), respectively. The charts display the percentage of the maximum count for each element, which is shown at the side of each chart, versus the distance in millimeters. The dashed lines identify the probable different phases in each interface and are identified right on top of each chart.

Using ENIG surface finish, for solder B (Figure 52 (a)), it was identified 2 distinct IMC phases. The IMC 1 region contains mostly Sn, some peaks of Au and a considerable amount of Cu and Ni and it is placed right after the IMC 2 region, which contains mostly Sn, Ni and Cu, and some amount of Au. When matching this results to the EDS analysis on solder B interface, it can be said that IMC 1 is the $(Au,Ni,Cu)Sn_3$, which grows in the form of needle-shaped cristals (see Figure 51 (a)), and the IMC 2 is probably $(Ni,Cu,Au)_3Sn_4$. The element Zn is spread out through the solder bulk, IMC phases and substrate (Ni-P and Cu), in less amounts in the latter. Solder D (Figure 52 (b)), presented a region with a peak of gold between two high Sn content regions which are believed to be the solder matrix, which was identified as IMC 3. This region has a slight increase of Zn content and no significant amounts of Ni or Cu. Probably this IMC phase is $AuSn_4$ rather than the modified $AuSn_3$, since in analysis of IMCs in the bulk it was the only Au-Sn IMC found, considering the atomic percentages, as figure 54. The IMC 4 region is probably the $(Ni,Cu,Au)_3Sn_4$ IMC, given the counts of Sn, Ni and Cu elements. It is thinner than the IMC 2 in solder B, which agrees with the SEM and EDS results, however a peak of Zn was found, which was not identified in the EDS analyses. Solder C (Figure 52 (c)), which contains the highest Zn amount between the 4 solders of this study, 0.19 wt.%, shows in the IMC 5 region an IMC that is probably $AuSn_4$ in the bulk, and the IMC 6 region can be $(Ni,Cu,Au)_3Sn_4$. The amount of Au in IMC 6 region is, nevertheless, smaller than in the IMCs next to the Ni-P region in the other solders, which mostly agrees with the previous SEM and EDS results. The amount of Zn is smaller than the IMC 4 in solder D, which is a solder with less amount of Zn added, meaning that the Zn does not accumulate uniformly in this type of IMC.

Using OSP surface finish, all solders had an IMC region between the bulk and substrate containing an IMC that is propably Cu_6Sn_5, considering its elemental counts, agreeing with

SEM and EDS results, however it shows that there is an accumulation of Zn in this IMC, previously not detected, proportional to the initial amount of Zn in the solder – the solders with 0.09, 0.16 and 0.19 wt. % Zn showed in the IMC region a Zn absolute count of, respectively, 221, 275 and 313.

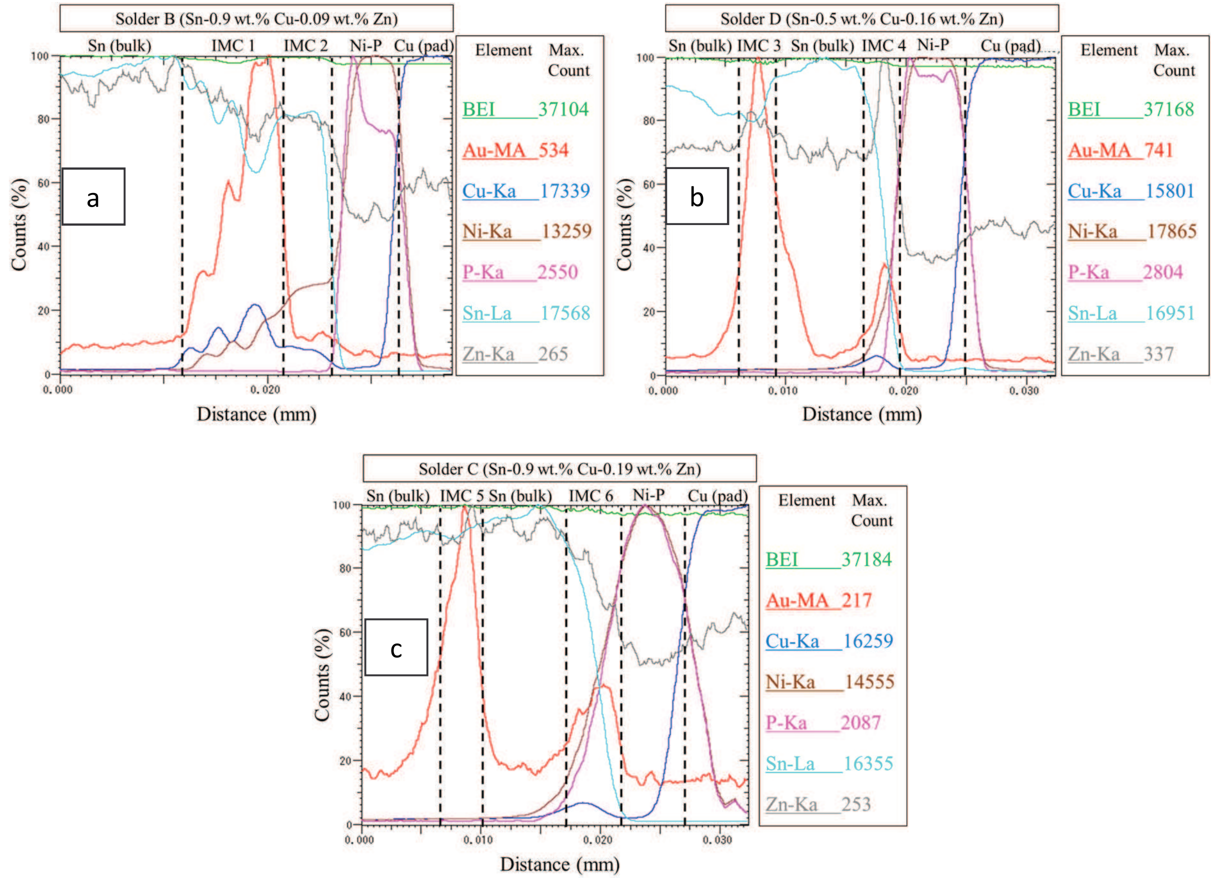

Figure 52: EPMA line scan in the region between the solder bulk and substrate using ENIG surface finish for solders B (a), D (b) and C (c).

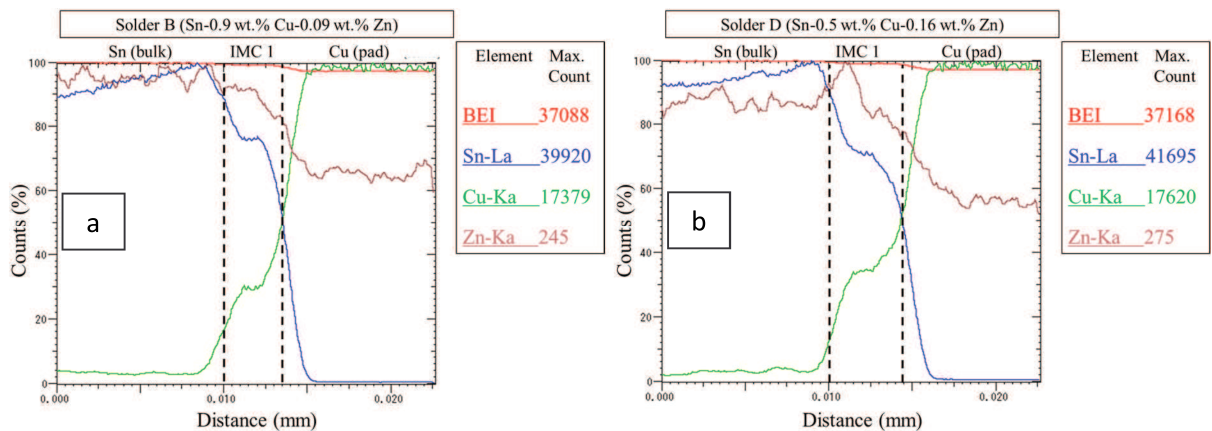

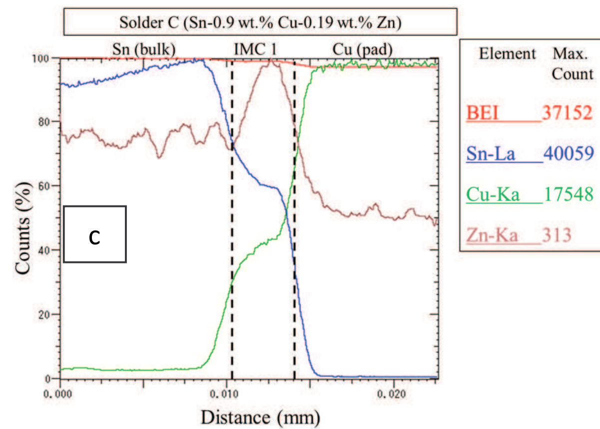

Figure 53: EPMA line scan in the region between the solder bulk and substrate using OSP surface finish for solders B (a), D (b) and C (c).

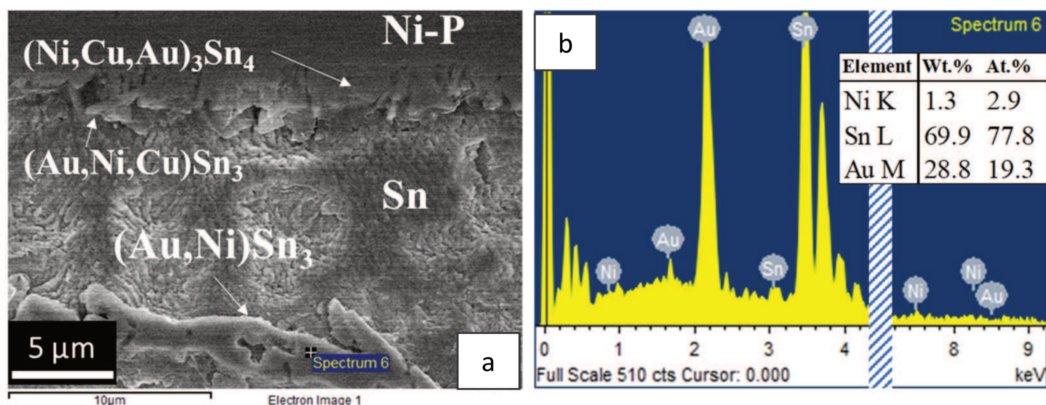

Element	Wt.%	At.%
Ni K	1.3	2.9
Sn L	69.9	77.8
Au M	28.8	19.3

Figure 54: SEM image of etched cross section of solder D (a) and EDS elemental analysis' spectrum and summary table made on a bulk IMC near the interface.

4.1.2. Bulk IMC and grain size distribution

The bulk IMC was analyzed by cross sectioning solders and obtaining an image with an optical microscope using the bright field light (Figures 55 and 56), and the grain size was analyzed by obtaining the images of the same samples using cross polarized light (Figures 57 and 58). The grain size of at least 4 samples of same conditions was further measured using a software for image analysis, and the results were plotted in the form of a boxplot (Figure 59).

In Figures 55 (a), (b), (c), and (d), the cross section of samples of, respectively, solder A, B, C and D in the as reflowed condition using OSP surface finish is shown. As analyzed by EDS, all bulk IMC in these solders are Cu_6Sn_5. The distribution of IMC in all cases is similar close to an eutectic distribution. The solder matrix appears with a grey color, and the IMC is darker and has dark contours. It is possible to see for solder A regions with β-Sn dendrites and IMC dispersed in the inter-dendritic space. Some large Cu_6Sn_5 appear in the solder matrix. Solder B showed the largest eutectic colonies, with fine IMC dispersion, which can be due the Cu content being near the Cu-Sn eutectic – 0.9 wt.%, and the Zn content being low – 0.09 wt.% Zn. Solder C has larger β-Sn than solder B but a considerable number of eutectic colonies. It has same Cu content, however larger Zn content, so it behaves as an alloy of the ternary Cu-Zn-Sn system and requires more Zn for reaching the eutectic point. Solder D has larger primary IMC and it is not dispersed in eutectic-like colonies. Analogously to solder C, this may be due the lower Cu content – 0.05 wt.% and intermediate amount of Zn – 0.16 wt.%.

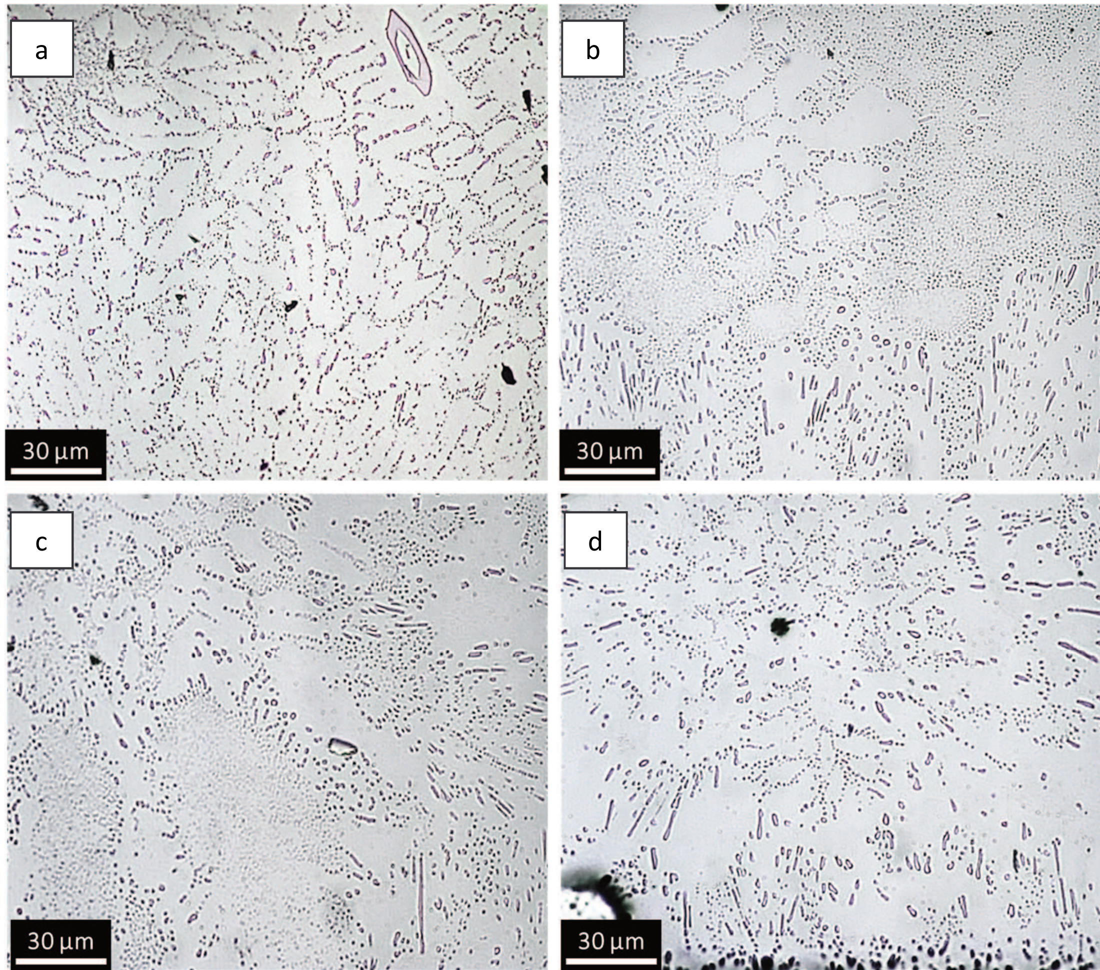

Figure 55: Cross section image obtained by optical microscope with bright field light showing the distribution of the IMCs in solders A (a), B (b), C (c) and D (d), in an as reflowed condition using OSP surface finish.

In Figures 56 (a), (b), (c), and (d), the cross section of samples of, respectively, solder A, B, C and D in the as reflowed condition using ENIG surface finish is shown. The IMC compositions were determined by EDS and they were mostly $AuSn_3$, also having some smaller Cu_6Sn_5. Solder A has a finely dispersed IMC, but not as quite fine as in eutectic colonies. The zinc-added solders had their IMC larger and more located on grain boundaries with larger β-Sn regions, although solder C presented small eutectic areas. This may be due to the quinary solder system Sn-Cu-Zn-Au-Ni is achieved after the dissolution of the elements that composed the substrate into the solder matrix, which places the system's eutectic point further away.

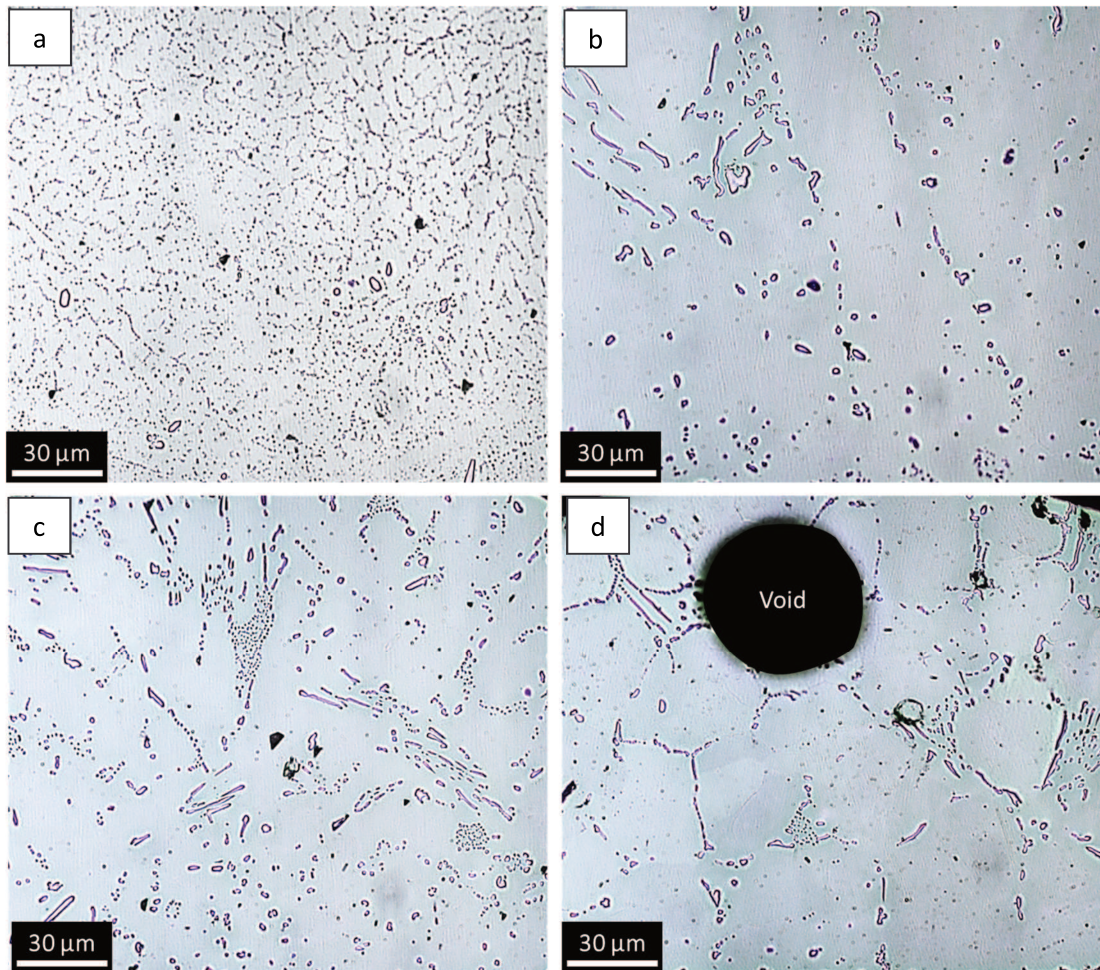

Figure 56: Cross section image obtained by optical microscope with bright field light showing the distribution of the IMCs in solders A (a), B (b), C (c) and D (d), in an as reflowed condition using ENIG surface finish.

Figures 57 and 58 show the cross polarized image of the cross sections of solders A, B, C and D in an as reflowed using, respectively, OSP and ENIG surface finishes. It is possible to see that in most samples there are 3 color tones, which means probably that the grains are cyclic twins. The samples in Figure 57 are the same shown in Figure 55, and the ones in Figure 58 are the same as those in Figure 56. Through this method, different grains that have little misorientation appear with very similar color tone, and it would be more suitable to perform an EBSD analysis to precisely identify the grains, however, due to the nature of solidification of high Sn solders which usually precipitate as twin grains, it is possible to analyze and compare the different alloying conditions.

In Figure 57 (a), solder A shows a grain structure mixed between fully twinned and interlaced. Many interlaced grains are also found in solder D (Figure 57 (d)). Solder B (Figure 57 (b)) presents fewer interlaced grains and solder C has quite large grains (Figure 57 (c). It is possible that the increase in the grain size is caused by the reduction in undercooling with the addition of Zn.

The grains size and shape using the ENIG surface finish had a similar trend as compared with the usage of OSP, however there was more middle-sized grains, solders A and D presented more equiaxied grains and solders B and C presented a more interlaced structure. This may be due to the presence of more alloying elements in the solder (Au and Ni), which diffuse into the matrix during reflow, combined with the high affinity of Zn for noble elements, which are also

highly reactive, and end up decreasing the available Zn content in the molten solder, causing the undercooling to increase.

Figure 59 provides the plot of all grain sizes measured for each solder and surface finish at the as-reflowed condition. It is shown in the form of boxplots, so that the distribution of sizes is evident, and the y-axis is in a logarithmic scale, since there is a large range of grain area within the same samples. In this chart, the upper and lower dashes are the maximum and minimum values, the upper and lower edges of the box are the 75% and 25% markers, and the black lozenge is the median value, or 50% marker. The averaged grain size value is marked with a x.

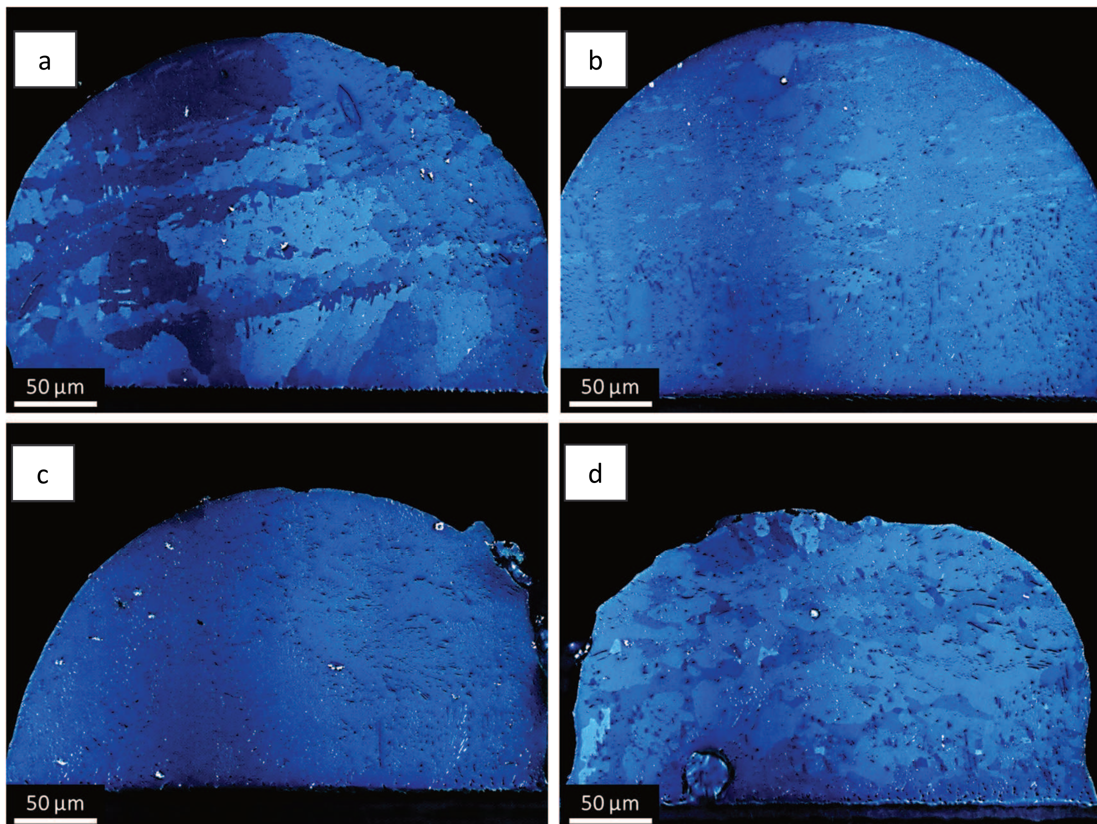

Figure 57: Cross section image obtained by optical microscope with cross polarized light showing the grain morphology in solders A (a), B (b), C (c) and D (d), in an as reflowed condition using OSP surface finish.

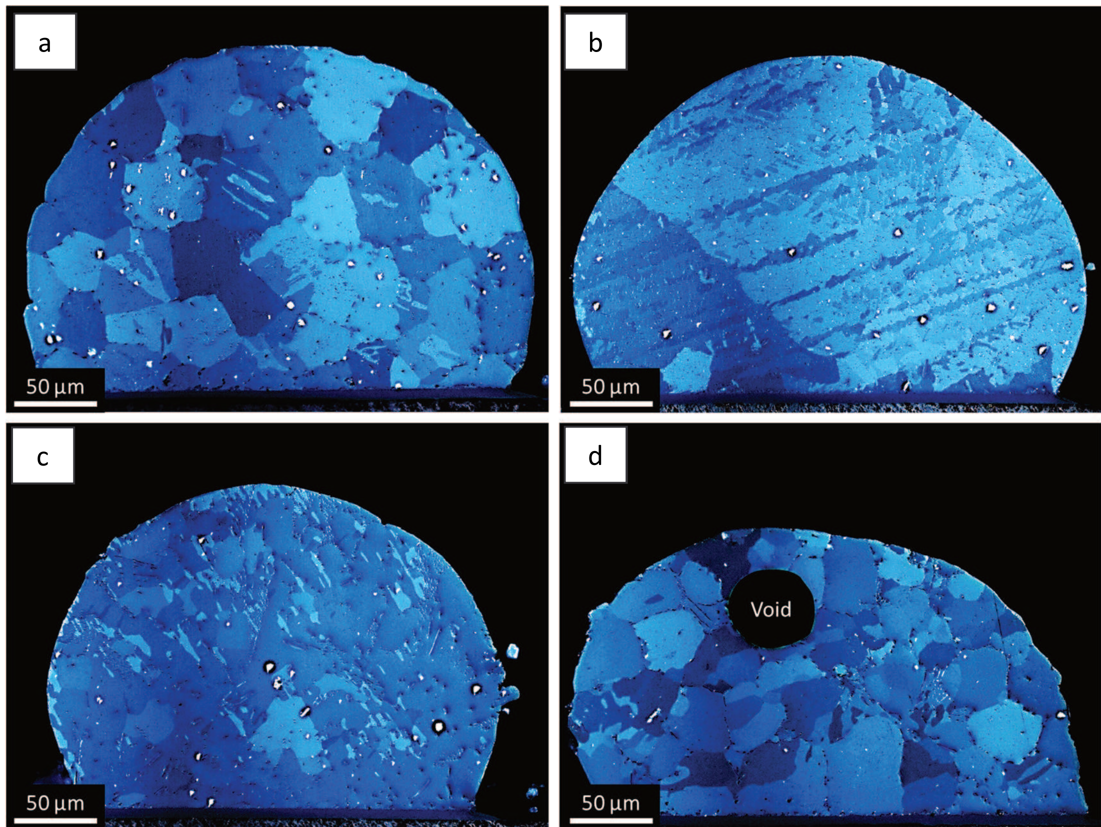

Figure 58: Cross section image obtained by optical microscope with cross polarized light showing the grain morphology in solders A (a), B (b), C (c) and D (d), in an as-reflowed condition using ENIG surface finish.

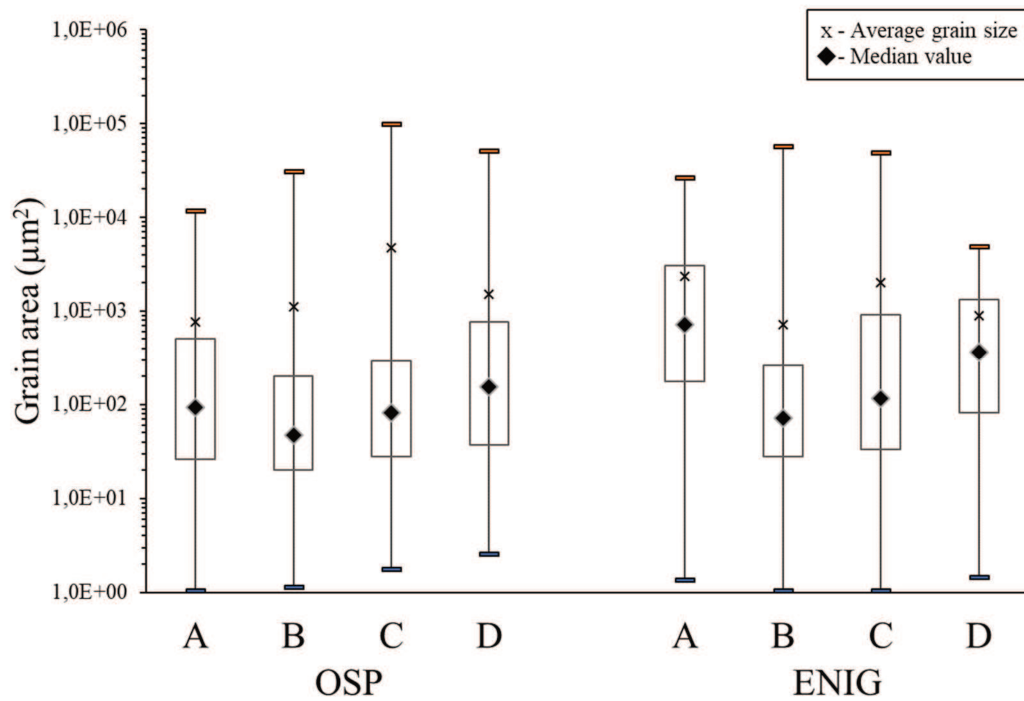

Figure 59: Boxplot chart of grains sizes for solders A, B, C and D and OSP and ENIG surface finishes using a logarithmic scale.

4.2. Microstructure evolution upon aging

4.2.1. Interfacial IMC

Upon aging, the samples using OSP surface finish grew with a planar shaped IMC at the interface. Figure 60 shows the bright field image of the cross section of samples aged at constant temperature of 175 °C and for 500 h. Solder A and B (Figures 60 (a) and (b)), which had no Zn and 0.09 wt.% Zn respectively, had an IMC 11 µm thick, while solders C and D (Figures 60 (c) and (d)) had a smaller IMC, around 8 µm thick. There are 2 phases of IMC, and, as confirmed by EDS analysis, the light color IMC phase is Cu_6Sn_5 and the darker is Cu_3Sn. The addition of Zn reduced the growth of the Cu_3Sn IMC significantly with 0.16 wt. Zn (solder D) and virtually no Cu_3Sn was found when 0.19 wt.% Zn solder was used.

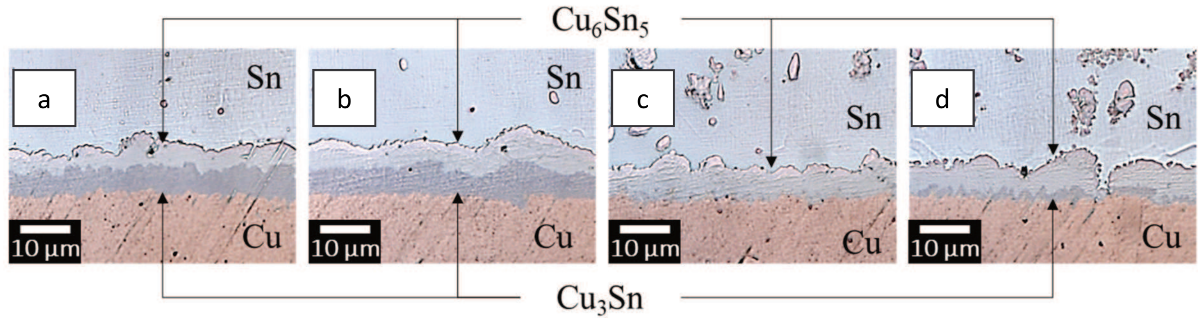

Figure 60: Bright field image of the interfacial IMCs of samples aged isothermally at 175 °C for 500 h, for solders A (a), B (b), C (c) and D (d) using OSP surface finish. The Cu_6Sn_5 IMC appear as a brighter phase on top of a darker Cu_3Sn IMC.

The aged samples were cross sectioned, and the total thickness of the IMC was measured for all solders and conditions. The growth model can be represented by the equation below:

$$W = (kt)^n \tag{11}$$

W is the IMC thickness, *k* is the growth constant, *t* is the aging time and *n* is the time exponent. Yoon et al. (2003) determined empirically that the growth model for these interfacial IMCs is diffusion-controlled, and the time exponent *n* takes the value of 0.5. Therefore, the IMC thickness can be plotted versus the square root of the aging time.

Below, there are the plots of Total IMC thickness (Figure 61) and Cu_3Sn IMC thickness (Figure 62), measured in µm versus the square root of the aging time, which was performed until 500 h. The slope increases with the temperature, meaning that the growth rate increases. The curve fits to the experimental results, meaning that the diffusion is indeed diffusion-controlled.

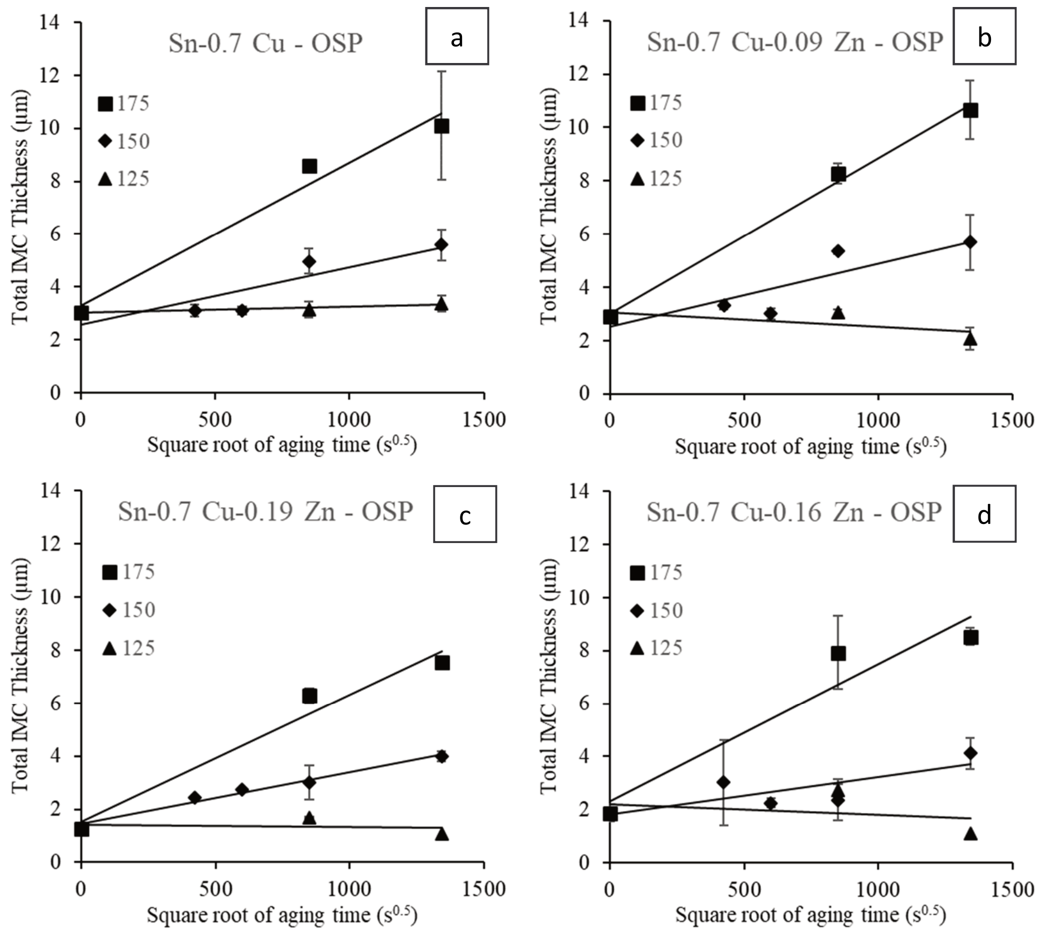

Figure 61: Total IMC thickness versus the square root of the aging time, at 125, 150 and 175 °C, for solders A (a), B (b), C (c) and D (d) using OSP surface finish.

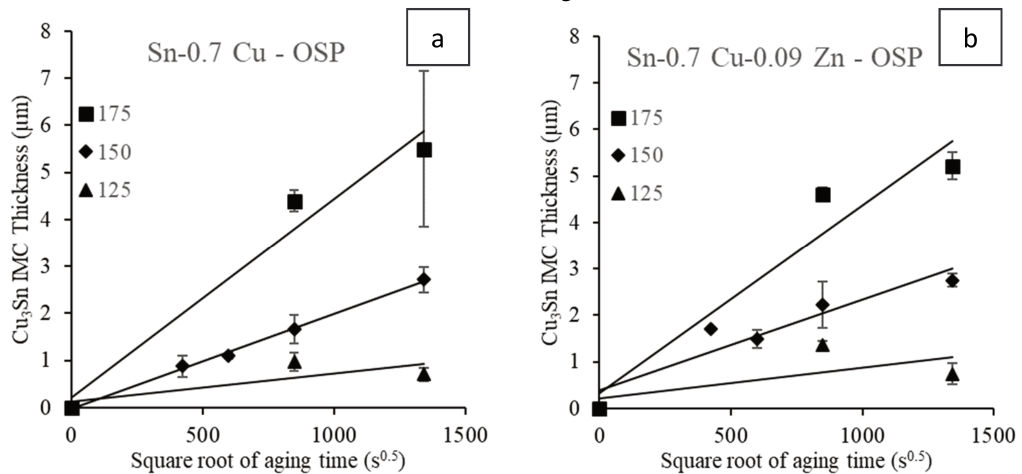

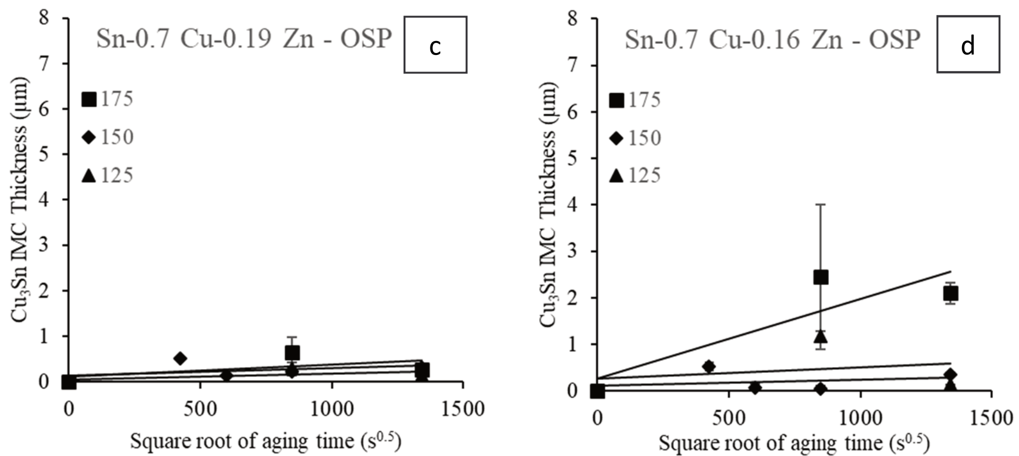

Figure 62: Cu3Sn IMC thickness versus the square root of the aging time, at 125, 150 and 175 °C, for solders A (a), B (b), C (c) and D (d) using OSP surface finish.

Figure 63 summarizes the total IMC thickness and Cu_3Sn IMC for each solder and aging temperature, for 500 h of aging. The higher the aging temperature, the thicker the IMCs formed, and it is evident that the addition of Zn suppresses the growth of Cu_3Sn.

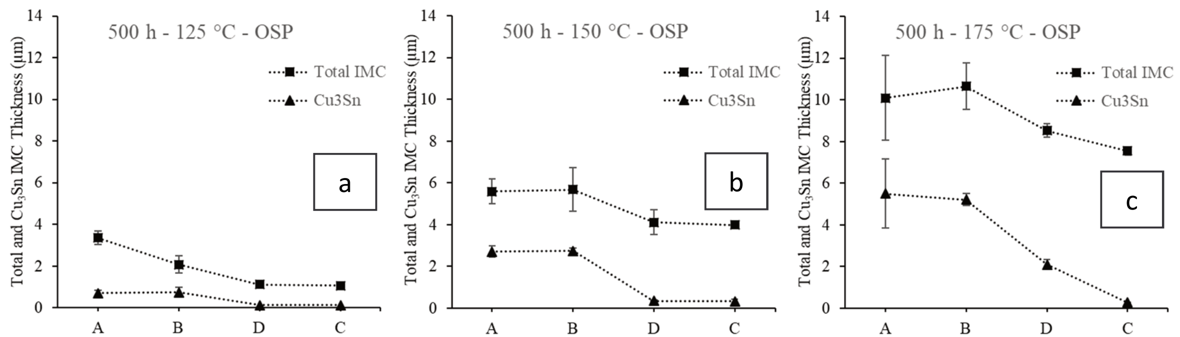

Figure 63: Comparison between each solder's total IMC and Cu3Sn IMC thickness after 500 h of isothermal aging at 125 °C (a), 150 °C (b) and 175 °C (c).

The samples using ENIG had a smaller growth of the interfacial IMC upon aging and the addition of Zn suppressed slightly its growth. Figure 64 shows the cross section of samples that used ENIG surface finishes and underwent isothermal aging at 175 °C for 500 h for solders A (a), B (b), C (c) and D (d). No solder showed the crystal modified $AuSn_3$ IMC, as it was seen in the as-reflowed condition. The morphology was planar, and the phases identified through EDS elemental analysis were Ni_3Sn_4 and $AuSn_4$.

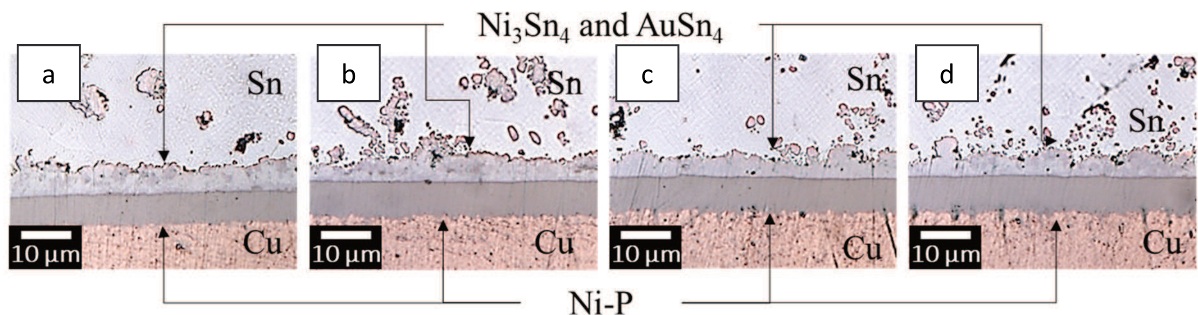

Figure 64: Bright field image of the interfacial IMCs of samples aged isothermally at 175 °C for 500 h, for solders A (a), B (b), C (c) and D (d) using ENIG surface finish. The Ni_3Sn_4 and AuSn4 IMCs appear as a brighter phase on top of a darker Cu_3Sn IMC.

The ENIG surface finished samples had an overall IMC size much smaller than samples with OSP surface finish, even after 500 h of aging. The addition of Zn suppressed the growth of the interfacial IMC, since after 500 h of aging at 175 °C solder A, which has no Zn added, show an IMC of on average 6,5 µm, and solder C had an IMC of around 4,5 µm. Figure 65 show the results of the interfacial IMC thickness evolution for each solder alloy and aging condition. Figure 66 shows a comparison between each solder's total IMC thickness after 500 h of isothermal aging at 125, 150 and 175 °C.

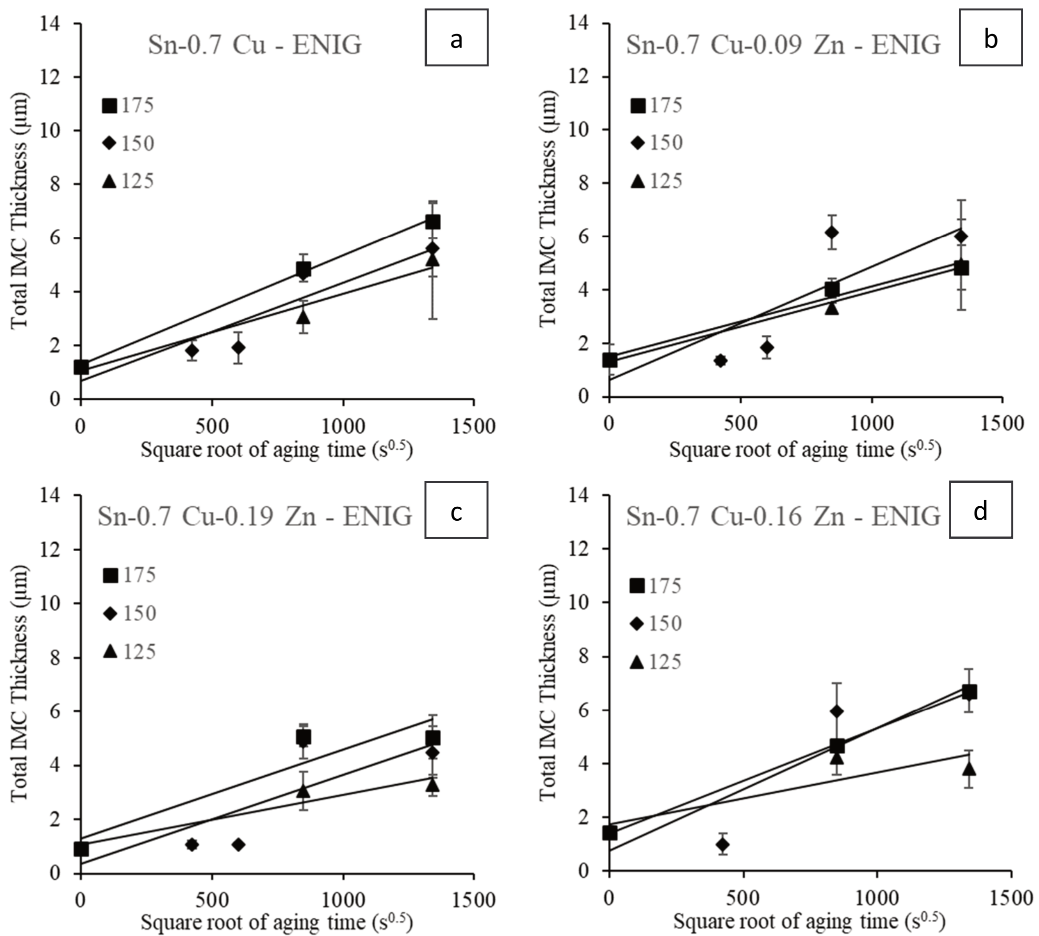

Figure 65: Total IMC thickness versus the square root of the aging time, at 125, 150 and 175 °C, for solders A (a), B (b), C (c) and D (d) using ENIG surface finish.

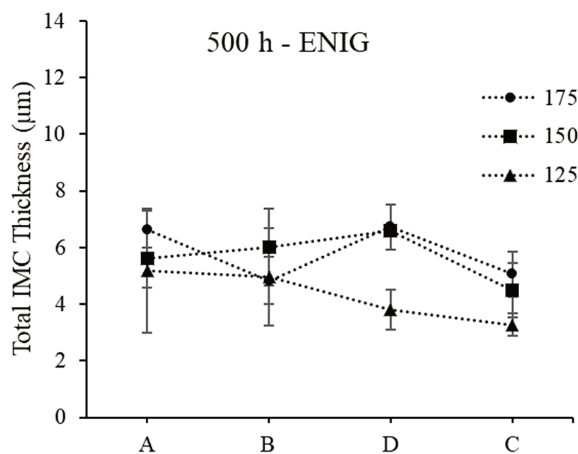

Figure 66: Comparison between each solder's total IMC thickness after 500 h of isothermal aging at 125, 150 and 175 °C.

4.2.2. Bulk IMC and grain size distribution

The microstructure evolution in the solder's bulk region upon aging was evaluated by cross sectioning samples and comparing the IMCs and grains morphologies. Figure 67 shows the characteristic bulk IMC morphology after 200 hours of aging at 3 different temperatures, 125, 150 and 175 °C, for solders A, B, C and D using OSP surface finish (each solder is identified on top of each column with the wt.% value for each element). In all cases, when comparison to the as-reflowed microstructure, it is possible to see that the IMC coalesced, always as Cu_6Sn_5, after thermal stress. Solders A and B, which have no and small amount of Zn, when aged at 125 °C still have some more dispersed IMC (sometimes it is possible to see a larger primary Cu_6Sn_5 with a faceted or hexagonal and hollow shape). Under higher temperatures, for this amount of time, solders A and B have most of its IMC turned into a round shape and large, often located at grain boundaries. With the addition of more Zn into the solder, the IMCs endured more its initial fine dispersion in the solder matrix.

Figure 68 shows images of the same samples of figure 67 but using cross polarized light. Apparently, for all solders, the grains coalesce proportionally to the aging time and temperature. Solders A and B have a morphology mixed between full twinned and interlaced grains, and the Zn added solders showed larger grains, often a single grained solder. This may be due to the reduction in the undercooling with the addition of Zn.

Figure 69 shows the plot of all measurements of the grain sizes for each solder in the form of boxplots, so that the size distribution is clear for each solder. The data in these charts confirms the trend afore mentioned.

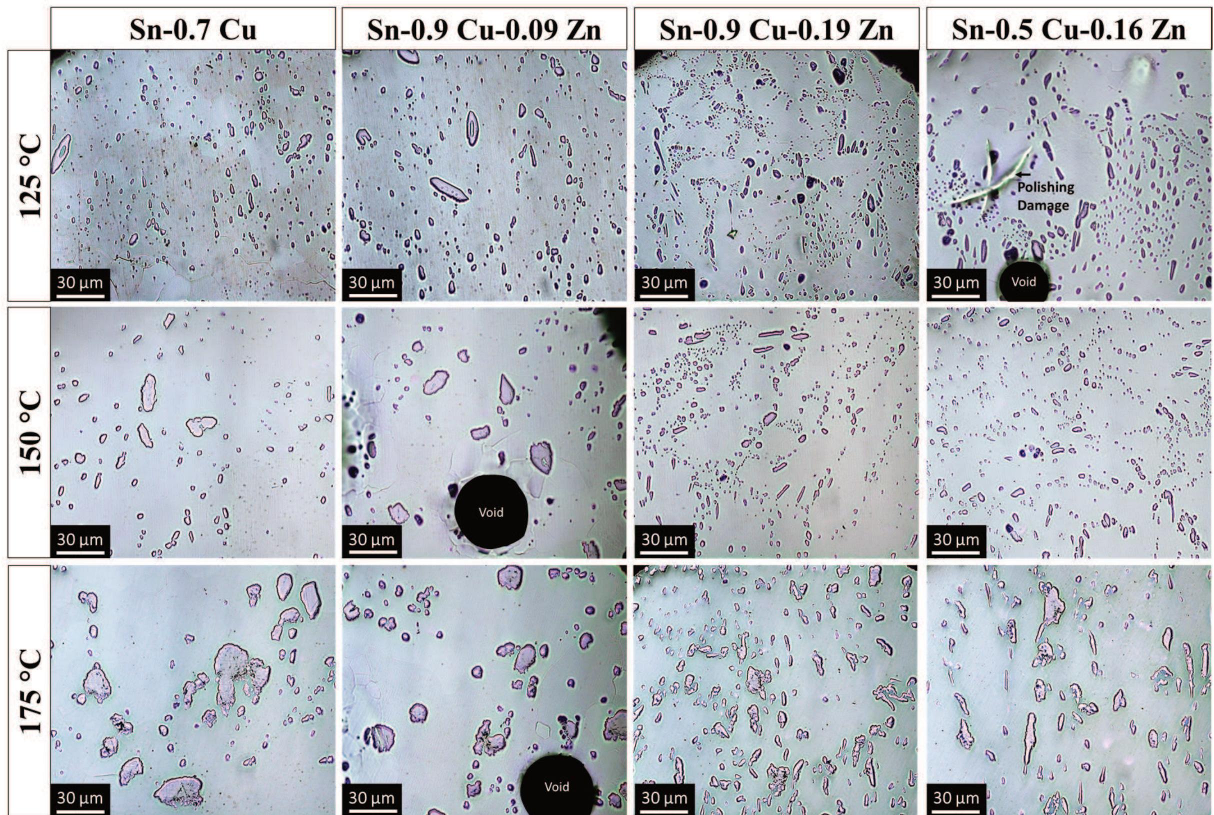

Figure 67: Characteristic IMC morphology obtained by optical microscope using bright field light after 200 hours of aging at 3 different temperatures, 125, 150 and 175 °C, for solders A, B, C and D using OSP surface finish.

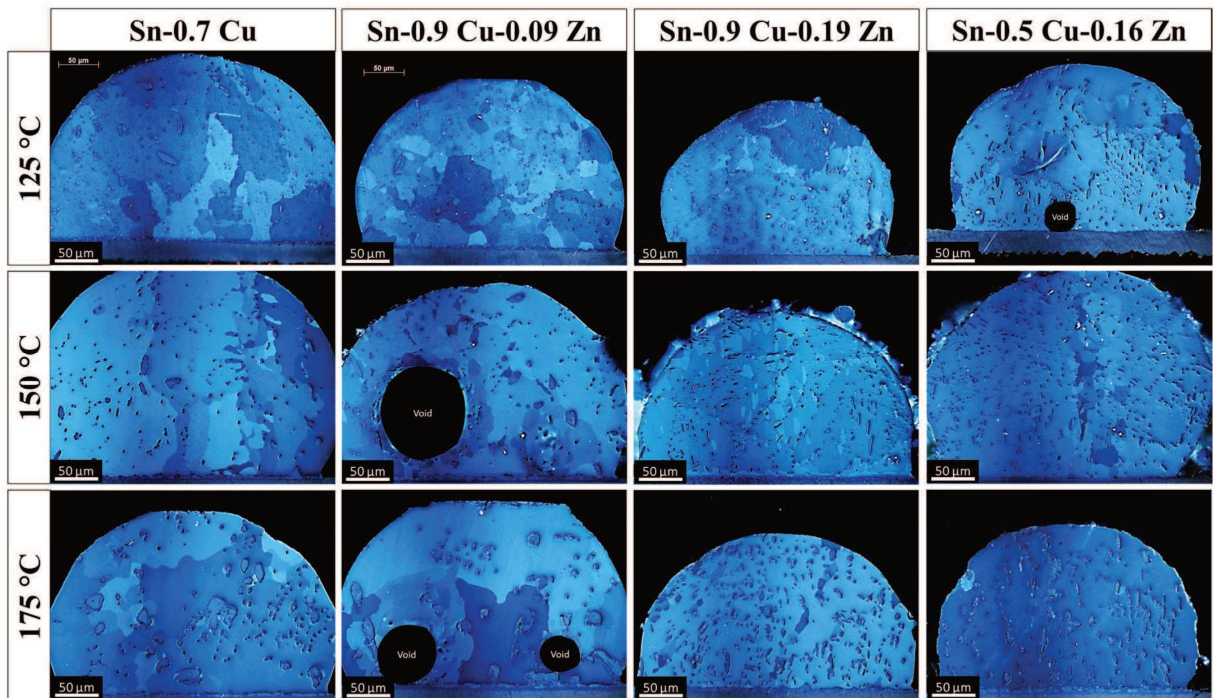

Figure 68: Characteristic IMC morphology obtained by optical microscope using cross polarized light after 200 hours of aging at 3 different temperatures, 125, 150 and 175 °C, for solders A, B, C and D using ENIG surface finish.

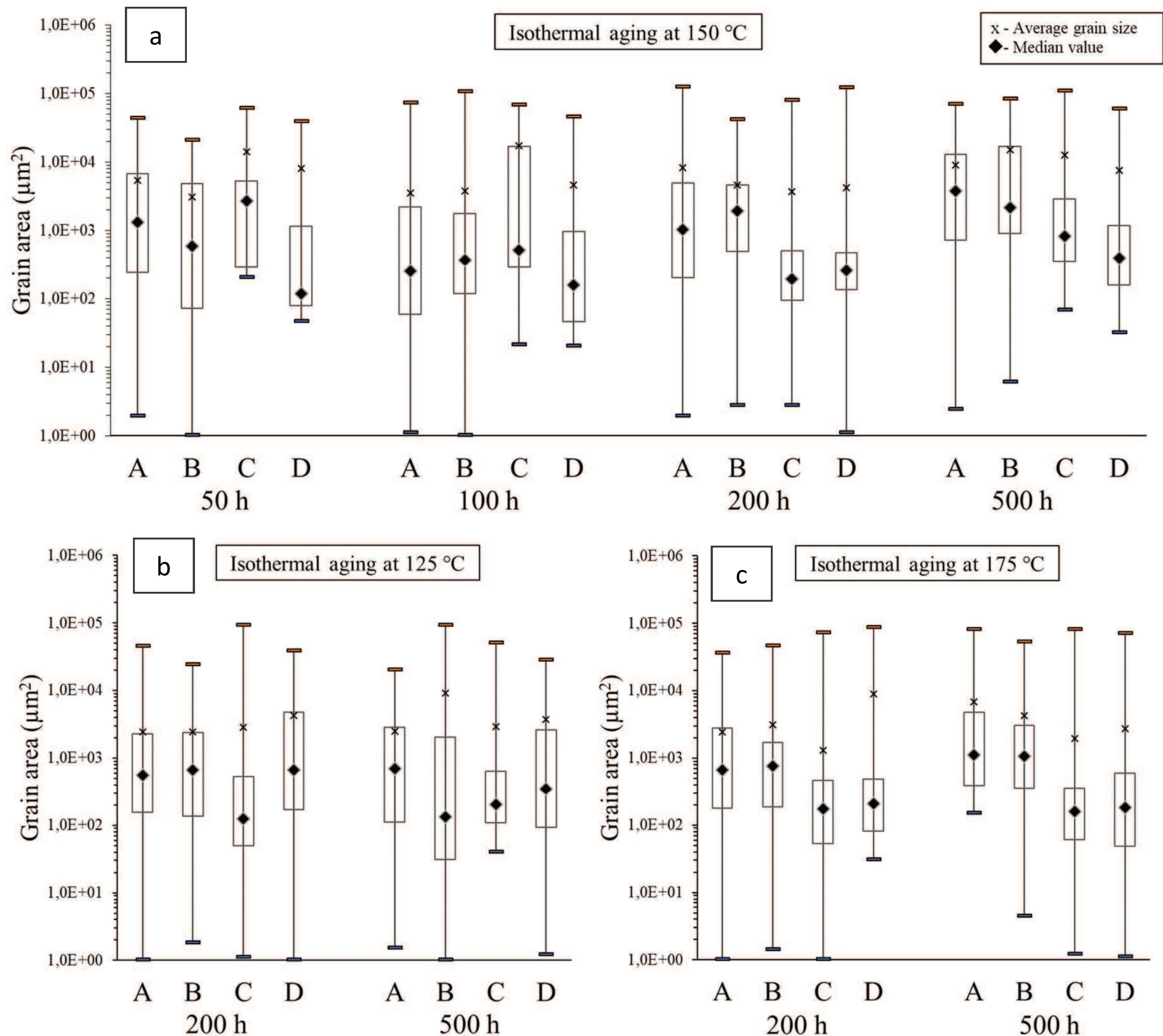

Figure 69: Boxplot charts of grains sizes for aged solders A, B, C and D and OSP surface finishes for various aging times ranging from 50 to 500 h and test temperatures of 150 °C (a), 125 °C (b) and 175 °C (c).

Analogously to the analysis above, here for samples that used ENIG surface finish, Figures 70 and 71 show images obtained by optical microscope with bright field light and images of the same samples but obtained using cross polarized light, respectively, and Figure 72 has the boxplot of all the measured grain sizes.

The IMC in the solder matrix are mainly $AuSn_4$ and Cu_6Sn_5 are also present. Often, large needle-shaped $AuSn_4$ appear in the solder matrix as seen in Figure 70. Upon aging at 125 °C, the IMCs are uniformly dispersed in the solder matrix, unlike the samples that used OSP. Solders C and D maintained a finer distribution of IMC, precipitated along grain boundaries, subgrain boundaries or interdendritic spaces, which can be confirmed when the location of IMC in Figure 70 and the grains morphologies shown in Figure 71. Figure 71 shows that most samples using ENIG surface finish aged at 125 °C have fine grain structure, which is not expected to be due to high undercooling, since the solder contains many elements that reduce the undercooling effect, such as Zn, Ni and Au. It is possible that there is recrystallization due to dynamic precipitation of IMC. From Figures 71 and 72 it is evident that there is a grain size increase with the aging temperature, however, this increase is lower in Zn added solders.

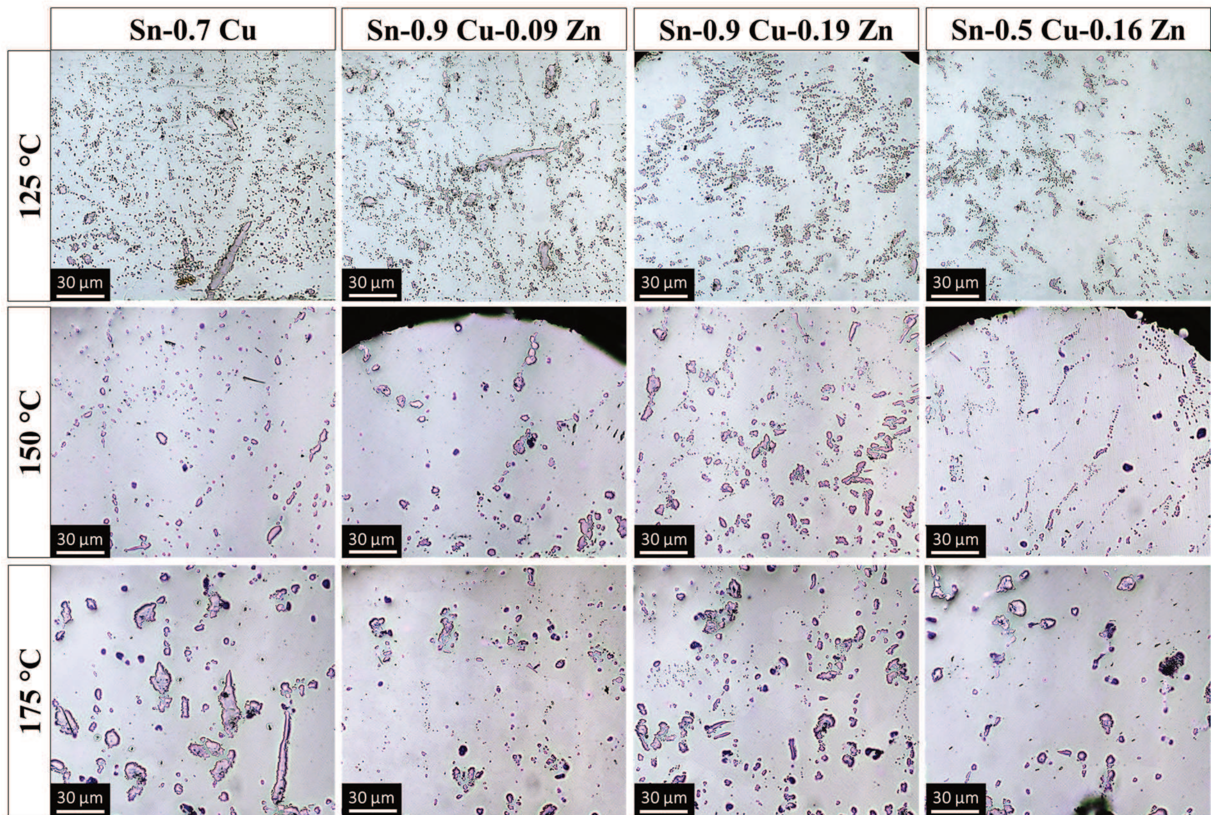

Figure 70: Characteristic IMC morphology obtained by optical microscope using bright field light after 200 hours of aging at 3 different temperatures, 125, 150 and 175 °C, for solders A, B, C and D using ENIG surface finish.

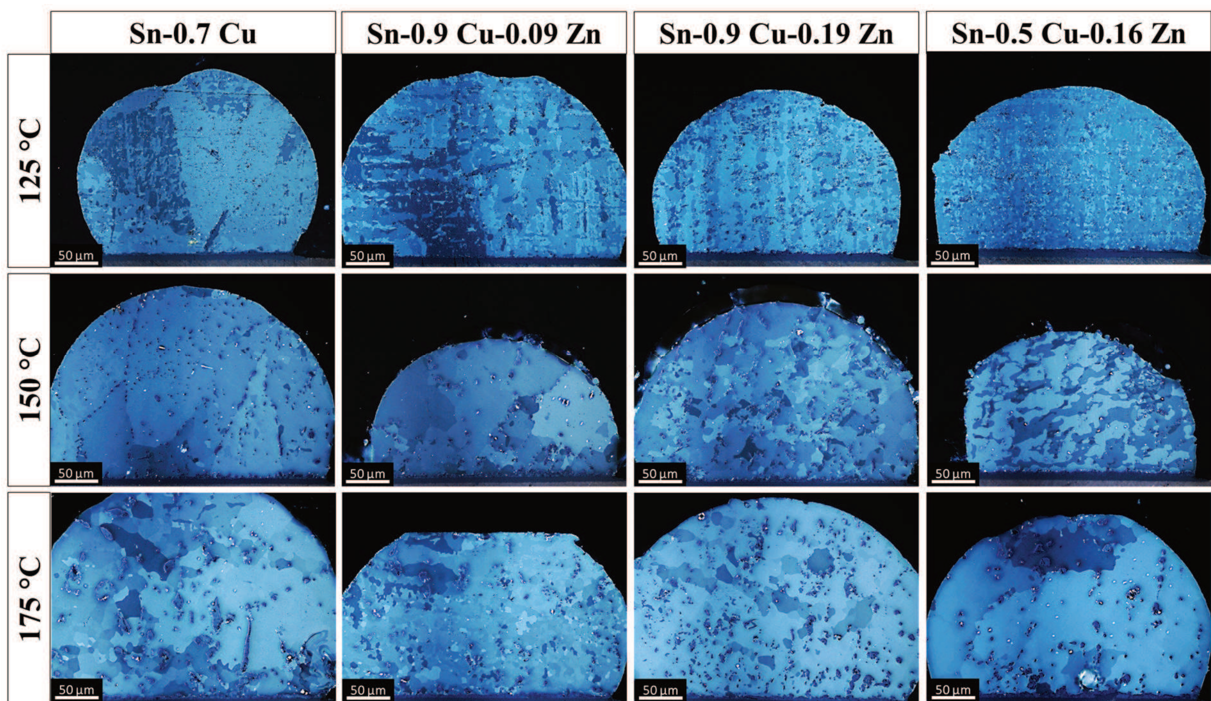

Figure 71: Characteristic IMC morphology obtained by optical microscope using cross polarized light after 200 hours of aging at 3 different temperatures, 125, 150 and 175 °C, for solders A, B, C and D using ENIG surface finish.

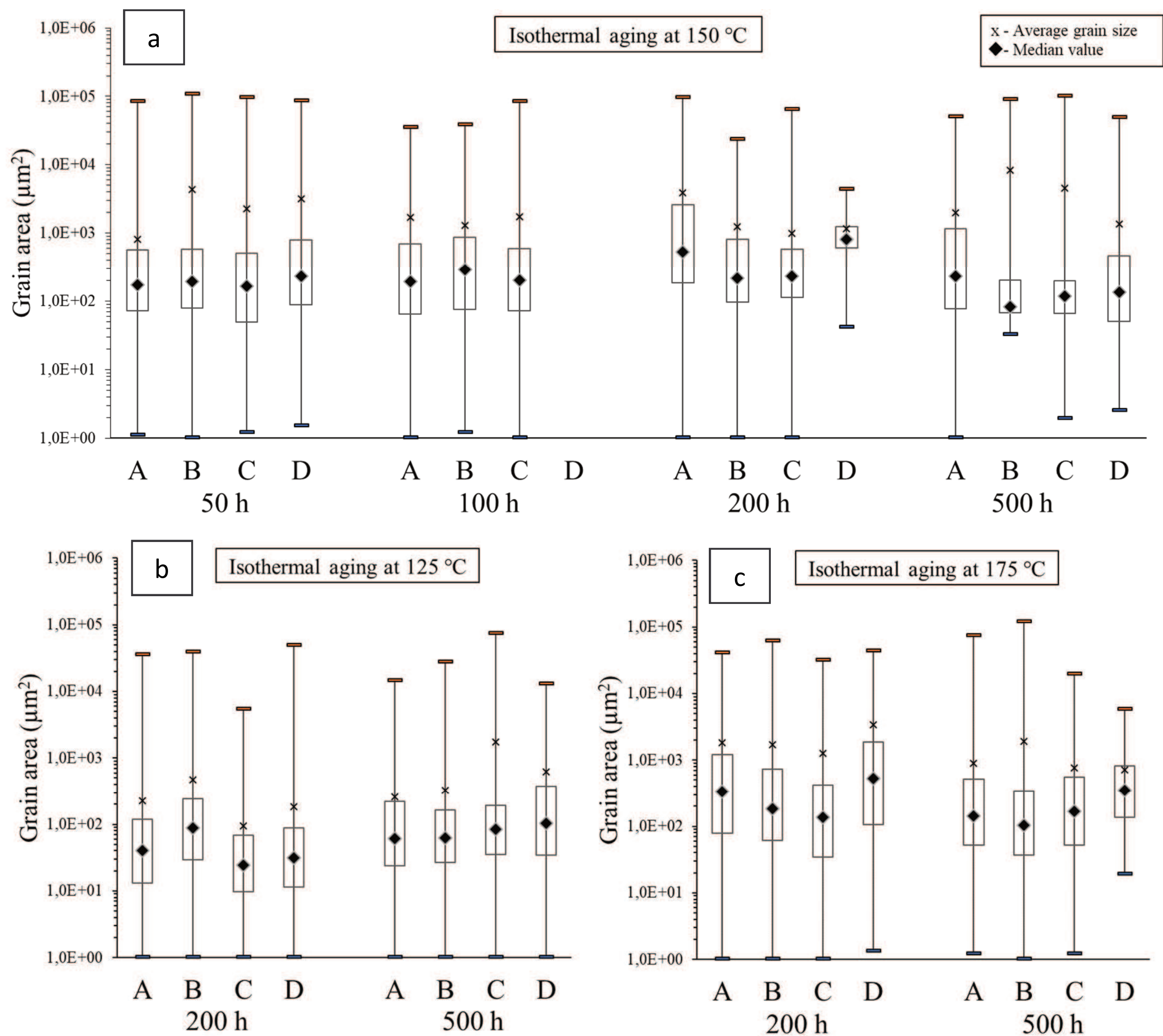

Figure 72: Boxplot charts of grains sizes for aged solders A, B, C and D and ENIG surface finishes for various aging times ranging from 50 to 500 h and test temperatures of 150 °C (a), 125 °C (b) and 175 °C (c).

4.2.3. Shear tests

The shear tests were conducted on solders in the as-reflowed condition and after aging. All sample conditions, regarding solder composition, surface finish, aging time and temperature were tested. Figures 73 and 74 provide the results of shear tests on solders using OSP and ENIG surface finishes, respectively. All charts contain the results for the tests on the as-reflowed condition as a reference.

As seen in the results of Figure 73, solder A had the highest shear strength between the solders used in this study in most of the conditions, solder B and C had intermediate values, and solder D varied greatly, from having the smallest shear force to the highest, upon aging at 150 °C. For aging at 150 and 125 °C, the average shear force increased with aging time.

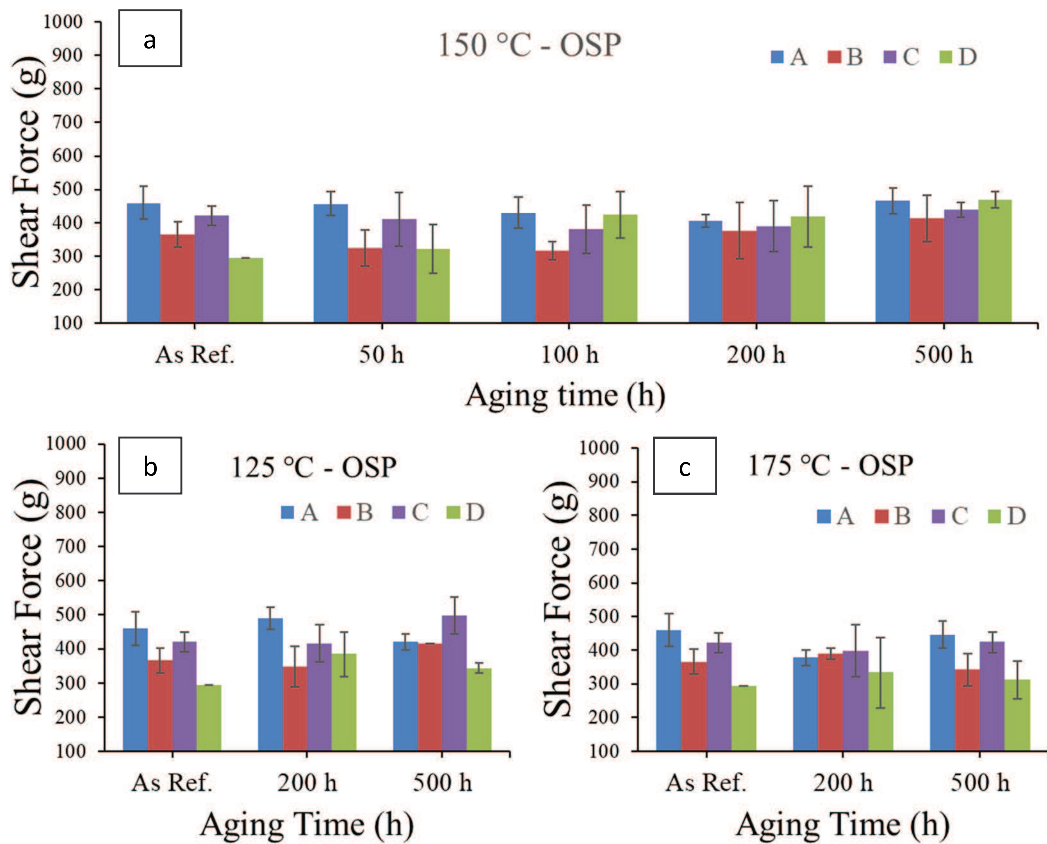

Figure 73: Shear force (g) vs aging time (h) for solders A, B, C and D using OSP surface finish and test temperatures of 150 °C (a), 125 °C (b) and 175 °C (c).

The solders using ENIG, as shown in Figure 74, had a higher shear force overall than OSP samples. It followed, nevertheless, the same trend in which solder A has the highest shear force, followed by solder B and C with intermediate values, and ultimately solder D had mostly the lowest shear force. It is worthy to mention that solder C in the results for 500 h had a peak of shear force. This may be due to the small grain sizes and the fine distribution of IMCs, as observed in the previous section.

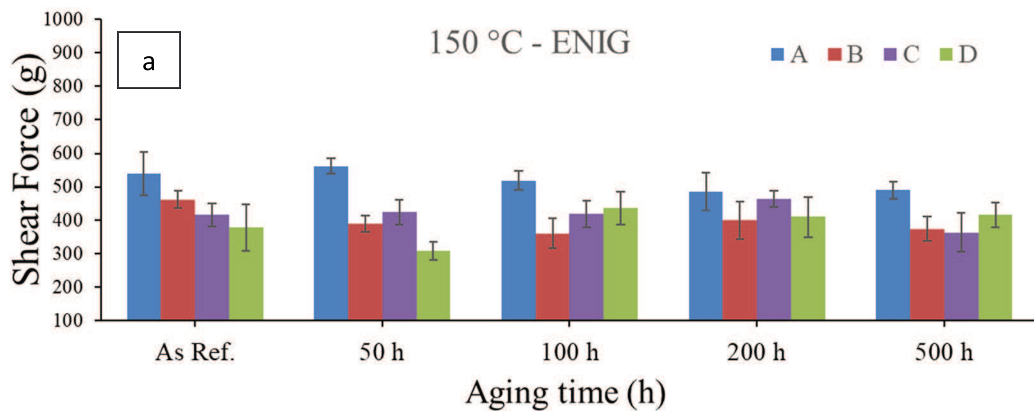

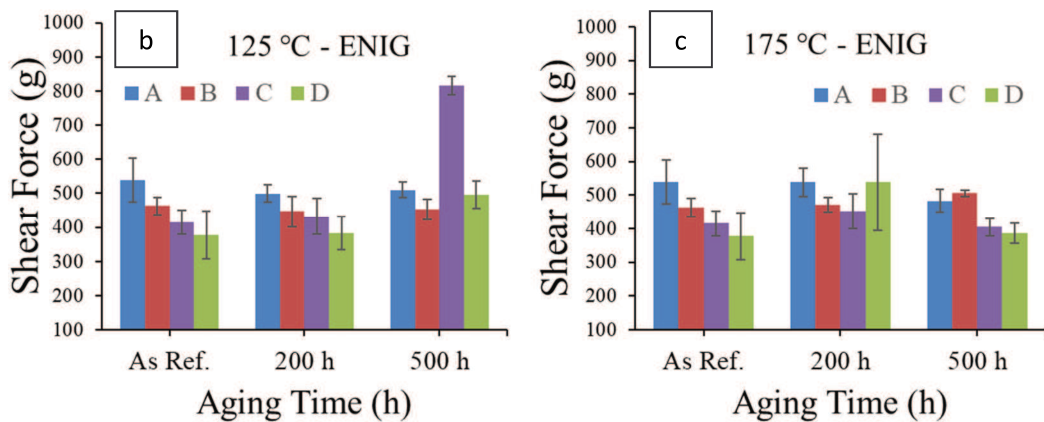

Figure 74: Shear force (g) vs aging time (h) for solders A, B, C and D using ENIG surface finish and test temperatures of 150 °C (a), 125 °C (b) and 175 °C (c).

The fracture surface was further analyzed with SEM and EDS elemental scan. The samples tested were solder A and C, aged at 125 °C for 500 h using ENIG surface finish, and aged at 175 °C for 500 h using both OSP and ENIG surface finish. It was found that all fractures had a ductile-dominant type of failure. The ductile fracture in the shear tests are characterized by parallel stretch marks left from the testing tool tip. See figure 75 with these results, including the EDS mapping of solders A and C aged at 175 °C for 500 h. Solder C aged at 125 °C for 500 h, which had the highest shear force values, presented marks on the shear surface that are probably grain boundaries. The solders aged at 175 °C presented some large Cu_6Sn_5 within the solder, and the amount of these IMCs is larger in solder A. The EDS mapping results show that none of the interfacial IMC was exposed, otherwise the Cu count in such region would be high, and Sn count would be lower than the matrix.

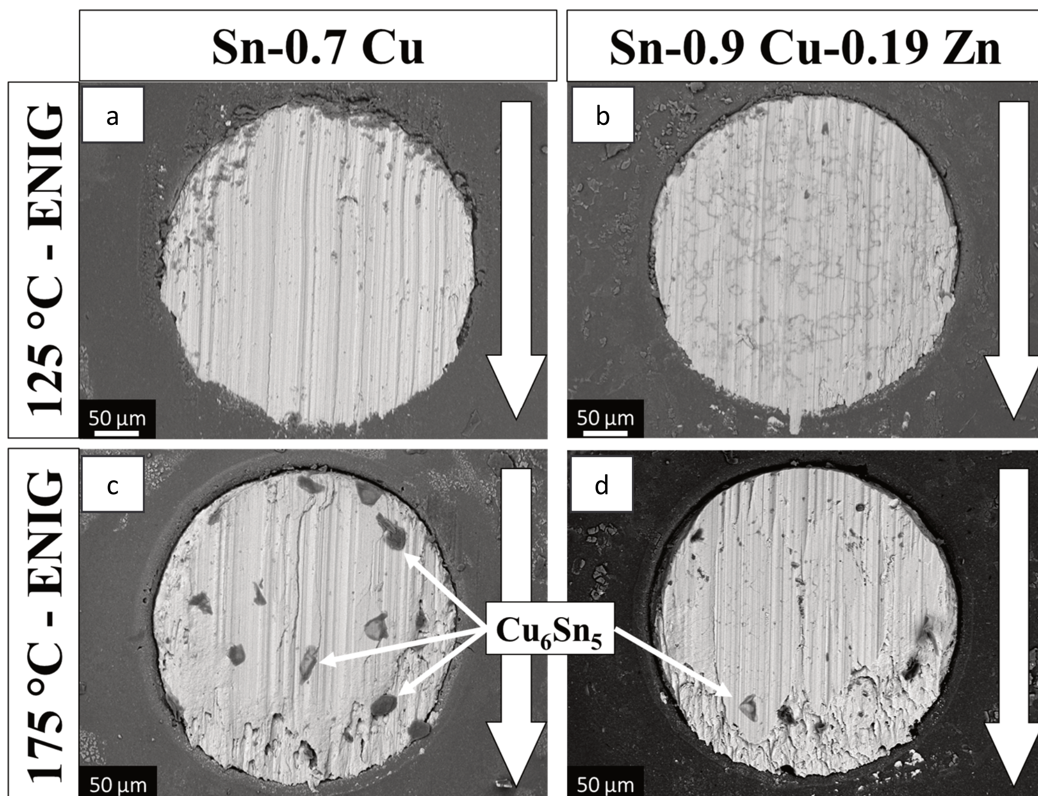

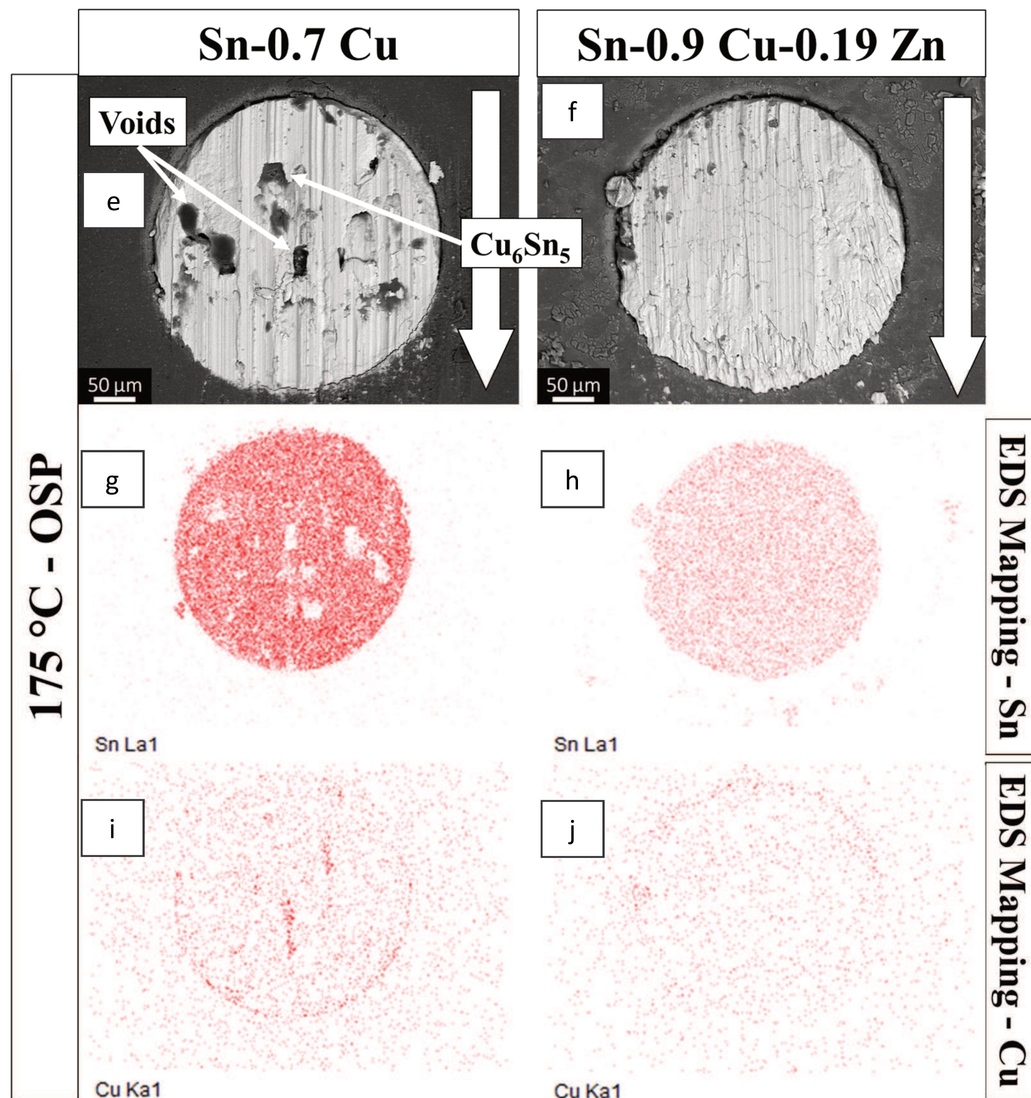

Figure 75: Shear pattern of solders A and B (Sn-0.7 wt.%Cu and Sn-0.9 wt.%Cu-0.19 wt.%Zn) aged for 500 h for the following test temperature and surface finish for A and B, respectively: 125 °C and ENIG (a) and (b); 175 °C and ENIG (c) and (d); 175 °C and OSP (e) and (f). EDS mapping for solders A and B for the following elements, respectively: Sn (g) and (h); and Cu (i) and (j).

4.3. Electromigration

4.3.1. Resistance change during the tests

During the electromigration tests, the voltage and current were sampled once per second and recorded, therefore the resistance could be calculated. The majority of samples had a resistance change (R/R_0) below 8% within the test time (up to 200 h), which was desired, since greater resistance change could lead to melting of the interconnect and then the EM properties would change. Figure 76 shows the curves of the resistance change versus time in hours during EM tests for 3 different samples. These samples were soldered with solder A, and these curves are shown to exemplify possible behavior during the tests. No correlation could be drawn from comparing the resistance change between different solder alloys in this study, due to the

relatively short test time. Some peaks that can be seen in the curves are due to changes in the temperature of the room where the experiments were taking place.

The curves identified as for samples A1 and A2 had a constant increase in resistance, however the curve for sample A2 achieved 6% of resistance change after 180 h, while the sample A1 reached 5 % in the same time. It means that at this point, the sample A2 was around 10 °C hotter than sample A1, and that the thermal induced changes in microstructure were more intensified. The curve for A3 indicates that the sample had a partial failure, since the resistance increased suddenly and started oscillating. A cross section in the failed joint revealed a void at the anode interface between solder matrix and Cu trail (figure 77). This type of so-called pancake void forms due to the mismatch between diffusivity rates of Cu and Sn due to electromigration – the diffusivity of Cu is higher than of Sn, so at some point Cu is depleted to the point of creating a void – more on this is discussed on section 4.3.3.

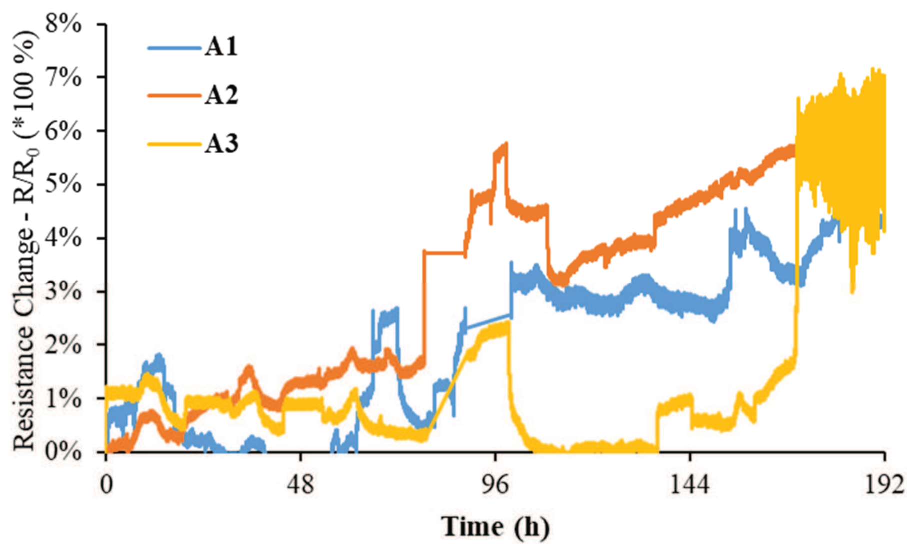

Figure 76: Resistance change (*R/R0*) versus time during electromigration tests for three different samples using solder A and OSP surface finish.

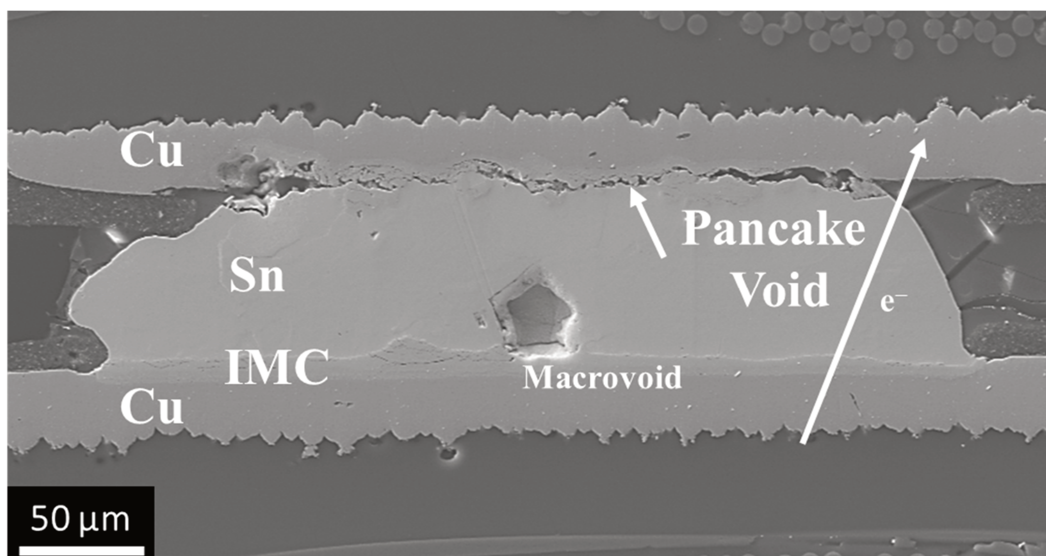

Figure 77: Solder joint exhibiting a propagate pancake-type void after current stress during an electromigration test. The sample used solder A and OSP surface finished.

4.3.2. Characterization of compounds formed after electromigration tests

The application of current to the solder joints caused the substrate materials to diffuse into the solder matrix and form intermetallic compounds. The morphology varied greatly between each joint, however the formed compounds had similar composition when same surface finish was used. Figure 78 exhibits two couples of solder joints that used OSP surface finish after 200 h of EM stress. The joints (a) and (b) are a couple fabricated with the solder alloy B, and the joints (c) and (d) are a couple fabricated with the solder alloy C. The couple (a) and (b) were greatly affected by the EM stress. The IMC formed in a great area of the solder matrix. The couple (c) and (d) was less affected and the shape of the IMC on the left side it was formed at the edge of the solder, and on the right side, instead of growing from the substrate towards the anode like in the other joints, this one formed IMC on the cathode, which means that the Cu diffused into the matrix without forming an intermetallic. Both cases of formation of the IMC are possible and were observed in other joints (more will be discussed in the next section).

The compounds in the joints of Figure 78 were analyzed by EDS and the results are shown on Figure 80. The large IMCs formed within the bulk are Cu_6Sn_5 and there is Cu_3Sn formed at the interface of the Cu_6Sn_5 IMC and the Cu pads. Solder C, which did not form Cu_3Sn even after 500 h of aging at 175 °C here exhibits a certain amount of this IMC in some regions of the interfaces.

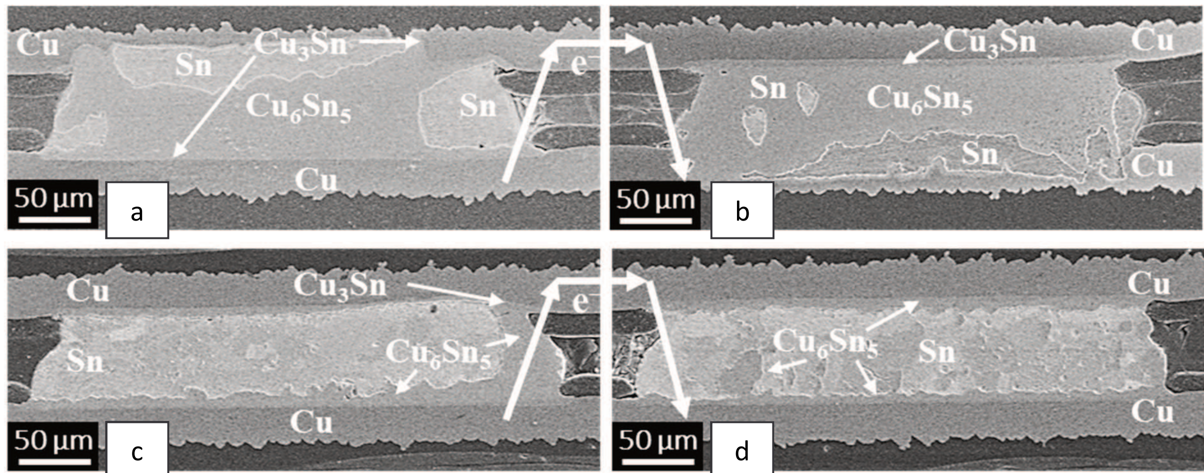

Figure 78: SEM image of solder joint couples stressed for 200 h in the electromigration tests. Both couples used OSP surface finish. It was used solder B for fabrication of the couple on the images (a) and (b), and the solder alloy C for the couple on the images (c) and (d).

Figure 79 exhibits two joints of solder joints that used ENIG surface finish after 200 h of EM stress. The joint (a) was fabricated with solder alloy A, and the joint (c) was fabricated with solder alloy C. The joint (a) shows little formation of IMC, while the joint (b) forms a considerable amount of IMC growing from the cathode into the solder bulk. The formed compounds were analyzed by EDS and the results are shown on Figure 81. In the joint (a), the IMCs formed in the bulk were mainly $(Ni,Cu)_3Sn_4$ which denotes that some Cu from the trails diffused through the Ni-P layer considering its at.% amount, and at the cathode surface, a $(Au,Ni)Sn_3$ IMC as thick as 10 µm was formed. The compounds of the joint (b) are also shown in Figure 81, and show that the large IMC at the cathode contains an intricate structure of $(Au,Ni)Sn_3$ and Ni_3Sn_4. Some regions with $(Au,Ni)Sn_3$ IMC are outlined with an yellow dashed line in Figure 79 (b). It was observed that no Cu was found into Ni_3Sn_4 IMC. A line-EPMA

analysis was performed over the IMC, in the region indicated by the white dashed line on Figure 79 (b), and the results are shown on Figure 82. It is possible to see that there is a low amount of Cu into the Ni-Sn IMC when compared with other EPMA analysis over Ni-Sn IMCs (see figure 52), and there is Zn spread throughout the IMC and Ni-P layer. The presence of Cu in Ni-Sn IMC at the cathode interface of the joint (a), which had no Zn alloying, leads to the suggestion that the Zn may hinder the diffusion of Cu through the Ni-P layer and Ni-Sn IMC.

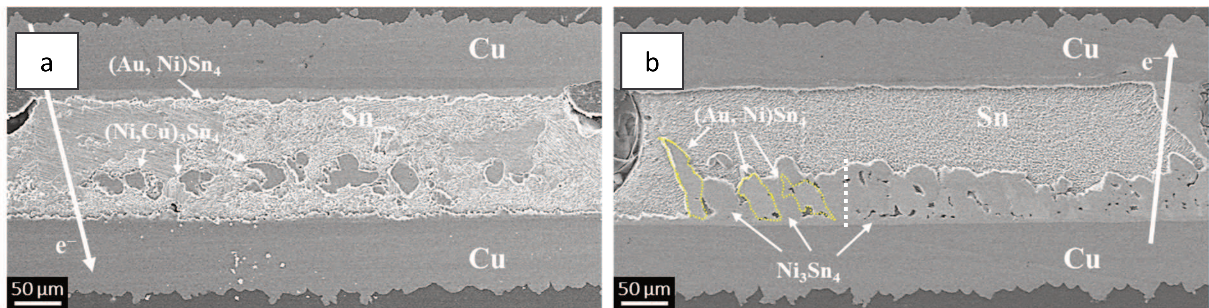

Figure 79: SEM image of solder joints stressed for 200 h in the electromigration tests. Both joints used ENIG surface finish. It was used solder A for fabrication of the joint on the image (a), and solder C for the joint on the images (b). The white dashed line indicates the location where EPMA line scan took place.

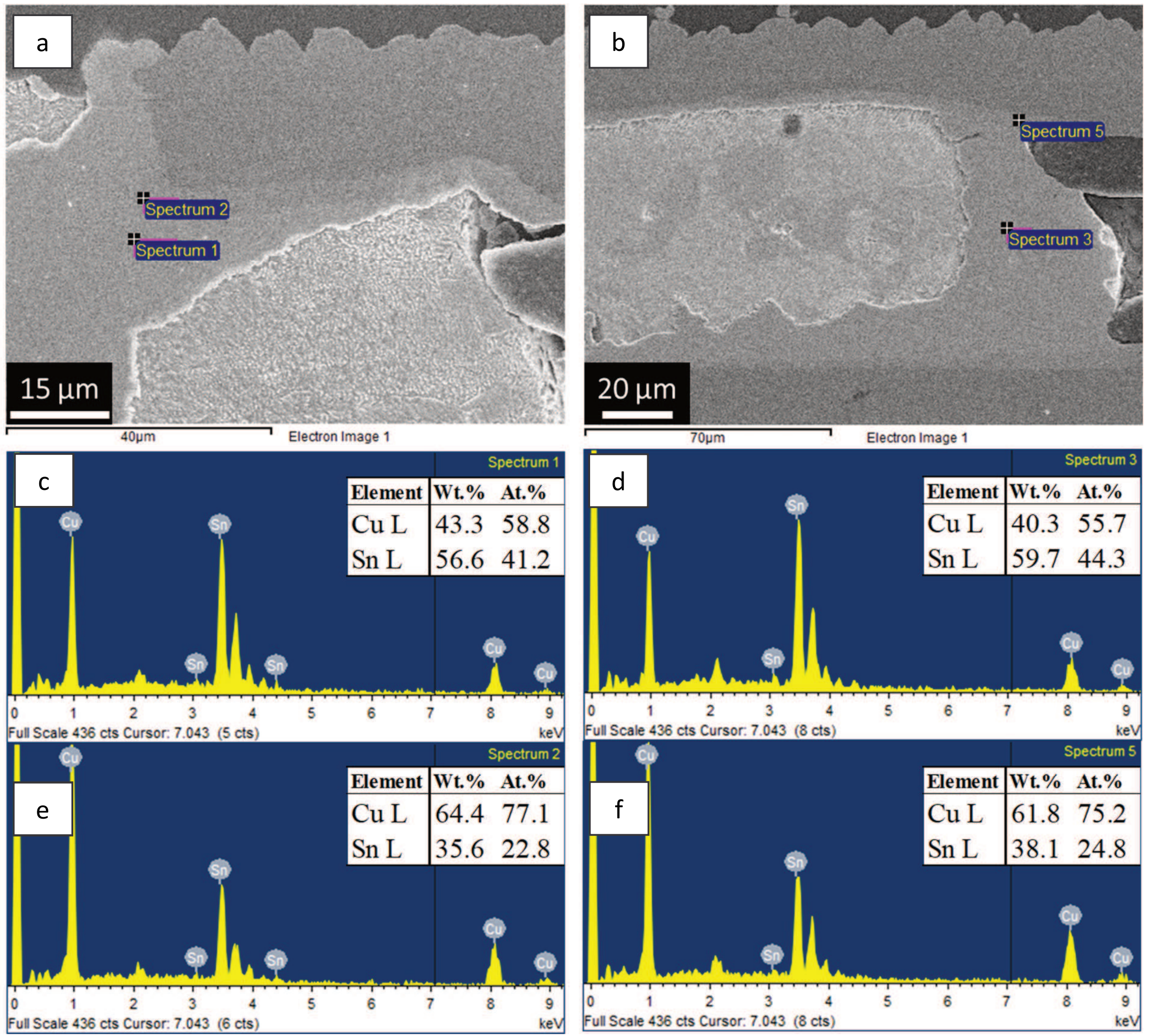

Figure 80: EDS analysis of different IMC compounds formed during 200 h of electromigration tests. Both joints used OSP surface finish. The joint (a) was fabricated with solder B and the spectrum of each point analyzed is shown on Figures (c) and (e). The joint (b) was fabricated with solder C and the spectrum of each point analyzed is shown on Figures (d) and (f).

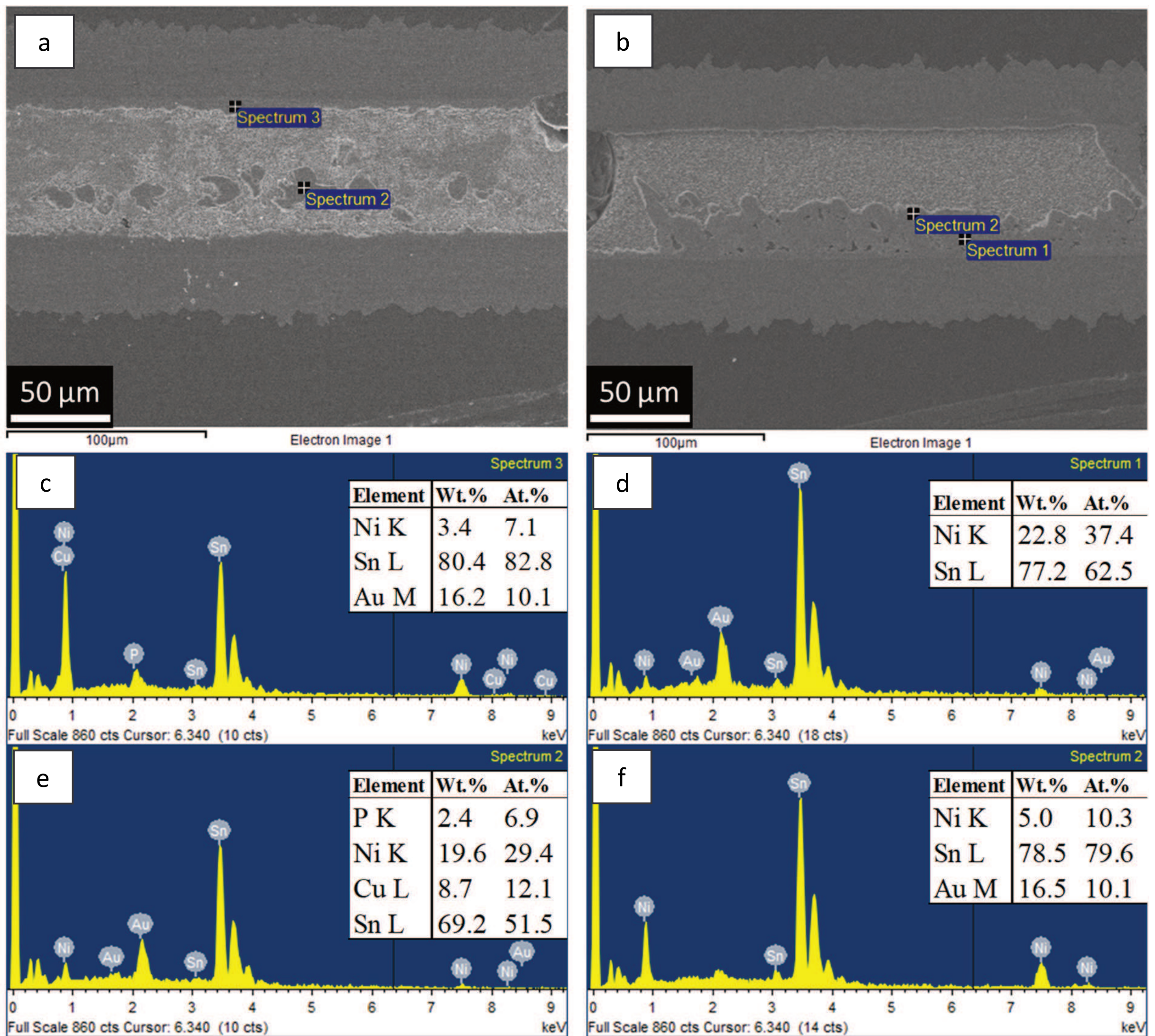

Figure 81: EDS analysis of different IMC compounds formed during 200 h of electromigration tests. Both joints used ENIG surface finish. The joint (a) was fabricated with solder A and the spectrum of each point analyzed is shown on Figures (c) and (e). The joint (b) was fabricated with solder C and the spectrum of each point analyzed is shown on Figures (d) and (f).

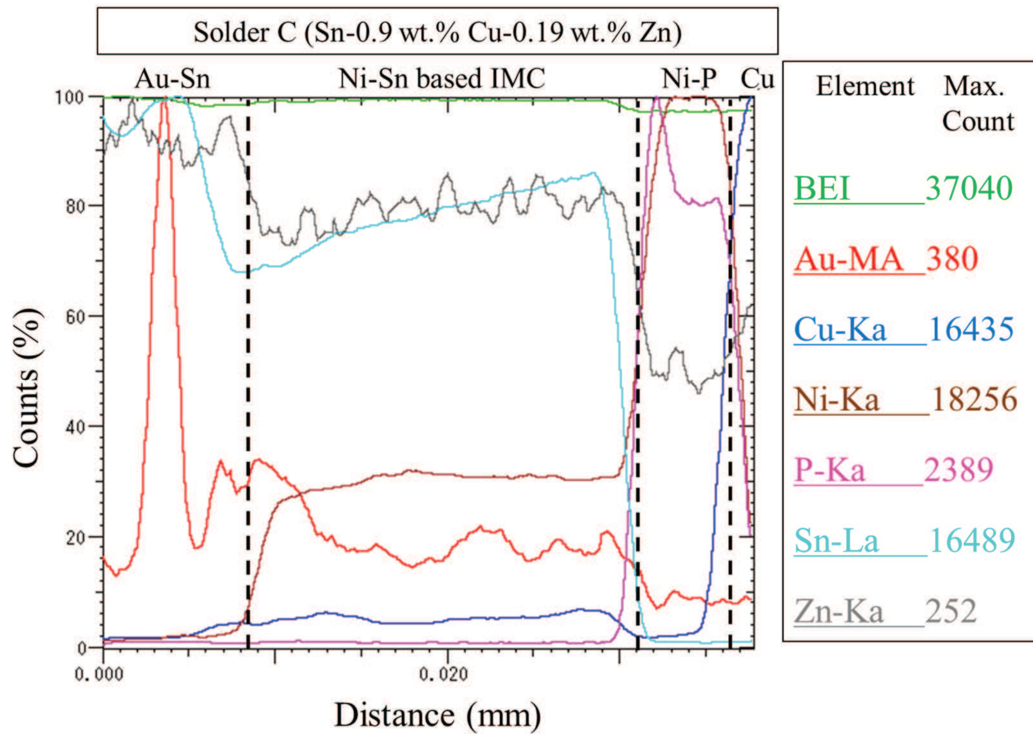

Figure 82: Line EPMA scan over an IMC formed at the cathode of a test sample that underwent 200 h of current stress. The joint was fabricated with solder C and ENIG surface finish.

4.3.3. Grain orientation analysis

As mentioned in the section 2.3.5.4, the diffusivity of Cu and other alloying elements during high current application, is higher along the c-axis of the BCT lattice structure of β-Sn grains. Thus, after the electromigration tests, an analysis of the grains' orientations was carried out utilizing the EBSD method. The inverse pole figure maps obtained from the images used as reference axis the transverse direction, which was parallel to the current flow direction when the images were obtained. This means that when the c-axis is parallel to the current flow, the grain in the map will be shown with a reddish color, since the 001 plane is normal to this direction, and as a standard the red color is used for when the 001 plane is normal to the reference axis. This is illustrated in figure 83.

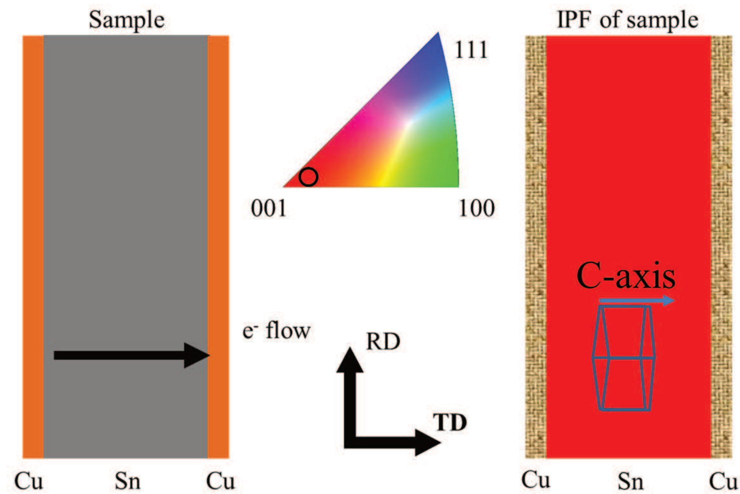

Figure 83: Illustration of a sample with a single grain with its orthogonal c-axis oriented parallel to TD and the result in terms of the inverse pole figure map.

Figure 84 shows the cross section of a sample that used solder A and OSP surface finish that underwent current stress for 50 h. It is possible to see that the diffusion inside a solder joint can happen non-uniformly, depending on how parallel the c-axis of a grain is to the direction of the current flow. In this sample, the cathode was at the bottom side of this image, and it is seen that there was diffusion of Cu into the solder matrix preferentially in 2 grains that had the c-axis most parallel to the current flow. At the left top corner of the sample there are grains with c-axis transverse to the current flow, which appear with a blue color. When the cu reached the boundaries of this grains, it stalled and accumulated, forming an IMC.

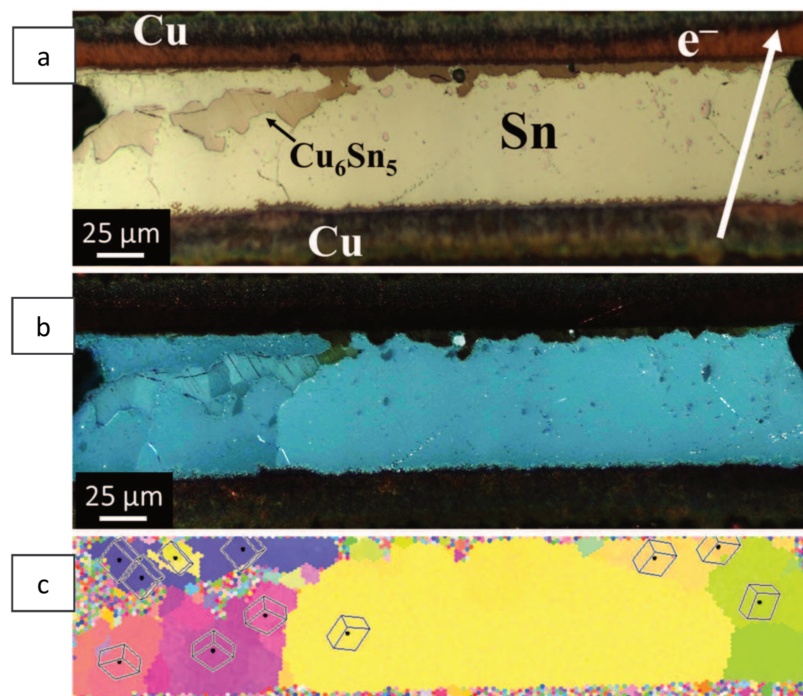

Figure 84: Bright field image (a), cross polarized light image (b) and inverse pole figure map (c) of cross section of joint fabricated using solder A and OSP surface finish that underwent 50 h of electromigration stress.

The sample of Figure 85 was shown previously in the section 4.3.1, Figure 77. It had failed before 200 h of EM stressing and the cross section revealed a pancake shaped void. An EBSD analysis was carried out for this sample, and the IPF map is shown in figure 85 (c). Figure 85 (b) has a image obtained with cross polarized light optical microscope, used as reference to confirm the microstructures. Two grains are dominant near the cathode, which appear as purple and blue colors in the IPF map, and they have orientations almost transverse to the current flow. This makes the diffusion of Cu into the solder matrix very slow, however, at the anode the Cu is carried by the electron cloud by self diffusion and gets depleted at the anode interface with the solder. The Sn does not migrate fast enough to compensate for this depletion, and since there is no Cu flowing from the cathode to the anode, a void ripped open and caused the failure of the joint.

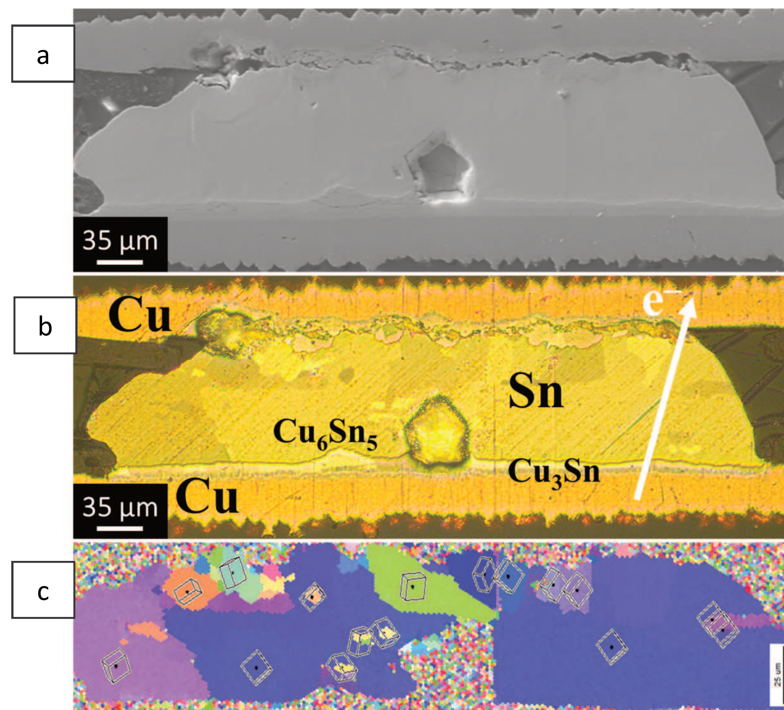

Figure 85: SEM image (a), cross polarized light image (b) and inverse pole figure map (c) of cross section of joint fabricated using solder A and OSP surface finish that underwent 200 h of electromigration stress.

Samples with different Zn content but similar Sn grain orientation had similar results in terms of Cu diffusion into the solder and IMC growth. Figure 86 contains two samples stressed fabricated using OSP surface finish and solders A (a) and C (b). The sample (a) was stressed for 50 hours and the sample (b) for 100 h. Both grain orientations have c-axis almost parallel to the current flow, which allowed great diffusion of Cu into the solder, forming large Cu_6Sn_5 grains grown from the cathode towards the anode, as can be seen in Figures 86 (c) and (d). The sample (a) formed a considerably thick Cu_3Sn near the cathode and near the anode in the region where the current was flowing, whereas the sample (b) only formed this IMC near the anode. The presence of Zn may have suppressed the formation and growth of Cu_3Sn at the cathode, with the same mechanism that takes place during aging, however at the anode the initial structure is carried away and replaced by new atoms of Cu and Sn, so the amount of Zn in this region may be not enough to hinder the growth of this IMC. The growth rate in solder (b) is higher than in solder (a), which can be due to the orientation in sample (b) be slightly more leaned towards the region where current gets crowded at the anode.

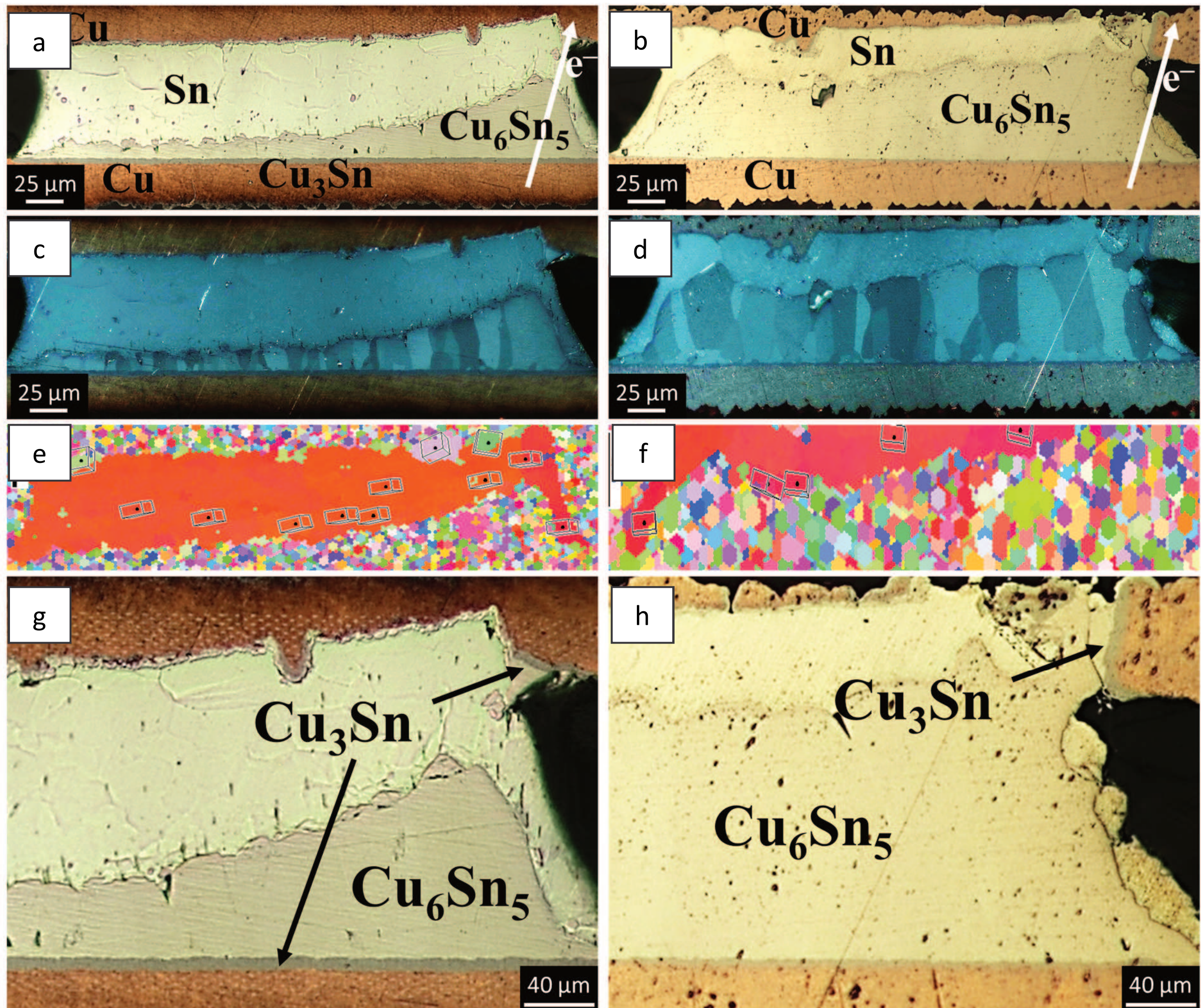

Figure 86: Bright field images (a) and (b), cross polarized light images (c) and (d), inverse pole figure maps (e) and (f) and zoomed in bright field image (g) and (h) of cross sections of joints fabricated using, respectively, solder A and solder C, and OSP surface finish that underwent, respectively, 50 and 100 h of electromigration stress.

Samples using ENIG surface finish were stressed for 50 h and the cross section and IPF maps are shown in figure 87. The solder alloys used were A, B, C and D, and bright field OM images are shown in, respectively, (a), (b), (g) and (h); cross polarized OM images are shown in, respectively, (c), (d), (i) and (j), and the inverse pole figure maps are shown in (e), (f), (k) and (l). It is noted that there was growth of Au_3Sn and Ni_3Sn_4 IMCs due to the favorable Sn grain orientation in the bulk – the solders that have a more reddish color tone hat higher IMC growth. However, the most important factor is the orientation of c-axis in relation to the current flow. The sample (a) possesses a more reddish color than sample (c), however the sample (c) grew larger IMC. It is possible to note by the cubes drawn in the IPF maps that the grains in the sample (a) were less misoriented in relation to TD, however the sample (c) had its Sn grains with c-axis oriented towards the current crowding region, and it is possible to see that the IMCs grow in the same direction. No conclusion could be drawn in respect to the Zn alloying in these solders in terms of microstructure morphology and evolution.

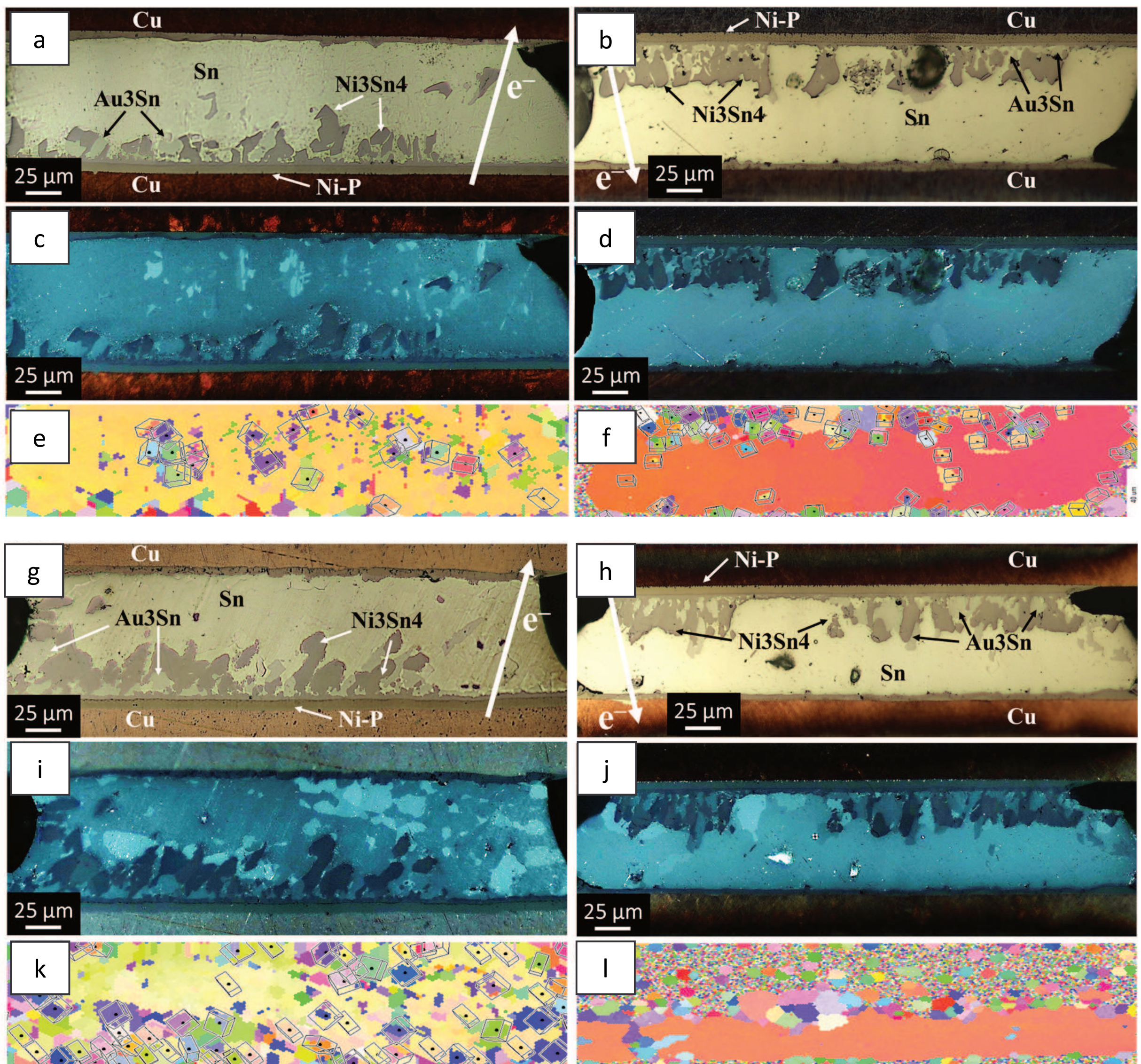

Figure 87: Cross section of samples that underwent 50 h of electromigration stress and were fabricated using ENIG surface finish. The solder alloys used were A, B, C and D, and bright field OM images are, respectively, (a), (b), (g) and (h); cross polarized OM images are, respectively, (c), (d), (i) and (j), and the inverse pole figure maps are, respectively, (e), (f), (k) and (l).

CHAPTER 5. SUMMARY AND CONCLUSIONS

5.1. As reflowed condition

Sn-based Pb-free solders were obtained and prepared for microstructure evaluation upon aging and electromigration stress. The final composition of the solders were determined to be as follows, and they were identified as, respectively, solders A, B, C and D: Sn-0.7 wt.% Cu, Sn-0.9 wt.% Cu-0.09 wt.% Zn, Sn-0.9 wt.% Cu-0.19 wt.% Zn, and Sn-0.5 wt.% Cu-0.16 wt.% Zn. They were prepared in samples as solder balls for isothermal aging experiments and as couple joints for electromigration experiments. The preparation included printing of solder paste, reflow at 260 °C for 1 minute.

(1) Zn and Sn were expelled with the flux in Zn added solders reflowed in air. Zn added solders (B, C and D) lost around 83 wt.% of its Zn content, Solder A lost 2 wt.% of Sn, B and C solders lost 12 wt.% of Sn and D lost 3 wt.% of its Sn.

(2) The samples that used OSP formed Cu_6Sn_5 at the interface of solder and substrate and within the solder matrix and the shape of the interfacial IMC turned into more scalloped with the addition of Zn, and its size decreased from 3 µm, for solder A, to 1,5 µm for solder C.

(3) Near-eutectic solder compositions promote fine dispersion of IMCs at the bulk, being the nearest the solder B and the farthest the solder D. Solder A had large primary IMCs and interlaced grain structure, denoting large undercooling. The addition of Zn and Cu appear to decrease primary IMC sizes and the quantity of interlaced grains.

(4) The samples that used ENIG surface finish formed $(Ni,Cu,Au)_3Sn_4$ at the interface needle-shaped $(Au,Ni,Cu)Sn_3$ crystals were found to grow on top of it. The addition of Zn in the solders suppressed the growth of the modified AuSn3 crystals and the Au contents in the modified Ni_3Sn_4 IMC.

(5) The IMC thickness for all ENIG samples was smaller than for those using OSP surface finish, and the addition of Zn also decreased its total average size to less than 1 µm with 0.19 wt.% Zn using ENIG surface finish.

(6) At the bulk of ENIG samples, the addition of Zn caused the precipitation of Au-Sn based IMCs often in grain boundaries, due to its affinity for noble elements, which diffuse from the surface finish during reflow.

(7) The ENIG samples presented more medium to small grains than OSP samples for same solder compositions. Assuming that the undercooling was not significantly affected by Au and Ni elements, it is speculated that the formed Au-Sn based IMCs are propitious to heterogeneous nucleation of Sn grains.

5.2. Aging experiments

For the isothermal aging experiments, the temperatures used were 125, 150 and 175 °C, and the aging time was up to 500 h. Identification of phases, evolution of IMCs and grains morphologies and shear strength were assessed.

(1) For the OSP solders, Cu_3Sn was formed between the Cu_6Sn_5 IMC and the Cu substrate. The addition of Zn suppressed completely its growth with 0.19 wt.%, and the total IMC thickness also decreased. This can be beneficial to a solder joint since the Cu_3Sn IMC growth causes induces formation of microvoids, there are less phases with different lattice constants, which decreases the bonding strength and the IMC is a brittle material, which can hinder mechanical properties of the joint.

(2) The ENIG samples had an IMC around 50% smaller than solders using OSP, and the addition of Zn decreased even further the IMC thickness.

(3) The bulk IMC coalesced upon aging, however the addition of Zinc made these IMCs more stable and decreased this effect. The same trend was observed with the grain sizes, however for low aging temperature of 125 °C the microstructure was found to be much finer, which indicates recrystallization of the grains. Further studies are needed to understand this phenomenon.

(4) The shear strength was evaluated for samples in as-reflowed and aged conditions. Solder A had, overall, higher shear strength than the other solders for both surface finishes, but performed better with ENIG, having a maximum shear force of, in average, 550 g, versus 459 g for OSP.

(5) Other solders generally performed poorly, except for the Zn-added solders C and D in the lower temperature aging condition, where the shear force reached 800 g for solder D. This can be consequence to fine sized grains and also IMC dispersed through the grain boundaries.

5.3. Electromigration experiments

The electromigration tests were performed with application of a current of 3.25 A and the test sample temperature was 150 °C. The samples were stressed for up to 200 h and the microstructure was evaluated. The phases were identified, the microstructure evolution was observed and grain orientation was determined in order to understand the electromigration effects.

(1) For the OSP samples, it was observed that Cu is drifted by the electron clouds and, from the cathode, it causes the growth of Cu_6Sn_5, and at the anode, it causes UBM depletion.

(2) Cu3Sn was found to grow as expected for low or no Zn added solders, and Zn suppressed its growth at the cathode, but the modification of the anode structure through drift and replacement of atoms allowed Cu_3Sn to form in this region.

(3) The ENIG samples formed basically $(Ni,Cu)_3Sn_4$ and $(Au,Ni)Sn_4$ at the cathode interface and also bulk. The addition of Zn decreased the amount of Cu into the $(Ni,Cu)_3Sn_4$.

(4) EBSD analyses showed that the orientation of the c-axis of the BCT lattice of Sn grains played a major role regarding the evolution of the microstructure during electromigration stress. When the c-axis is parallel to the direction of current flow, the Cu and Ni can diffuse from the substrate at the cathode and form IMC at the interface or near the anode.

(5) When the c-axis is transverse to the direction of the current flow, the small atomic radius alloying elements cannot diffuse easily though the solder matrix, and IMC does not grow. However, it was seen that it can greatly hinder the reliability of the solder by depleting the Cu at the anode, and due to the lack of supply of new Cu atoms and slow Sn self-difussion, causes nucleation and propagation of voids.

(6) Zn does not play a significant role on controlling the evolution of the microstructure during high current density electromigration tests, which was observed when different Zn content solders using OSP and ENIG surface finishes had its microstructure evolution compared for similar grain orientations – favorable to Cu diffusion.

REFERENCES

[1] World Semiconductor Trade Statistics, **WSTS Semiconductor Market Forecast 2017**. Available at: <http://www.wsts.org/>. Accessed by 12/01/2017.

[2] TUMMALA, R., RYMASZEWSKI, E. J., KLOPFENSTEIN, Alan G. **Microelectronics packaging handbook: technology drivers.** Springer Science & Business Media, 2001.

[3] TUMMALA, R. **Packaging: past, present and future.** 6th International Conference on Electronic Packaging Technology, 2005. p. 3–7.

[4] TUMMALA, R. **Moore's Law meets its match.** IEEE Spectrum, 43(6), 2006. p. 44–49.

[5] BADER, B., RICHARDSON, C., TSURIYA, M. **Technology Roadmap overviews and future direction through technology gaps.** In: Electronics Packaging and iMAPS All Asia Conference (ICEP-IACC), 2015 International Conference on. IEEE, 2015. p. 219-224.

[6] ABTEW, M., & SELVADURAY, G. **Lead-free solders in microelectronics.** Materials Science and Engineering R: Reports, 27(5), 2000. p. 95–141.

[7] SEO, S.-K. **β-Sn Grain Orientations in Pb-free Solders and Their Effect on the Reliability of Solder Joints.** 2010. 155p. Doctor of Philosophy Thesis. Department of Materials Science and Engineering. Korean Advanced Institute of Science and Technology.

[8] PULLITZ, K. **Handbook of Lead-Free Solder Technology for Microelectronic Assemblies**, ed. K.J. Puttlitz and K.A. Stalter (New York: Marcel Dekker, Inc.) 2004. pp. 239–280.

[9] SZENDIUCH, I. **Roadmap of Lead-free Soldering.** IEEE International Symposium on Systems Engineering, 30th, 2007. p. 527–534.

[10] ZHANG, H., TOLBERT, L. M., OZPINECI, B. **Impact of SiC devices on hybrid electric and plug-in hybrid electric vehicles**. IEEE Transactions on Industry Applications, 47(2), 2011. pp. 912–921.

[11] WU, C. et al, **Microstructure and mechanical properties of new lead-free Sn-Cu-RE solder alloys.** Journal of Electronic Materials, 31(9), 2002. pp. 928–932.

[12] KOO, J. et al, **New Sn-0.7Cu-based solder alloys with minor alloying additions of Pd, Cr and Ca.** Journal of Alloys and Compounds, 608, 2014. pp. 126–132.

[13] CHO, M. G., KANG, S. K., LEE, H. M. **Undercooling and microhardness of Pb-free solders on various under bump metallurgies.** Journal of Materials Research, 23(04), 2008. pp. 1147–1154.

[14] JEE, Y. K., KO, Y. H., YU, J. **Effect of Zn on the intermetallics formation and reliability of Sn-3.5 Ag solder on a Cu pad.** Journal of materials research, v. 22, n. 07, 2007. pp. 1879-1887.

[15] YU, C. et al. **Suppression of Cu_3Sn and Kirkendall voids at Cu/Sn-3.5 Ag solder joints by adding a small amount of Ge.** Journal of Materials Science: Materials in Electronics, v. 23, n. 1, 2012. pp. 56-60.

[16] LU, M. et al, **Effect of Zn doping on SnAg solder microstructure and electromigration stability.** Journal of Applied Physics, 106(5), 2009.

[17] ARENAS, M., HE, M., ACOFF, V. **Effect of flux on the wetting characteristics of SnAg, Sn-Cu, SnAgBi, and SnAgCu lead-free solders on copper substrates.** Journal of Electronic Materials, 35(7), 2006. pp. 1530–1536.

[18] PRAKASH, K. H., & SRITHARAN, T. **Interface reaction between copper and molten tin-lead solders**. Acta Materialia, 49(13), 2001. pp. 2481–2489.

[19] FREAR, D. R., JANG, J. W., LIN, J. K., & ZHANG, C. **Pb-free solders for flip-chip interconnects.** Journal of Materials, 53(6), 2001. pp. 28–33.

[20] LIU, C. Y., & TU, K. N. **Morphogy of wetting reactions of SnPb alloys on Cu as a function of alloy composition**. Journal of Materials Research, 13, 1998. pp. 37–44.

[21] LEE, T. Y., CHOI, W. J., TU, K. N., JANG, J. W., KUO, S. M., LIN, J. K., KIVILAHTI, J. K. **Morphology, kinetics, and thermodynamics of solid-state aging of eutectic SnPb and Pb-free solders (Sn–3.5Ag, Sn–3.8Ag–0.7Cu and Sn–0.7Cu) on Cu.** Journal of Materials Research, v. 17, n. 2, p. 291-301, 2002.

[22] SUNWOO, A. J., MORRIS, J. W., & LUCEY, G. K. **The growth of Cu-Sn intermetallics at a pretinned copper-solder interface.** Metallurgical Transactions A, 23(4), 1992. pp. 1323–1332.

[23] CHOU, C. Y., CHEN, S. W. **Phase equilibria of the Sn-Zn-Cu ternary system.** Acta Materialia, 54(9), 2006. pp. 2393–2400.

[24] YANG, S. C., & KAO, C. R. **Role of minor Zn addition in the interfacial reaction between lead-free solders and Cu.** Proceedings of Technical Papers - 2007 International Microsystems, Packaging, Assembly and Circuits Technology Conference, IMPACT, 250, 2007. pp. 102–105.

[25] WANG, H., WANG, F., GAO, F., MA, X., & QIAN, Y**. Reactive wetting of Sn0.7Cu-xZn lead-free solders on Cu substrate.** Journal of Alloys and Compounds, 433(1-2), 2007. pp. 302–305.

[26] KUMAR, Girish; PRABHU, K. Narayan. **Review of non-reactive and reactive wetting of liquids on surfaces**. Advances in colloid and interface science, v. 133, n. 2, p. 61-89, 2007.

[27] KOTADIA, H. R., MOKHTARI, O., CLODE, M. P., GREEN, M. A., & MANNAN, S. H. **Intermetallic compound growth suppression at high temperature in SAC solders with Zn addition on Cu and Ni-P substrates.** Journal of Alloys and Compounds, 511(1), 2012. pp. 176–188.

[28] CHO, M. G., KANG, S. K., SHIH, D. Y., & LEE, H. M. **Effects of minor additions of Zn on interfacial reactions of Sn-Ag-Cu and Sn-Cu solders with various Cu substrates during thermal aging**. Journal of Electronic Materials, 36(11), 2007. 1501–1509.

[29] DENG, X., PIOTROWSKI, G., WILLIAMS, J. J., & CHAWLA, N. **Influence of initial morphology and thickness of Cu_6Sn_5 and Cu_3Sn intermetallics on growth and evolution during thermal aging of Sn-Ag solder/Cu joints.** Journal of Electronic Materials, 32(12), 2003. pp.1403–1413.

[30] MU, D. K., MCDONALD, S. D., READ, J., HUANG, H., & NOGITA, K. **Critical properties of Cu_6Sn_5 in electronic devices: Recent progress and a review.** Current Opinion in Solid State and Materials Science, 20(2), 2016. pp. 55–76.

[31] SHANG, P. J., LIU, Z. Q., PANG, X. Y., LI, D. X., & SHANG, J. K. **Growth mechanisms of Cu_3Sn on polycrystalline and single crystalline Cu substrates.** Acta Materialia, 57(16), 2009. pp. 4697–4706.

[32] MA, D., WANG, W. D., & LAHIRI, S. K. **Scallop formation and dissolution of Cu-Sn intermetallic compound during solder reflow**. Journal of Applied Physics, 91(5), 2002. pp. 3312–3317.

[33] LI, J. F., AGYAKWA, P. A., & JOHNSON, C. M. **Interfacial reaction in Cu/Sn/Cu system during the transient liquid phase soldering process.** Acta Materialia, 59(3), 2011. pp. 1198–1211.

[34] CHO, M. G., KIM, H. Y., SEO, S. K., & LEE, H. M. **Enhancement of heterogeneous nucleation of β-Sn phases in Sn-rich solders by adding minor alloying elements with hexagonal closed packed structures**. Applied Physics Letters, 95(2), 2009a. pp. 1–4.

[35] CHO, M. G., KANG, S. K., SEO, S. K., SHIH, D. Y., & LEE, H. M. **Interfacial reactions and microstructures of Sn-0.7Cu-xZn solders with Ni-P UBM during thermal aging**. Journal of Electronic Materials, 38(11), 2009b. pp. 2242–2250.

[36] LU, M., SHIH, D. Y., LAURO, P., KANG, S., GOLDSMITH, C., & SEO, S. K. **The effects of Ag, Cu compositions and Zn doping on the electromigration performance of pb-free solders.** Proceedings - Electronic Components and Technology Conference, 1, 2009. pp. 922–929.

[37] KHOSLA, A., & HUNTINGTON, H. B. **Electromigration in tin single crystals**. Journal of Physics and Chemistry of Solids, 36(5), 1975. pp. 395–399.

[38] JUNG, Y. **Effects of electromigration on the Kirkendall void and intermetallic compounds growths in lead-free solder joints.** 2014. 104p. Doctor of Philosophy Thesis. Department of Materials Science and Engineering. Korean Advanced Institute of Science and Technology.

[39] GAN, H., TU, K. N. **Polarity effect of electromigration on kinetics of intermetallic compound formation in Pb-free solder V-groove samples**. Journal of Applied Physics, 97(6), 2005.

[40] CONRAD, H. **Effects of electric current on solid state phase transformations in metals.** Materials Science and Engineering: A, 287(2), 2000. pp. 227–237.

[41] CHEN, C., TONG, H. M., & TU, K. N. **Electromigration and Thermomigration in Pb-Free Flip-Chip Solder Joints**. Annual Review of Materials Research, 40(1), 2010. pp. 531–555.

[42] CHEN, L. D., HUANG, M. L., & ZHOU, S. M. **Effect of electromigration on intermetallic compound formation in line-type Cu/Sn/Cu interconnect**. Journal of Alloys and Compounds, 504(2), 2010. pp. 535–541.

[43] TU, K. N. **Recent advances on electromigration in very-large-scale-integration of interconnects.** Journal of Applied Physics, 94(9), 2003. pp. 5451–5473.

[44] ZHANG, X. F., GUO, J. D., & SHANG, J. K. **Reverse polarity effect from effective charge disparity during electromigration in eutectic Sn–Zn solder interconnect.** Journal of Materials Research, 23(12), 2008. pp. 3370–3378.

[45] LIU, H. Y., ZHU, Q. S., WANG, Z. G., GUO, J. D., & SHANG, J. K. **Effects of Zn addition on electromigration behavior of Sn-1Ag-0.5Cu solder interconnect**. Journal of Materials Science: Materials in Electronics, 24(1), 2013. pp. 211–216.

[46] YEH, E. C. C., CHOI, W. J., TU, K. N., ELENIUS, P., & BALKAN, H. **Current-crowding-induced electromigration failure in flip chip solder joints**. Applied Physics Letters, 80(4), 2002. pp. 580–582.

[47] LIU, P., WANG, S., LI, D., LI, Y., & CHEN, X.-Q. **Fast and Huge Anisotropic Diffusion of Cu (Ag) and Its Resistance on the Sn Self-diffusivity in Solid β–Sn**. Journal of Materials Science & Technology, 32(2), 2016. pp. 121–128.

[48] KIM, J. M., JEONG, M. H., YOO, S., & PARK, Y. B. **Effects of surface finishes and current stressing on interfacial reaction characteristics of Sn-3.0Ag-0.5Cu solder bumps.** Journal of Electronic Materials, 41(4), 2013. pp. 791–799.

[49] MEI, Z. et al. **Brittle interfacial fracture of PBGA packages soldered on electroless nickel/immersion gold.** In: Electronic Components & Technology Conference, 1998. 48th IEEE. IEEE, 1998. pp. 952-961.

[50] YOON, J. W.; JUNG, S. B. **Interfacial reactions between Sn–0.4 Cu solder and Cu substrate with or without ENIG plating layer during reflow reaction.** Journal of alloys and compounds, v. 396, n. 1, p. 122-127, 2005.

[51] YOON, J. W.; KIM, S. W.; JUNG, S. B. **IMC morphology, interfacial reaction and joint reliability of Pb-free Sn–Ag–Cu solder on electrolytic Ni BGA substrate.** Journal of Alloys and Compounds, v. 392, n. 1, p. 247-252, 2005.

[52] CHOI, W. K.; LEE, H. M. **Prediction of primary intermetallic compound formation during interfacial reaction between Sn-based solder and Ni substrate.** Scripta Materialia, v. 46, n. 11, p. 777-781, 2002.

[53] LIU, Y. et al. **Fracture reliability concern of (Au, Ni) Sn 4 phase in 3D integrated circuit microbumps using Ni/Au surface finishing.** Scripta Materialia, v. 119, p. 9-12, 2016.

[54] SEO, S. K. et al. **Minor alloying effects of Ni or Zn on microstructure and microhardness of Pb-free solders.** In: Electronic Components and Technology Conference (ECTC), 2011 IEEE 61st. IEEE, 2011. p. 84-89.

[55] FÜRTAUER, S. et al. **The Cu–Sn phase diagram, Part I: new experimental results.** Intermetallics, v. 34, p. 142-147, 2013.

[56] VENTURA, T. et al. **Effects of solidification kinetics on microstructure formation in binary Sn–Cu solder alloys**. Acta Materialia, v. 59, n. 4, p. 1651-1658, 2011.

[57] LEHMAN, L. P. et al. **Cyclic twin nucleation in tin-based solder alloys**. Acta Materialia, v. 58, n. 10, p. 3546-3556, 2010.

[58] BIELER, T. R. et al. **Influence of Sn grain size and orientation on the thermomechanical response and reliability of Pb-free solder joints**. IEEE Transactions on Components and Packaging Technologies, v. 31, n. 2, p. 370-381, 2008.

[59] ARFAEI, B.; BENEDICT, M.; COTTS, E. J. **Nucleation rates of Sn in undercooled Sn-Ag-Cu flip-chip solder joints**. Journal of Applied Physics, v. 114, n. 17, p. 173506, 2013.

[60] PARKS, G. et al. **The nucleation of Sn in undercooled melts: the effect of metal impuritie**s. JOM, v. 66, n. 11, p. 2311-2319, 2014.

[61] ARFAEI, B.; KIM, N.; COTTS, E. J. **Dependence of Sn grain morphology of Sn-Ag-Cu solder on solidification temperature**. Journal of electronic materials, v. 41, n. 2, p. 362-374, 2012.

[62] TU, K. N.; GUSAK, A. M.; LI, M**. Physics and materials challenges for lead-free solders**. Journal of applied Physics, v. 93, n. 3, p. 1335-1353, 2003.

[63] SEO, S. K. et al. **The crystal orientation of β-Sn grains in Sn-Ag and Sn-Cu solders affected by their interfacial reactions with Cu and Ni (P) under bump metallurgy**. Journal of Electronic Materials, v. 38, n. 12, p. 2461-2469, 2009.

[64] KIM, Y. I.; YOON, J. H.; JUNG, S. B. **Effects of Pd layer thickness on mechanical properties and microstructures of Sn-3.0 Ag-0.5 Cu solder joints.** International Journal of Materials and Structural Integrity 12, v. 8, n. 1-3, p. 76-87, 2014.

[65] KANG, S. K. et al. **Ag3Sn plate formation in the solidification of near-ternary eutectic Sn-Ag-Cu.** Jom, v. 55, n. 6, p. 61-65, 2003.

[66] KOTADIA, H. R. et al. **Electronics Assembly and High Temperature Reliability Using Sn-3.8 Ag-0.7 Cu Solder Paste With Zn Additives.** IEEE Transactions on Components, Packaging and Manufacturing Technology, v. 3, n. 10, p. 1786-1793, 2013.

[67] ALAM, M. O. et al. **High electric current density-induced interfacial reactions in micro ball grid array (µBGA) solder joints.** Acta Materialia, v. 54, n. 3, p. 613-621, 2006.

[68] LU, M. et al. **Effect of Joule heating on electromigration reliability of Pb-free interconnect**. In: Electronic Components and Technology Conference (ECTC), 2012 IEEE 62nd. IEEE, 2012. p. 590-596.

[69] YOON, J. W.; LEE, C. B.; JUNG, S. B. **Growth of an intermetallic compound layer with Sn-3.5 Ag-5Bi on Cu and Ni-P/Cu during aging treatment.** Journal of electronic materials, v. 32, n. 11, p. 1195-1202, 2003.

[70] HUNTINGTON, H. B.; GRONE, A. R. **Current-induced marker motion in gold wires**. Journal of Physics and Chemistry of Solids, v. 20, n. 1-2, p. 76-87, 1961.

[71] SEO, S. K. et al. **The evolution of microstructure and microhardness of Sn–Ag and Sn–Cu solders during high temperature aging**. Microelectronics Reliability, v. 49, n. 3, p. 288-295, 2009.

[72] FU, N. et al. **Visualization of Microstructural Evolution in Lead Free Solders during Isothermal Aging Using Time-Lapse Imagery.** In: Electronic Components and Technology Conference (ECTC), 2017 IEEE 67th. IEEE, 2017. p. 429-440.